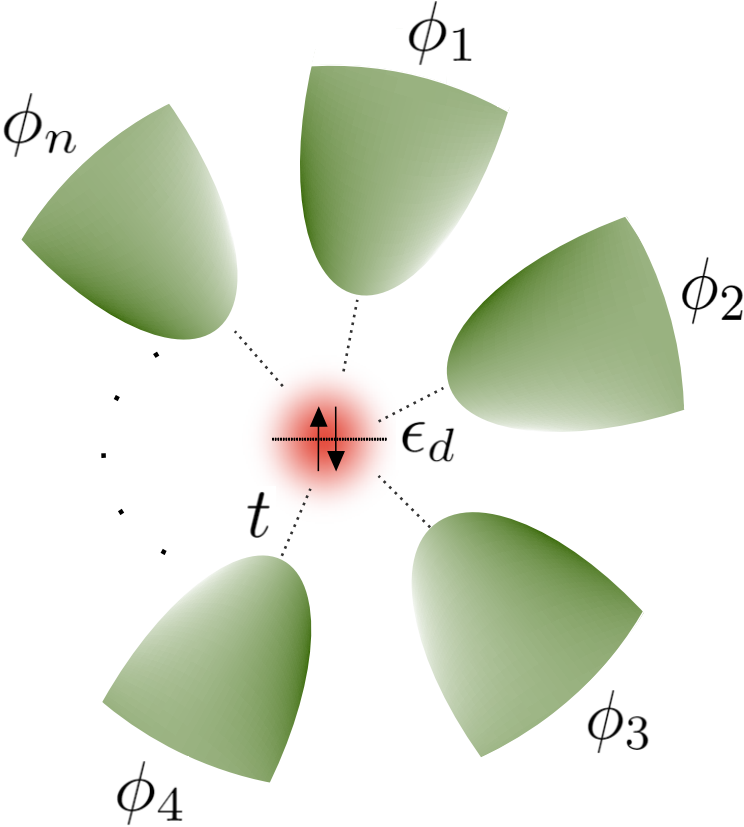# Master Thesis: Properties of Multiterminal Josephson Junctions

by Elvira C. Jarmbæk Jacobsen

Master student in Quantum Physics at the Niels Bohr Institute, University of Copenhagen

Supervised by Karsten Flensberg and Max Geier

April 14, 2023

Abstract

The coupling of additional superconductors to the successful Josephson junction has been studied for decades. However, the experimental manifestation of the multiterminal Josephson effect was not accomplished before a few years ago. This motivates the theoretical studies of this thesis, which focuses on using a model describing the multiterminal Josephson junction by n equal superconductors coupled through a non-interacting single energy level of a quantum dot to cover a wide selection of properties. Based on this, we review and reproduce results of a range of previously found theoretical and experimental studies, both serving as a validation of the model and a springboard for adding new details. The major topic concerns the conductance properties of a current-biased three-terminal Josephson junction. The impact of the Q factor is emphasised and it is shown how the regime of bias currents only slightly exceeding the critical current contour complicates the system dynamics, expressed through the behaviour of the multiplet resonances and the branches of reduced differential resistance. We study the deformation of the critical current contour in the presence of a magnetic field and find agreement with experimental results. Using a sinusoidal time-dependent magnetic field, half-integer Shapiro steps are demonstrated. In addition, we propose a design for a protected superconducting qubit involving a three-terminal Josephson junction and suggest an accompanying gate method.

Contents

1 Introduction

In the early 20th century, alongside the development of two of the cornerstones of modern physics, namely the General Theory of Relativity and Quantum Theory, superconductivity was observed for the very first time. The groundbreaking discovery was made in a laboratory in Leiden in 1911 by H. Kamerlingh Onnes, showing that some metals have a critical temperature T_c on the order of 1 K, at which the electrical resistance vanishes abruptly, such that current, a *supercurrent*, can flow with no dissipation [1]. This discovery of an exotic phase of matter was the beginning of an era in condensed matter physics. Despite huge efforts, many years went by before a satisfying microscopic theory of superconductivity, the BCS theory by Bardeen, Cooper and Schrieffer, was published in 1957 [2]. Only five years after, in 1962, it was predicted by B. D. Josephson that a supercurrent can flow across a weak link between two superconductors; a prediction which was accompanied by the associated current and voltage relations [3].

Today, a Josephson junction is an appreciated and widely used device. It is used in a range of devices, including the SQUID, which is an ultrasensitive magnetometer that converts flux to voltage using the Josephson effect [1]. Josephson junctions play a significant role in the context of quantum computing, where solid state physics offers some of the leading platforms for implementation. One of the most famous and prevalently used superconducting qubits, the transmon, was included in the Google 2019 quantum processor [4] and other realizations of quantum computer technologies. The Josephson junction is an invaluable element in the transmon and many other superconducting qubits [5].

One of the main obstacles for the development of quantum computers across all fields is the tradeoff between isolation and control. The qubits need to be completely isolated from the environment to preserve their quantum states, where on the other hand measurements are obviously a necessary part of quantum computation. The compromise means preserving the quantum state for a coherence time just sufficient to perform the computations and the measurements with sufficiently few errors, depending on the error correction schemes available. Keeping the coherence time up and the error rate down is crucial, and it is therefore necessary to invest a huge amount of effort to limit the noise. There has already been many proposals for more complex qubits which have exceeded the coherence times of the transmon [6], but quantum computation remains in its early stage and a wide range of possibilities are still tried out [7].

Considering the success of Josephson junctions, the generalization to n terminals seems like a natural field of investigation. The additional degrees of freedom would be expected to bring along new phenomena worth exploring. Indeed, theoretical studies of multiterminal Josephson junctions go at least three decades back [8].

The conductance properties of multiterminal Josephson junctions have been investigated by current biasing the leads and using a generalized RCSJ model for the resistance built in at finite voltages, constituting a semiclassical description (see eg. [9], [10], [11]). These studies showed

a coexistence of supercurrent and dissipative currents up to high bias currents. Other central findings include the generalization of MAR involving multiple leads [9], multiplet resonances [10], where perfect conductance arises at finite voltages and fractional Shapiro steps [11]; plateaus in the $I - V$ curves when the currents are alternating.

One of the findings about multiterminal Josephson junctions that has caused the greatest amount of scientific excitement concerns their topological properties. Despite that they are typically constructed by topologically trivial materials only, the Andreev bound states (ABS) formed in the normal region of the junction have been predicted to host topological phases and accommodate Weyl singularities for $n \geq 4$, realizing topology in $n - 1$ dimensions in the space of the $n - 1$ independent phase differences across the junction (see eg. [12], [13], [14]). The energy spectrum of multiterminal Josephson junctions can accordingly be used to emulate the band structure of topologically nontrivial materials. This is a huge topic in itself and will not be covered further in this work. Other ideas for potential applications include circuit elements for new types of qubits [15] or for coupling multiple qubits [16], formation of an Andreev interferometer, which have been shown to possess advantages of the SQUID [17] and realizing a flux-controlled Josephson diode effect [18].

The first experiments involving three terminals have been conducted within the last decade. However, the experimental precision necessary has not been within reach until a few years ago. Multiterminal supercurrents were reported in 2019 [19], but the first convincing experimental manifestation of the Josephson effect in three- and four-terminal Josephson junctions to our knowledge was published in 2020 [20]. Here, the critical current contour (CCC), which is the generalization of the critical current scalar I_c of standard junctions, that had been overlooked so far, was studied in detail. It was found how it responded to magnetic fields, and the results were compared to the CCC's produced by the scattering matrix approach applied to multiterminal ABS. Additional assumptions about the symmetry properties were made, but there was a good agreement between theory and experiment even with no assumptions about the microscopic details of the junction. Hence, the results were deemed probable as a manifestation of the multiterminal Josephson effect.

The relationship between theory and technology is a dynamical interplay, and now that the technology for performing experiments with multiterminal Josephson junctions is a reality, the research in this area has gained additional momentum. With this project, we aim to use the newly gained experimental evidence for the properties of multiterminal Josephson junctions to take a step back and test how well a model of a junction consisting of a single, non-interacting level between the superconducting leads, can capture the observed phenomena. We use this relatively simple model to describe a broad range of properties of multiterminal Josephson junctions. We both reproduce results of other publications, which serves as a compact review and a validity test of the model, and we contribute with additional details, perspectives and ideas. Finally, we propose a starting point for a protected superconducting qubit including a multiterminal

Josephson junction which is placed in extension of modern qubit proposals.

1.1 Outline

The thesis is organized as follows:

In Chapter 2 the relevant background physics is introduced, aimed to equip the reader, assumed to be a physics student at the master level or equivalent, with knowledge sufficient to understand the main parts of the thesis. The chapter introduces the reader to Josephson junctions and the dynamics of the RCSJ model for dissipation. It also introduces Andreev reflections, the SQUID and important recent findings about multiterminal Josephson junctions. Finally, the huge topic of superconducting qubits is also introduced, with a focus of qubits protected from decoherence.

Chapter 3 is where the main analytical work is done. It is shown how one can, with the proper simplifications, derive an effective Hamiltonian for the model consisting of a quantum dot of a single energy level coupled to n superconducting leads. From this Hamiltonian, the ground state energy and the form of the Josephson currents is given, focusing on three-terminal Josephson junctions, which are quantities used extensively in the following chapters.

Chapter 4 paves the way for making a protected superconducting qubit with one two- and one three-terminal Josephson junction, finding desirable and realistic parameter settings, showing the energy dispersion as a function of bias parameters and finding the form of the qubit states. Finally, a method for implementation of gates is proposed.

Chapter 5 extends the RCSJ model to the three-terminal Josephson junction, and the differential resistance as a function of bias currents is studied extensively, both in absence and presence of a magnetic field. The results are compared to recent similar experimental results. Finally, a first step is taken to study the manifestation of fractional Shapiro steps in the system.

1.2 Acronyms

ABS	Andreev Bound State
CCC	Critical Current Contour
DSFQ	Double Shunted Flux Qubit
MAR	Multiple Andreev Reflection
NS	Normal-Superconducting
RCSJ	Resistively and Capacitively Shunted
SQUID	Superconducting Quantum Interference Device
Q	Quality factor proportional to $R\sqrt{C}$
QD	Quantum Dot

2 Background

This chapter starts out with a very short introduction to the main aspects of superconductivity relevant for the following work, after which four subsections follow, introducing in more detail the relevant background physics.

One of the fundamental building blocks of superconductivity is the formation of bound states between two electrons of opposite momentum and spin, *Cooper pairs*, an idea presented by L. N. Cooper. A supercurrent, i.e. a current flowing with no dissipation, is carried by Cooper pairs. Hence, the discovery of the Josephson effect brought along the more general result that not only single electrons, but in this case also paired electrons, are able to tunnel over a barrier.

At $T = 0$ in the normal state, all momentum states are filled up to the Fermi level. Transitioning to the superconducting state involves Cooper pairing of electrons with binding energy 2Δ, which induces a gap in the density of states between $-\Delta$ and Δ around the Fermi level at zero energy.

In contrast to a normal metal, where the wavefunctions describing each of the electrons are unrelated, the entire ensemble of Cooper pairs is described by a single many-body wavefunction with a fixed phase relation. The quantum coherence of the superconducting wavefunction can explain the properties of superconductors, including vanishing resistance, the Meissner effect, flux quantization and the Josephson effect, of which the two latter will be introduced in this chapter.

A superconductor is hence described by a macroscopic quantum state where the seemingly intangible concept of the phase of a quantum wavefunction can account for macroscopic phenomena like observable currents. This is one of the main reasons why superconductivity is a subject getting huge attention.

2.1 Two-terminal Josephson Junctions and the RCSJ Model

A Josephson junction is formed by separating two superconducting electrodes by a thin, non-superconducting layer. The link must be thin enough for the wavefunctions of each electrode to overlap, which allows tunneling of Cooper pairs across the link, driven by the phase difference ϕ between the superconductors' wavefunctions at the boundaries. This establishes a supercurrent I_s across the link, which can flow at zero voltage. If there is a voltage over the Josephson junction, the supercurrent oscillates, and consequently this phenomenon is called the DC or AC Josephson effect in the case of a zero and finite voltage over the junction, respectively.

The property that Cooper pairs leak into the normal metal at an interface between normal and superconducting layers (NS-interface) is known as the proximity effect [21]. This results in the formation of a gap in the density of states and Andreev bound states (ABS) in the normal layer. ABS are discrete pairs of states emerging inside the energy gap, and they typically carry most of the supercurrent across a Josephson junction [22].

The Josephson relations predicted by B. D. Josephson for a two-terminal Josephson junction with superconducting phase difference ϕ and voltage V are

$$I_J = I_c \sin(\phi) \qquad V = \frac{\hbar}{2e} \frac{d\phi}{dt}. \tag{2.1}$$

A Josephson junction has the associated Josephson current $I_J = I_c \sin(\phi)$, whose amplitude is the critical current I_c, the maximal supercurrent that the junction can support, which is generally much lower than the critical current of the superconducting leads.

The relation for voltage can be understood in both directions; a finite voltage can either be applied or appear when a current $I > I_c$ is forced through the junction, which results in dissipation and a nonzero $\langle \dot{\phi} \rangle$. One can include the finite resistance regime in the model semiclassically by shunting the Josephson junction, i.e. connecting it in parallel in an electical circuit, by a resistor and capacitor known as the Resistively and Capacitively Shunted Josephson Junction (RCSJ) model [1].
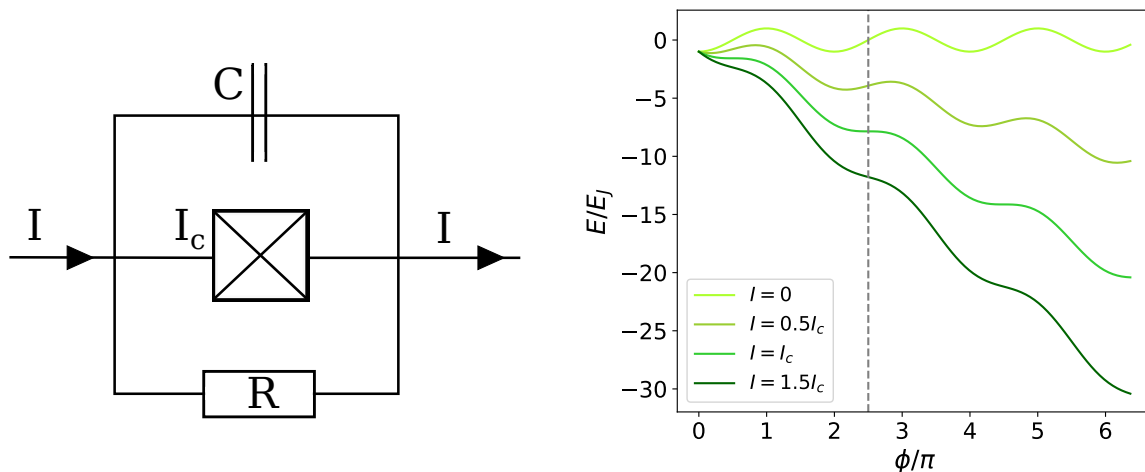

Figure 2.1: Left: The RCSJ model. A two-terminal Josephson junction, biased by current I, is shunted by a resistor and a capacitor. Right: 1D tilted washboard potential $U(\phi)$ for four different values of I. The vertical line $\phi = \pi/2$ is added to show how the minima are shifted from $\phi = 0$ to $\phi = \pi/2$. Energies are measured in units of the Josephson energy $E_J = \hbar I_c/2e$.

The RCSJ model is shown in Figure 2.1 (left), where the circuit elements are connected in parallel and the currents through each part of the circuit are related through Kirchoff's First Law

$$I = I_c \sin(\phi) + \frac{V}{R} + C\dot{V}.$$

The voltage V is replaced by the Josephson relation $V = \hbar\dot{\phi}/2e$, such that we get the second order differential equation for the phase difference over the junction ϕ

$$I = I_c \sin(\phi) + \frac{\hbar}{2eR}\dot{\phi} + \frac{\hbar C}{2e}\ddot{\phi}$$

After introducing the dimensionless time variable $\tilde{t} = Qt/RC$, where $Q = R\sqrt{2eI_cC/\hbar}$ the equation of motion for the phase can be written in dimensionless form, where we can see that the dynamics are determined solely by the Q factor and the ratio of the bias- to critical current.

5

$$\frac{I}{I_c} = \ddot{\phi} + Q^{-1}\dot{\phi} + \sin(\phi) \tag{2.2}$$

This classical model of the finite voltage regime of the junction gives a good intuition about the physics of the system, since there exists mechanical analogs. Here, we will lean on the tilted washboard model, which is characterized by the potential

$$U(\phi) = -\frac{\hbar I_c}{2e}\Big(\cos(\phi) - \frac{I}{I_c}\phi\Big).$$

The washboard refers to the sinusoidal curve which tilts when a bias current I is applied, as shown in Figure 2.1 (right). Considering a fictitious particle of mass $(\frac{\hbar}{2e})^2 C$ moving in this potential while subjected to a viscous drag force $-\frac{1}{R}(\frac{\hbar}{2e})^2\dot{\phi}$, it has the equation of motion

$$\Big(\frac{\hbar}{2e}\Big)^2 C\ddot{\phi} = -\frac{dU(\phi)}{d\phi} - \frac{1}{R}\Big(\frac{\hbar}{2e}\Big)^2\dot{\phi}.$$

By rewriting in terms of the dimensionless time variable $\tilde{t}$ and Q, this is seen to be the same equation of motion as in (2.2), which legitimizes the analogy.

When $I < I_c$, there exists stationary solutions to the equation of motion. Starting from an arbitrary ϕ, the particle rolls down the incline due to the influence from the potential $-\partial U/\partial\phi = \frac{\hbar I_c}{2e}\big(\frac{I}{I_c} - \sin(\phi)\big)$ until it rests in a minimum. Hence, when a small bias current enters the circuit, the phase of the Josephson junction adjusts such that all the bias current is guided through the junction which remains at $V = 0$. The minima sit in $\phi = 0$ for $I = 0$ and are shifted to lie at increasing ϕ-values until at $I = I_c$, where the minima become inflection points at $\phi = \pi/2 + 2\pi n$ as seen in Figure 2.1. This is the critical point above which the only solution for the particle under any conditions is to run down the tilted washboard which means the phase starts winding, resulting in a finite voltage and an AC current over the junction, according to (2.1). The current now has a DC component that runs through the resistor.

As mentioned, the effect of the capacitance C and resistance R on the dynamics can be collected in the Q factor. Staying in the washboard analogy, R is inversely proportional to the friction while C is proportional to the mass of the particle. Note the fact that increasing R means decreasing the drag of the particle on the washboard, which might lead to confusion. In the limit where $Q \ll 1$, drag dominates inertia, while in the opposite case $Q \gg 1$, the drag is negligible. For low Q, the velocity of the particle is approximately proportional to the slope of the washboard, such that when the bias current slightly exceeds I_c, making the slope alternatingly steep and almost flat, the particle spends almost all of the time on the flat sections. This is reflected in the voltage profile as a series of pulses, as seen in Figure 2.2. The $I - V$ relation in this regime is not Ohmic, but rather $V = R\sqrt{I^2 - I_c^2}$, however approaching $V = RI$ for $I \gg I_c$ [1].

If Q is sufficiently large as in Figure 2.3, the particle is able to start running down the washboard even though $I < I_c$, given that it starts at a higher potential than that of the next local maximum. This is not the case in the figure, but instead the long convergence time is demonstrated. Because
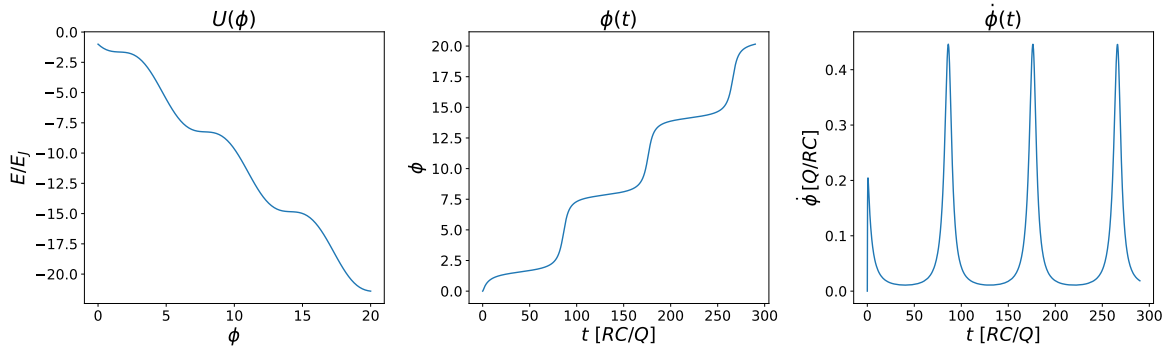
Figure 2.2: Position $\phi(t)$ and velocity $\dot{\phi}(t)$ as a function of time of a particle rolling down the incline $U(\phi)$. The bias current is slightly exceeding the critical current $(I = 1.05I_c)$ and $Q = 0.22$.
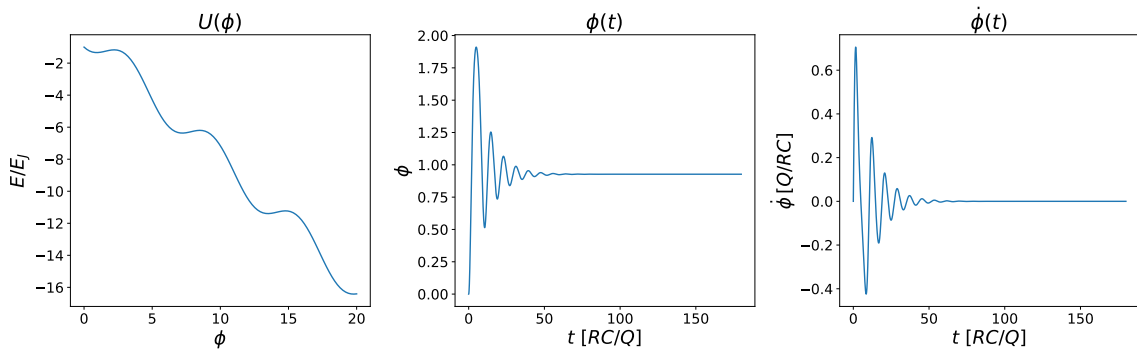

Figure 2.3: Position $\phi(t)$ and velocity $\dot{\phi}(t)$ as a function of time of a particle rolling down the incline $U(\phi)$. The bias current is slightly below the critical current $(I = 0.8I_c)$ and $Q = 5.14$.

of its large inertia, it might require $I \to 0$ to stop the motion of a particle rolling down the washboard at high Q, and the $I - V$ relation becomes hysteretic.

2.1.1 Andreev Reflections

Consider an interface between normal metal (N) and superconductor (S). If an electron in the normal metal of energy less than the superconducting gap Δ travels toward the NS-interface, transmission is not possible since there are no available single-electron states at that energy. Instead, it will be reflected. This can be either a normal reflection , where the electron simply reflects from the interface, or it can be Andreev reflected. The latter is unique to an interface with a superconductor. The electron is reflected as a hole with opposite spin while a Cooper pair travels into the superconductor, generating a supercurrent. This is the only way of transferring charge over an NS-interface at low bias voltages $eV < 2\Delta$. Hence the conductance in this regime is proportional to the probability of Andreev reflection [23].

Now consider the SNS-interface in Figure 2.4a, which we can see as a Josephson junction. An
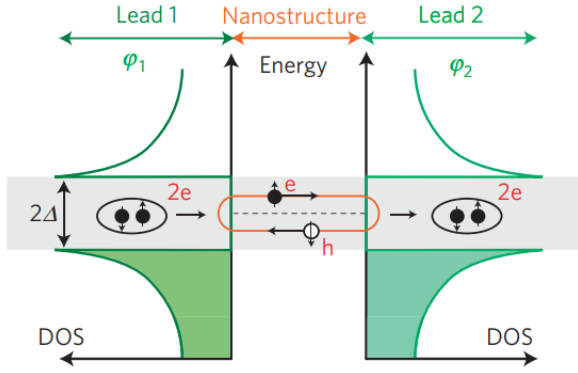
(a) Formation of Andreev Bound States (ABS) in a Josephson junction. The figure is from Ref. [24].
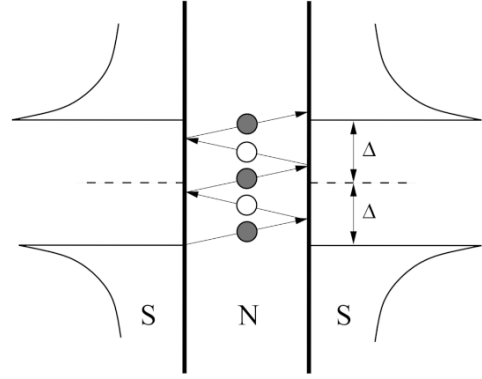
(b) Multiple Andreev Reflections (MAR) in a Josephson junction at a bias voltage between $eV \in]2\Delta/5; \Delta/2[$. The figure is from Ref. [25]

Figure 2.4: Figures showing (a) ABS at $V = 0$ and (b) MAR at $V < 2\Delta/e$ in a two-terminal junction.

electron in the normal metal is reflected at Lead 2, where it picks up the phase ϕ_2 of the superconductor and is reflected as a hole, which is again reflected at Lead 1 as the time-reversed counterpart of Andreev reflection, picking up the phase ϕ_1. The electron and hole make up an entangled pair and forms a coherent standing wave across the normal layer, an ABS [24]. The set of electron-hole pairs form a set of discrete energy levels inside the gap, symmetrically distributed around the Fermi energy. Recall that the Andreev reflection is also associated with a Cooper pair propagating in the superconducting part of the interface, as seen in Figure 2.4a. Because of the phase coherence, the ABS can carry a supercurrent from one superconductor to the other. In a Josephson junction the ABS play a big role, since they typically carry most of the Josephson current [22].

Now we consider the case where a bias voltage is applied. When the electron is Andreev reflected at a low voltage $eV < 2\Delta$, the retroreflected hole gains energy eV. After n Andreev reflections, the particle has gained energy neV and whenever the electron has gained at least the energy 2Δ, it can escape into the superconductor. Hence, at $eV = \Delta$ it requires one Andreev reflection for charge to propagate, for $eV = 2\Delta/3$ it requires two, etc. This describes the concept of multiple Andreev reflections (MAR), as illustrated in Figure 2.4b. It results in peaks in the conductance every time a new possibility of charge transport opens up at $eV = 2\Delta/n, n \in \mathbb{Z}$ [26]. Because the voltage is a fraction of $2\Delta/e$, the structure of the conductance as a function of voltage in this regime is known as subharmonic gap structure (SGS). MAR being responsible for the SGS in superconducting weak links has been known for 40 years [27].

2.2 Effect of Flux through a Superconducting Loop

A superconductor is characterized by a collective wavefunction for all electrons in the sample, only varying by its phase. Now we consider the case of a closed loop of superconducting material. First of all, the wavefunction must be single-valued such that $\Psi(\phi = 0) = \Psi(\phi = 2\pi)$. Now this loop is placed in a magnetic field, which results in the flux Φ through the loop

$$\Phi = \int \mathbf{B} \cdot d\mathbf{a} = \int \nabla \times \mathbf{A} \cdot d\mathbf{a} = \oint \mathbf{A} \cdot d\mathbf{s}.$$

The flux is related to the phase difference over a Josephson junction through the vector potential $\gamma = \phi - (2\pi/\Phi_0) \int \mathbf{A} \cdot d\mathbf{s}$ where γ is the gauge-invariant phase difference[1] and $\Phi_0 = h/2e$ is the magnetic flux quantum, so in this case the line integral of $\mathbf{A}$ around the loop must be a multiple of Φ_0. The vector potential can be shown to be $\mathbf{A} = (\Phi_0/2\pi)\nabla\phi$ inside the superconductor as long as the distance from the central interior of the superconductors to the edge is sufficiently large for all surrounding fields to decay [1].

The flux through the loop Φ produces screening currents in the superconducting loop that tend to cancel the flux. If we instead imagined that this closed loop was placed in a magnetic field resulting in a flux $\Phi = \Phi_0$ before cooling it down to its superconducting state, after which the magnetic field was turned off, the induced screening currents would persist since the usual decay in the case of a normal metal would break the single-valuedness of the wavefunction. This explains why superconducting rings are locked in a magnetic field and why practically eternal currents can flow.

If we now picture the loop interrupted by two Josephson junctions as seen in Figure 2.5a, this is known as a SQUID (Superconducting QUantum Interference Device). In this case, the change in phase along the superconducting part of the loop must be equal and opposite to the sum of the phase differences across the two junctions, i.e. $\int_{\text{superconductor}} \nabla\phi \cdot d\mathbf{s} = -(\phi_1 + \phi_2)$ such that

$$\Phi = \oint \mathbf{A} \cdot d\mathbf{s} = -\frac{\Phi_0}{2\pi}(\phi_1 - \phi_2) + \int_{\text{Junction 1}} \mathbf{A} \cdot d\mathbf{s} + \int_{\text{Junction 2}} \mathbf{A} \cdot d\mathbf{s}$$

with both phase differences ϕ_1 and ϕ_2 taken in the "down" direction as shown in Figure 2.5a, while all line integrals are taken in clockwise direction around the loop. The single-valuedness of the wavefunction means that the phases of the Josephson junctions are interdependent. Using the relation for the Josephson junctions $\gamma = \phi - (2\pi/\Phi_0) \int \mathbf{A} \cdot d\mathbf{s}$, the ϕ_1 and ϕ_2 terms cancel, and the result is

$$\gamma_2 - \gamma_1 = 2\pi \frac{\Phi}{\Phi_0} \,(\text{mod}\, 2\pi). \tag{2.3}$$

Equivalently, the phases of the junctions are modified as $\gamma_1 \rightarrow \gamma_1 + 2\pi\Phi/\Phi_0$. In general, this phase shift can be applied to any current carrying circuit element.

---

[1]Throughout the thesis, the symbol ϕ, which is equivalent to γ in the case where any present magnetic fields can be neglected, will simply be used for phase difference, but it is necessary to make the distinction here in order to show the relation between phase and flux.
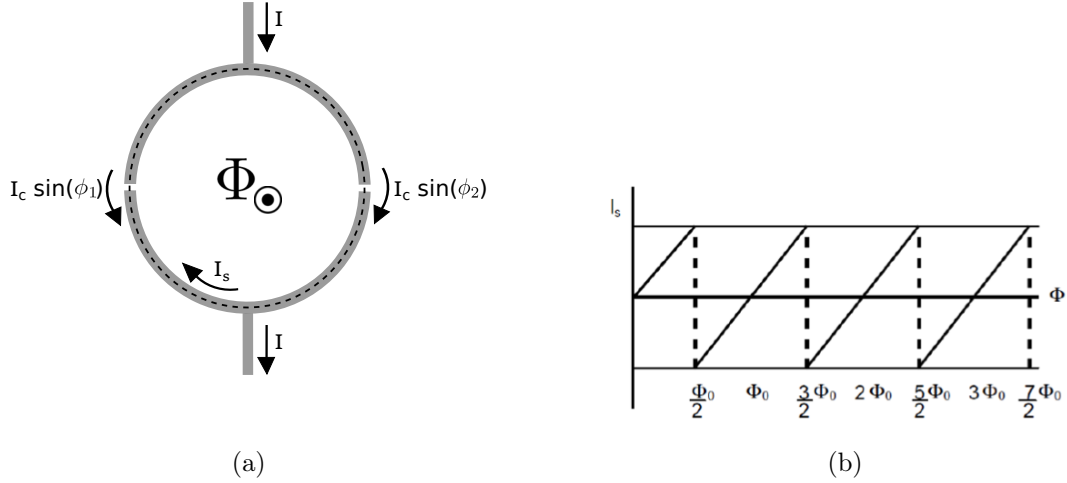
Figure 2.5: Left: A SQUID is a superconducting loop biased by a current I and interrupted by two Josephson junctions with critical currents I_c and phase differences ϕ_1 and ϕ_2, respectively. The dashed circle marks the area that defines the flux Φ, which induces a screening current I_s in the loop. Right: Variation of screening current generated by the flux. Picture from [a]

[a]Course notes for "SQUID Practicum" at TU Delft

We know that the individual junctions have the critical current I_c which is reached for a bias current $I = I_c$ where the minima become flat inflection points at $\gamma = \pi/2$. The bias current I is equally split between the two junctions. When $\Phi = n\Phi_0$, $\gamma_1 = \gamma_2$, so they evolve equally. There is no way to tell from observing one of the junctions, that the junction is part of a loop and not just a straight wire, since it reacts exactly the same way to the bias current and the phase starts winding at $I = I_c$. From (2.3) we see that if $\Phi \neq n\Phi_0$, the two junctions cannot reach this point at the same time, and thus the critical current of the SQUID is reduced by the presence of a magnetic field. The total current over the SQUID is

$$I = I_c\big(\sin(\gamma_1) + \sin(\gamma_2)\big) = 2I_c \sin\left(\frac{\gamma_2 + \gamma_1}{2}\right)\cos\left(\frac{\gamma_2 - \gamma_1}{2}\right) = 2I_c \cos(\pi\Phi/\Phi_0)\sin(\pi\Phi/\Phi_0 + \gamma_1).$$

From this we see that the maximal supercurrent over the SQUID is reduced as a function of Φ via the relation

$$I_{c,\mathrm{SQUID}} = 2I_c|\cos(\pi\Phi/\Phi_0)|. \tag{2.4}$$

Additionally, we know that the applied flux induces a screening current I_s in the loop. The total flux Φ is in fact the sum of the applied (external) flux and the screening flux; $\Phi = \Phi_{ext} + \Phi_s$. The screening current combines with the bias currents such that the currents over the junctions are $I/2 + I_s$ and $I/2 - I_s$ as seen in Figure 2.5a. Whenever the current over one of the junctions exceeds I_c, the SQUID also exceeds its critical current. The meaning of the critical current of the SQUID is the maximal bias current where the voltage can be zero over the SQUID. From this, together with (2.4) we can conclude that $I/2 + I_s = I_c$ when $\Phi = \Phi_0/2$.

As Φ is increased from zero to one flux quantum, I_s increases as it attempts to cancel the flux

until it reaches $I_s = I_c - I/2$ at the point where $\Phi/\Phi_0 = 1/2$. In exceeding this point it becomes more favorable to increase the net flux to Φ_0, hence I_s changes direction after this point as seen in Figure 2.5b. During the time it takes for I_s to change direction, the net flux increases from 0 to Φ_0.

Using the result from (2.3), we have the general relations for the currents [1]

$$I = I_c\Big(\sin(\gamma_1) + \sin(\gamma_2)\Big)$$
$$I_s = (I_c/2)\Big(\sin(\gamma_2) - \sin(\gamma_1)\Big).$$

Combining these equations for maximal current and eliminating γ_1 using (2.3), the result is that $I/2 + I_s = I_c$ or, by eliminating γ_2 instead, we get that $I/2 - I_s = I_c$ at the critical point, as expected.

In this section, we have discussed the symmetric SQUID where both Josephson junctions have equal critical currents and seen how the current over the SQUID relate to the flux. This device can be seen as a single Josephson junction with tunable energy. Using (2.4), the energy of the symmetric SQUID becomes $-2E_J|\cos(\pi/\Phi/\Phi_0)|\cos(\phi)$ equivalently to a single junction with a critical current reduced as a function of Φ. In case of an asymmetric SQUID with critical currents I_c and αI_c, the energy is instead $-(E_{J,1} + E_{J,2})\sqrt{\cos^2(\pi/\Phi/\Phi_0) + d^2\sin^2(\pi/\Phi/\Phi_0)}\cos(\phi)$ with $d = (\alpha - 1)/(\alpha + 1)$ [5]. In the limit of $E_{J,2} \gg E_{J,1}$ or equivalently $\alpha \gg 1$, we see that the SQUID's energy reduces to $-E_{J,2}\cos(\phi)$ which is that of one single junction with no effect from the flux. This type of tunability is often useful in the context of superconducting qubits, which is the topic of the following section.

2.3 Superconducting Qubits

2.3.1 Charge and Flux Qubits

A classical LC-circuit is described by the Hamiltonian $H = CV^2/2 + LI^2/2$. Rewriting in terms of magnetic flux,

$$H_{LC} = \frac{1}{2}C\Big(\frac{d\Phi}{dt}\Big)^2 + \frac{1}{2}\frac{\Phi^2}{L}$$

makes clear that this is the circuit harmonic oscillator. In terms of its mechanical analogy, $x \to \Phi$, $m \to C$ and $\omega \to 1/\sqrt{LC}$.

Just like with the quantization of the harmonic oscillator, the LC-circuit can then be quantized via canonical quantization. We introduce the canonically conjugate variables charge and flux

$$[\hat{\Phi}, \hat{Q}] = i\hbar$$

and state the quantum mechanical LC circuit

$$\hat{H} = \frac{\hat{Q}^2}{2C} + \frac{1}{2}\frac{\hat{\Phi}^2}{L}.$$

11

We can switch to the operator $\hat{n} = \hat{Q}/2e$ which counts the number of electron pairs and the reduced flux $\hat{\phi} = 2\pi\hat{\Phi}/\Phi_0$ counting the flux quanta through the loop, where $\Phi_0 = h/2e$ is the magnetic flux quantum. Note that the reduced variables are still a conjugate pair $[\hat{\phi}, \hat{n}] = i$. This gives the usual form for superconducting circuit Hamiltonians,

$$\hat{H} = 4E_C\hat{n}^2 + \frac{1}{2}E_L\hat{\phi}^2,$$

with charging energy $E_C = e^2/2C$ and inductive energy $E_L = (\Phi_0/2\pi)^2/L$ [5].

Now, what we have is a quantized LC-circuit, which has the spectrum of a quantum harmonic oscillator. When looking for a qubit platform, it is necessary to be able to isolate two states of the energy spectrum well enough to describe it as an effective two-level system. The harmonic oscillator has the well-known feature of equidistant energy levels, meaning that the transition energies between any two neighboring energy states are the same, which immediately disqualifies any pair of eigenstates of the circuit as a qubit candidate.

The needed ingredient is a nonlinear circuit element which can introduce *anharmonicity* in the potential, and this is a main reason why the Josephson junction acts as a circuit element in most superconducting qubit proposals, as it has a nonlinear inductance

$$L_J = V\left(\frac{dI}{dt}\right)^{-1} = \frac{\hbar}{2eI_c\cos(\phi)}.$$

Integrating the work per unit time done by a current source to change the phase, expressed through the Josephson relations, yields the energy stored in the junction at time t

$$E(t) = \int_{-\infty}^{t} dt' I(t')V = \frac{\hbar I_c}{2e}\int_{\phi_0}^{\phi} d\phi'\sin(\phi') = \text{const.} - E_J\cos(\phi),$$

where $V = \hbar\dot{\phi}/2e$ and $E_J = \hbar I_c/2e$ are the instantaneous voltage from the Josephson relations and the Josephson energy, respectively.

We can replace the inductor and capacitor of the LC-circuit by a single Josephson junction, which is also a type of capacitor. The n-operator of the capacitive term is the number of Cooper pairs that have tunneled through the junction. The Hamiltonian then becomes

$$\hat{H} = 4E_C\,\hat{n}^2 - E_J\cos(\hat{\phi}). \tag{2.5}$$

Through the expansion $\cos(\phi) = 1 - \phi^2/2 + \phi^4/4! + ...$ we see that the Josephson energy deviates from a linear inductive term by its $\phi^4/4!$ and higher order contributions. The reduced flux and the superconducting phase difference have an exact correspondence, so the same Greek letter has been used for both on purpose. As discussed in the previous section, a flux Φ through a superconducting loop interrupted by a Josephson junction are related by $\phi = 2\pi\Phi/\Phi_0$. With this in mind, the Josephson relation for V is nothing but the definition of magnetic flux through a conducting loop with an ideal voltage source,

$$\Phi(t) = \int_{-\infty}^{t} V(t')dt'.$$

The circuit described in (2.5) is an isolated charge qubit where the two states are based on the quantum number $\hat{n}$, distinguishing between 0 and 1 extra Cooper pairs in a small region of the circuit.

In order to control the qubit energy and set the offset charge, a gate voltage is coupled to the circuit which results in

$$\hat{H}_{charge} = 4E_C(\hat{n} - n_{gate})^2 - E_J \cos(\hat{\phi}). \tag{2.6}$$

E_C is associated with the energy of adding a Cooper pair to the island while E_J is the coupling energy across the junction. It is instructive to think about the charge qubit Hamiltonian as describing a fictitious particle of mass C moving in a cosine potential. Then the phase acts as position and Cooper pair charge $2e\hat{n}$ as momentum. The basic charge qubit, the Cooper-pair box, was first realized experimentally in 1997 [28].

Now we consider the effect of varying the ratio E_J/E_C. If $E_J/E_C \gg 1$, the fictitious particle is localized in a well of the potential such that $\hat{\phi}$ is a good quantum number and the eigenstates will be supported over many $\hat{n}$-states. On the other hand, if $E_J/E_C \ll 1$, the potential is approximately flat and the situation is reversed such that the states are localized in $\hat{n}$. This can be desirable in the other fundamental type of qubit, the flux qubit, where $\hat{\phi}$ plays the role that $\hat{n}$ plays in charge qubits. The flux qubit Hamiltonian is

$$\hat{H}_{flux} = 4E_C\,\hat{n}^2 - E_J \cos(\hat{\phi}) + \frac{1}{2}E_L(\hat{\phi} + 2\pi\Phi_{ext}/\Phi_0)^2, \tag{2.7}$$

where $E_L = \Phi_0^2/4\pi^2 L$ is the inductive energy [5] and Φ_{ext} is the externally applied flux. It is composed by a loop pierced by magnetic flux. When $E_J/E_C \ll 1$, the Cooper pairs can flow continuously, and the two states are the clockwise and anticlockwise currents around the loop, letting 0 or 1 extra magnetic flux quanta through. At $\Phi = \Phi_0/2$ there are two degenerate states and the resulting states are superpositions of currents in opposite directions.

2.3.2   Noise and Errors

Limiting the noise while being able to perform fast and high-fidelity qubit operations is a main challenge for qubits. Noise reduction stands on three legs. It can be reduced either by filtering the present noise away, by correcting the resulting errors or by designing the qubit to be less sensitive to noise [6]. The latter is the type that will be considered here.

Noise causes two distinct types of errors in a qubits, associated with rotation of the Bloch vector in two orthogonal directions; relaxation, the process in which the state of the qubit is flipped, and dephasing, where the noise changes the phase between the two states in superposition.

The error rates, defined as inverse lifetimes, for dephasing and relaxation, are associated to energy dispersion with respect to an external parameter λ and the transition matrix element between the ground and excited states, respectively. Thus, for a lifetime T with respect to dephasing (φ)

or relaxation (1) due to an external parameter λ, we have the relations for the error rates

$$\frac{1}{T_\varphi^\lambda} \propto \left|\frac{\partial E_{01}}{\partial \lambda}\right|^2$$

$$\frac{1}{T_1^\lambda} \propto \left|\langle 0| \hat{O} |1\rangle\right|^2$$

where E_{01} is the transition energy between the states and $\hat{O}$ is the relevant qubit operator, for example the charge operator for a charge qubit. Both can be reduced by proper qubit design.

Using the charge qubit as an example, the tunable n_g comes at an expense. The charge qubit couples to the environment through n_g, so that is becomes sensitive to charge noise; uncontrolled fluctuations of electric field in the environment, which causes dephasing of the charge qubit.

A flux qubit is correspondingly affected by flux noise. It should be noted that charge noise (in units of e) generally has an amplitude two orders of magnitude larger than flux noise (in units of Φ_0), so limiting charge noise is first priority.

In order to protect the qubit against dephasing, one should aim for flat dispersion of the qubit transition energy with respect to the control parameters. One might find an operational *sweet spot*, which means $\partial E_{01}/\partial \lambda$ is zero to first order. In order to protect against relaxation, the two states should live in distinct regions in the qubit parameter space such that only exponentially reduced tails of the wavefunctions are overlapping. For a periodic potential, the desired feature we are looking for in this context is two minima within a unit cell since we can then be able to confine a qubit wavefunction to each of the minima.

There has been invested much effort in improving the fundamental qubits. One can add various circuit elements or replace Josephson junctions with SQUID's to tune the critical current as discussed Section 2.2, all of which allows to fine-tune the qubit by modifying the potential and changing the performance of the qubits in the desired way. Characteristic for all of these variations is that each improvement generally comes with a trade-off.

An example can be made with the probably most famous and widely used qubit so far, namely the transmon. This is a charge qubit described by (2.6) with a large capacitance, corresponding to a heavy particle moving in the cosine potential such that $E_J/E_C \gg 1$. Where the original charge qubit was severely limited by charge noise, changing to the heavy regime of the transmon made the qubit close to charge-insensitive. This, on the other hand, reduces the anharmonicity and results in a larger transition matrix element, making the transmon more sensitive to relaxation [6].

In the end, the flux and charge qubits and variations of those, cannot be protected against both types of errors simultaneously, as the previous discussion should illustrate. It is necessary to combine flux and charge modes in the qubit design to protect it against both dephasing and relaxation. We call these qubits, shielded against noise through hardware, protected qubits.

2.3.3 Protected Qubits

Recall the Josephson potential $-E_J \cos(\phi)$, where ϕ is the phase picked up by a Cooper pair tunneling over the junction. If we could replace the Josephson junction of the transmon with another element with the potential $-E_J \cos(2\phi)$, there would be two minima per unit cell, which would open up for the option of a ground- and excited state confined to separate wells, securing good protection against relaxation. Physically, this modification corresponds to tunneling of *pairs* of Cooper pairs. Different strategies to suppress single Cooper pair tunneling have been proposed, e.g. [29] and [30]. In [29], the Josephson junction of the transmon is replaced by symmetric SQUID-like structure with added inductors, pierced by a magnetic field of half a flux quantum. This only allows for simultaneous Cooper pair tunneling over both junctions, resulting in the desired potential. It has two nearly degenerate ground states, and the Hamiltonian conserves the parity of the Cooper pair number, both of which contributes to protection of the qubit; the former by ensuring a vanishing energy dispersion and the second by prohibiting relaxation to states of opposite parity, provided symmetry obedience of the related noise [6]. The decoherence times expected for this $\cos(2\phi)$-qubit proposal at optimal parameter choices are reported to be one order of magnitude larger than for the transmon.

The main downside to protected qubits protected against relaxation is that it becomes cumbersome to perform gates, which can be thought of as rotations of the quantum state in the qubit state Bloch Sphere. A perfectly isolated quantum system cannot be manipulated, and a qubit is not of much use without the ability to participate in gate operations.

When the states live in the same potential well, one simply drives transitions between the states by applying electromagnetic radiation of the transition frequency. Now, when the states are separated such that their overlap vanishes, it often causes a significant increase in the time it takes to perform the gate, calling for a different method. A common approach in this case is to include a third state of the system of higher energy, that couples to both of the qubit states, as an intermediary between the transitions. This necessarily results in higher losses and increases decoherence.

In Ref. [31] an alternative approach is presented, discussing a variable barrier height between the potential wells as a possible solution. The qubit proposed in this context is a double-shunted flux qubit (DSFQ), shown in Figure 2.6. It consists of a loop of three Josephson junctions, pierced by a magnetic flux quantum at a value around $\Phi_0/2$, creating a double-well potential in the two-dimensional space spanned by the two independent phases. Two of the junctions are shunted by large capacitors such that $E_J/E_C \gg 1$, confining the two quasi-degenerate states to their respective wells, ensuring good protection against relaxation. This simultaneously protects the two charge modes from dephasing due to charge noise. Contrarily, the qubit is sensitive to flux noise, which is cleverly accounted for by adding an additional loop, forcing the currents to circulate in opposite directions, which turns out to cancel fluctuations in global flux.
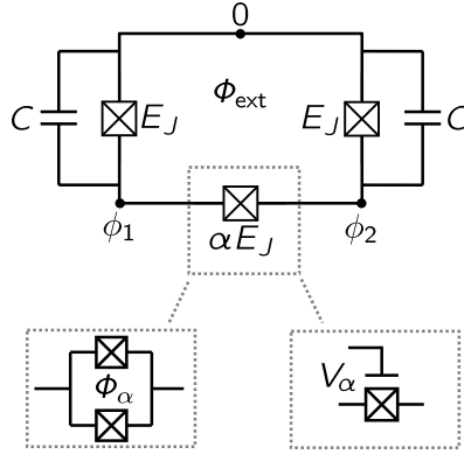
Figure 2.6: The Double Shunted Flux Qubit (DSFQ) consists of a flux-biased loop of three Josephson junctions, of which one has a variable energy.

They key point of this paper is that the energy of the third Josephson junction is variable. Where the two shunted junctions have energy E_J, the third has a tunable energy αE_J. By lowering α, the barrier between the two wells can be flattened completely. The paper numerically inspect the performance of gates by a procedure where the barrier is lowered from $\alpha = 1$ to a lower barrier level where a microwave pulse is applied, performing a rotation, after which α is cranked up to its initial value. Two-qubit gates are also demonstrated. The gate times and the quality of the gate operations fall within a regime comparable to gates schemes of existing qubits [5].

The above discussion illustrates that there are many considerations to take into account and ever-recurring tradeoffs at essentially every decision, already when considering the qubit design and parameter choices in relation to noise and gate times. Many different approaches are being tested in parallel. The DSFQ is an example of a modern qubit standing on the shoulders of the past decades of development from the very first superconducting qubits.

2.4 Multiterminal Josephson Junctions

When adding a third superconducting terminal to the junction, the Cooper tunneling across the junction depends on the additional superconducting phase, resulting in the three-terminal Josephson junction being dependent on two independent phase variables. For each additional terminal, one phase is added such that the properties of an n-terminal junction is a function of $n-1$ independent phases. These additional degrees of freedom give rise to new phenomena that were reviewed in the introduction. This section supplements the introductory review with the more detailed introduction of Shapiro steps in 2.4.1, both in the context of two- and multiterminal junctions. In 2.4.2 it will be discussed how Andreev reflections generalize when additional terminals are coupled to the same weak link.

2.4.1 Shapiro Steps

Shapiro steps in Josephson junctions were first described in 1963 by S. Shapiro [32]. Consider a conventional two-terminal Josephson junction exposed to microwave radiation of frequency ω_r. If there is a voltage bias V_0, it is modified as $V_0 \to V_0 + V_r \cos(\omega_r t)$. The junction phase locks to the phase of the drive, and the DC $I - V$ curve then shows plateaus at voltages equal to integer multiples of $\hbar\omega_r/2e$ [1]. The result can as well been achieved by applying periodically varying bias currents [33]. However, if the Josephson junction is described by a non-sinusoidal Josephson current, skewing the washboard potential, Shapiro steps may occur in fractions of $h\omega_r/2e$ [34]. The characterization of the Josephson dynamics under a microwave drive can therefore serve as a probe into the current-phase relation of the junction [11].

In the context of multiterminal Josephson junctions, fractional Shapiro steps is an inherent property due to the higher dimensionality of the washboard potential. Fractional Shapiro steps result in a DC $I - V$ curve of a so-called devil's staircase structure [35], meaning that the most prominent fraction is $1/2$.

Fractional Shapiro steps in a three-terminal Josephson junction has been studied in detail in Ref. [11]. The following explanation serves some understanding to why fractional steps occur in junctions with $n > 2$. In the two-dimensional generalization of the tilted washboard model, which is presented in Section 5.1, Shapiro steps emerge when the DC current bias, which tilts the washboard, is combined with an AC bias that causes vibration of the washboard. If there is no DC bias, the fictitious particle moves in closed ellipses. With a DC bias, it rolls down the washboard in a spiral. If the trajectory is back at the potential minimum after one cycle, it has the same frequency ω_r as the drive. Now, a new possibility for the two-dimensional washboard compared the the one-dimensional is that the particle eventually lands on a saddle-point of the washboard after one cycle. If it takes in total two cycles before reaching the minimum, the trajectory has a cycle of frequency $\omega_r/2$. This way, fractional Shapiro steps appear.

2.4.2 Andreev Reflection and Multiplets

As well as the addition of superconducting leads to the junction introduces additional phases, multiple Andreev reflections can take now place involving more than two leads. In the case of one Andreev reflection (AR), there is the possibility discussed previously involving one pair of superconducting leads, where an electron from one terminal is reflected at a second terminal and absorbed again at the first terminal. If there are three terminals with Terminal 3 grounded, this happens at $eV_1 = \pm\Delta, eV_2 = \pm\Delta$ and $e(V_2 - V_1) = \pm\Delta$. In general, the electron from lead α can be reflected as a hole at lead β and absorbed at lead γ, which accommodate six additional options, namely $2V_2 - V_1 = \pm2\Delta/e$, $2V_1 - V_2 = \pm2\Delta/e$ and $V_1 + V_2 = \pm2\Delta/e$. These enable the transitions $1 \to 2 \to 3$ or vice versa, $1 \to 3 \to 2$ or vice versa and $2 \to 1 \to 3$ or vice versa, respectively. For each additional number of AR's, double as many new voltage relations arise

(including the two-terminal cases of e.g. $1 \rightarrow 2 \rightarrow 1 \rightarrow 2$). In general for n terminals and m AR's, there are $n(n-1)^{m+1}$ different voltage relations that in principle will be visible as peaks in the conductance. Summing up any number of AR's in the case of three terminals with number three grounded, the multiple Andreev reflection (MAR) condition $nV = 2\Delta/e$ generalizes to

$$pV_1 + qV_2 = 2\Delta/e \qquad p, q \in \mathbb{Z}.$$

These lines can be visible as peaks in the conductance as a function of low voltages, forming a subharmonic gap structure (SGS) [36]. Another condition giving rise to SGS is

$$pV_1 + qV_2 = 0.$$

According to [26], this can be explained by opening and closing of transport processes via MAR. However, more recently, the supercurrent in a three-terminal Josephson junction at $V_2 = -V_1$ has been demonstrated to be carried by *quartets*, which are entangled sets of four electrons, and simultaneously MAR as a possible mechanism was ruled out [37]. An approximation of the ABS energies under antisymmetric and low bias conditions was shown to yield a supercurrent proportional to $4e$, supporting the perception that the charge carrier is composed by four electrons. The quartet is formed in Lead 3 as follows: A Cooper pair is transferred from both Lead 1 and Lead 2 and two Cooper pairs are formed in Lead 3 via crossed Andreev reflection (CAR), which can be thought of as the conversion between electron and hole in a normal metal through a superconductor, in which a Cooper pair is formed [38]. When this happens from both leads at the same rate, the two Cooper pairs are broken up to form a quartet. This requires a length of the superconducting lead smaller or equal to the superconducting coherence length. Both CAR and MAR can only take place in a small region where all junctions meet, and can be suppressed by design [10].

Generalizing this, the physical origin of the supercurrent at voltages fulfilling $pV_1 + qV_2 = 0$ is the splitting of Cooper pairs to form entangled sets of $4 + 2n$ electrons, so-called *multiplets* [37]. Depending on the number of entangled electrons, these are called quartets, sextets, octets etc.

In spite of the indisputably quantum mechanical nature of this process, multiplets also arise from simulations of the classical RCSJ model, as was shown in a very recent paper [10]. Hence there must be an explanation within this classical framework. In Ref. [10], the stability of the quartet resonance was found to be analogous to the stability of inverted position of the pendulum in Kapitza's pendulum problem. This will be elaborated in section 5.2.3. In Ref. [9] it is backed up that *"differential resistance measurements alone are insufficient to conclusively distinguish resonant Andreev reflection processes from semi-classical circuit-network effects"*.

3 Quantum Dot coupled to an n-terminal Josephson Junction

In this section, a Hamiltonian describing an n-terminal Josephson junction will be derived. From this, we will analyze the resulting energy spectrum in Section 3.2 and the form of the supercurrent between the terminals in Section 3.3.

We start by constructing the simplest reasonable model we can imagine to describe n terminals coupled through a quantum dot (QD). This way, we can extract the essence of the physics of the system before eventually introducing more accurate corrections which raise the complexity of the problem. An exact theoretical description is only possible when Coulomb interaction between particles on the dot is neglected [22].
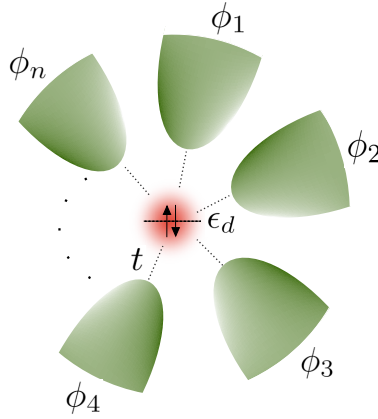

Figure 3.1: Model of an n-terminal Josephson junction coupled to a quantum dot.

The QD in this model has a single energy level ϵ_d , such that it can host two electrons of opposite spin. Closely around the QD we have n superconducting electrodes each described by a mean-field BCS Hamiltonian with pairing potential Δ of equal magnitude but varying in phase. The superconductors are distributed symmetrically around the QD which allows for tunneling of equal magnitude between each superconductor and the QD. A representation of the model is shown in Figure 3.1.

The Hamiltonian of this system is given by

$$\hat{H} = \hat{H}_d + \sum_{j=1}^{n} \hat{H}_{S_j} + \sum_{j=1}^{n} \hat{H}_{T_j},$$

representing the QD, superconductors and tunnel couplings, respectively, with

$$\hat{H}_d = \epsilon_d \sum_{\sigma} d_\sigma^\dagger d_\sigma$$

$$\hat{H}_{S_j} = \sum_{\mathbf{k}\sigma} \epsilon_{\mathbf{k}} c_{\mathbf{k}\sigma j}^\dagger c_{\mathbf{k}\sigma j} - \Delta \sum_{\mathbf{k}} \left(c_{\mathbf{k}\uparrow j}^\dagger c_{-\mathbf{k}\downarrow j}^\dagger + c_{-\mathbf{k}\downarrow j} c_{\mathbf{k}\uparrow j} \right)$$

$$\hat{H}_{T_j} = \sum_{\mathbf{k}\sigma} (t_j d_\sigma^\dagger c_{\mathbf{k}\sigma j} + t_j^* c_{\mathbf{k}\sigma j}^\dagger d_\sigma).$$

In order to justify neglecting Coulomb interaction, we impose the condition of strong coupling $\Gamma \gg U$ for the hybridization $\Gamma = \pi|t|^2\rho_0$ and the Coulomb energy U between two particles on the QD, where ρ_0 is the density of states around the Fermi energy approximated as a constant.

$\hat{H}_{S_j}$ is given on the form of a BCS mean-field Hamiltonian with the pairing potential $\Delta = V\sum_{\mathbf{k}}\langle c_{\mathbf{k}\uparrow}c_{-\mathbf{k}\downarrow}\rangle$. Furthermore, we have used imposed the symmetry on our system that the tunneling amplitudes t between the superconducting leads and the QD are independent on $\mathbf{k}$ and equal for all j channels.

The superconducting gap Δ is independent on $\mathbf{k}$ in BCS theory [1] where the potential strength $V_{\mathbf{k}\mathbf{k}'}$ for scattering a Cooper pair from $(\mathbf{k}', -\mathbf{k}')$ to $(\mathbf{k}, -\mathbf{k})$ is taken to be constant $-V$ in a narrow region within the Fermi energy, containing all relevant energies for electrons forming pairs, and zero elsewhere. The energies $\epsilon_{\mathbf{k}}$ and superconducting gaps are all of equal magnitude but are allowed to vary in phase, which will be important for the spectrum and supercurrents in the system.

The phase of each superconducting gap $\Delta_j = |\Delta|e^{i\phi_j}$ has been absorbed by the tunneling amplitudes by the transformation $c_{\mathbf{k}\sigma j} \to c_{\mathbf{k}\sigma j}e^{i\phi_j/2}$ such that $\Delta_j \to |\Delta|$ and $t \to |t|e^{i\phi_j/2}$. The tunneling amplitude t_j thus refer to $|t|^{i\phi_j/2}$ in the following, while the gap is simply the real number Δ.

3.1   Deriving the Low-energy Effective Hamiltonian

As a first step towards examining the system, the quantum dot's Green's function is derived. This method was also used in e.g. Ref. [22].

In absence of the Cooper pairing we could find the Green's function readily using the equation of motion technique [39], but because of the correlations brought into the system by the Cooper pairings' $c^\dagger c^\dagger$-terms, it is no longer solvable this way. Fortunately, in this case it turns out if we first transform the system to Nambu space, we can solve it by using exactly the same method, just in a two-dimensional vector space. This is done by introducing the Nambu spinors

$$\psi_{kj} = \begin{pmatrix} c_{\mathbf{k}\uparrow j} \\ c^\dagger_{-\mathbf{k}\downarrow j} \end{pmatrix} \qquad \psi_d = \begin{pmatrix} d_\uparrow \\ d^\dagger_\downarrow \end{pmatrix}$$

and the matrices

$$H_d = \begin{pmatrix} \epsilon_d & 0 \\ 0 & -\epsilon_d \end{pmatrix} \qquad H_S = \begin{pmatrix} \epsilon_{\mathbf{k}} & -\Delta \\ -\Delta & -\epsilon_{\mathbf{k}} \end{pmatrix} \qquad H_{T_j} = \begin{pmatrix} t_j & 0 \\ 0 & -t_j^* \end{pmatrix}.$$

The original Hamiltonian is then recovered by the relation

$$\hat{H} = \psi_d^\dagger H_d \psi_d + \epsilon_d + \sum_{\mathbf{k}j}\left(\psi_{kj}^\dagger H_S \psi_{kj} + \epsilon_{\mathbf{k}}\right) + \sum_{\mathbf{k}j}\left(\psi_d^\dagger H_{T_j}\psi_{kj} + \psi_{kj}^\dagger H_{T_j}^\dagger \psi_d\right).$$

While the usual Matsubara Green's function for the QD is $\hat{G}_{dd,\sigma}(\tau) = -\left\langle T_\tau\left[d_\sigma(\tau)d_\sigma^\dagger(\tau)\right]\right\rangle$, the

Matsubara Green's function in Nambu formalism is the matrix

$$G_{dd}(\tau) = -\left\langle T_\tau\left[\psi_d(\tau)\psi_d^\dagger(0)\right]\right\rangle = -\begin{pmatrix} \langle T_\tau[d_\uparrow(\tau)d_\uparrow^\dagger(0)]\rangle & \langle T_\tau[d_\uparrow(\tau)d_\downarrow(0)]\rangle \\ \langle T_\tau[d_\downarrow^\dagger(\tau)d_\uparrow^\dagger(0)]\rangle & \langle T_\tau[d_\downarrow^\dagger(\tau)d_\downarrow(0)]\rangle \end{pmatrix}.$$

Note that the operators in Nambu space has been defined without hats in order two distinguish between the two. Using the short-hand notation $\partial_\tau \equiv \frac{\partial}{\partial\tau}$, the imaginary time-derivative of an element of $G_{dd}(\tau)$ is

$$-\partial_\tau G_{dd}(\tau)_{ij} = \partial_\tau\left(\theta(\tau)\left\langle\psi_{d,i}(\tau)\psi_{d,j}^\dagger(0)\right\rangle \pm \theta(-\tau)\left\langle\psi_{d,j}^\dagger(0)\psi_{d,i}(\tau)\right\rangle\right)$$
$$= \delta(\tau)\left\langle\psi_{d,i}(\tau)\psi_{d,j}^\dagger(0) \mp \psi_{d,j}^\dagger(0)\psi_{d,i}(\tau)\right\rangle + \left\langle T_\tau\left[\partial_\tau\psi_{d,i}(\tau)\psi_{d,j}^\dagger(0)\right]\right\rangle$$

using that $\delta(-\tau) = -\delta(\tau)$. Upper and lower signs are for bosons and fermions, respectively.

With the imaginary-time dependence of an operator defined as $A(\tau) = e^{\tau\hat{H}}Ae^{-\tau\hat{H}}$, we get the imaginary-time Heisenberg equation $\partial_\tau A(\tau) = [\hat{H}, A](\tau)$, A being time-independent in the Schrödinger picture, such that $\partial_\tau\psi_d(\tau) = [\hat{H}, \psi_d](\tau)$. As a further reduction, the time-dependence in the first term can be dropped because of the delta function and we can see that

$$\sum_{ij}(\psi_{d,i}\psi_{d,j}^\dagger \mp \psi_{d,j}^\dagger\psi_{d,i}) = \begin{pmatrix} [d_\uparrow, d_\uparrow^\dagger]_\mp & [d_\uparrow, d_\downarrow]_\mp \\ [d_\downarrow^\dagger, d_\uparrow^\dagger]_\mp & [d_\downarrow^\dagger, d_\downarrow]_\mp \end{pmatrix} = \mathbb{1}$$

with the notation $[A, B]_+$ for anticommutator. Hence, the time-derivative of the dot's Green's function reduces to

$$-\partial_\tau G_{dd}(\tau) = \delta(\tau)\mathbb{1} + \left\langle T_\tau\left[\left[\hat{H}, \psi_d\right](\tau)\psi_d^\dagger(0)\right]\right\rangle. \tag{3.1}$$

Thus, we proceed by evaluating the two commutators

$$[\hat{H}, d_\uparrow] = \epsilon_d\sum_\sigma[d_\sigma^\dagger d_\sigma, d_\uparrow] + \sum_{\mathbf{k}\sigma j}t_j[d_\sigma^\dagger c_{\mathbf{k}\sigma j}, d_\uparrow] = -\epsilon_d d_\uparrow - \sum_{\mathbf{k}j}t_j c_{\mathbf{k}\uparrow j}$$

$$[\hat{H}, d_\downarrow^\dagger] = \epsilon_d\sum_\sigma[d_\sigma^\dagger d_\sigma, d_\downarrow^\dagger] + \sum_{\mathbf{k}\sigma j}t_j^*[c_{\mathbf{k}\sigma j}^\dagger d_\sigma, d_\downarrow^\dagger] = \epsilon_d d_\downarrow^\dagger + \sum_{\mathbf{k}j}t_j^* c_{\mathbf{k}\downarrow j}^\dagger$$

Collecting the two results, we see that since the $\mathbf{k}$-sum is symmetric around k=0 such that $\sum_{\mathbf{k}}c_{\mathbf{k}}^\dagger = \sum_{\mathbf{k}}c_{-\mathbf{k}}^\dagger$, they can be expressed in the single vector equation

$$[\hat{H}, \psi_d] = -H_d\psi_d - \sum_{\mathbf{k}j}H_{T_j}\psi_{kj}.$$

Inserting this in (3.1),

$$-\partial_\tau G_{dd}(\tau) = \delta(\tau)\left\langle\psi_d\psi_d^\dagger \mp \psi_d^\dagger\psi_d\right\rangle - H_d\left\langle T_\tau\left[\psi_d(\tau)\psi_d^\dagger(0)\right]\right\rangle - \sum_{\mathbf{k}j}H_{T_j}\left\langle T_\tau\left[\psi_{kj}(\tau)\psi_d^\dagger(0)\right]\right\rangle$$

and recognizing that

$$G_{kd}(\tau) = -\left\langle T_\tau\left[\psi_{kj}(\tau)\psi_d^\dagger(0)\right]\right\rangle,$$

we end with the compact equation of motion

$$-\partial_\tau G_{dd}(\tau) = \delta(\tau)\mathbb{1} - H_d G_{dd}(\tau) - \sum_{\mathbf{k}j}H_{T_j}G_{kd}(\tau). \tag{3.2}$$

Since $\partial_\tau G_{dd}(\tau)$ depends on $G_{kd}(\tau)$, we go on to find the equation of motion of the latter. Similarly to above,

$$-\partial_\tau G_{kd}(\tau) = -\left\langle T_\tau\left[[\hat{H}, \psi_{kj}](\tau)\psi_d^\dagger(0)\right]\right\rangle, \tag{3.3}$$

where the $\delta(\tau)$-term cancels because all the matrix elements are proportional to commutators between d and c operators. We evaluate the commutators

$$[\hat{H}, c_{\mathbf{k}'\uparrow j'}] = \sum_{\mathbf{k}\sigma j}\epsilon_{\mathbf{k}}[c_{\mathbf{k}\sigma j}^\dagger c_{\mathbf{k}\sigma j}, c_{\mathbf{k}'\uparrow j'}] - \Delta\sum_{\mathbf{k}j}[c_{\mathbf{k}\uparrow j}^\dagger c_{-\mathbf{k}\downarrow j}^\dagger, c_{\mathbf{k}'\uparrow j'}] + \sum_{\mathbf{k}\sigma j}t_j^*[c_{\mathbf{k}\sigma j}^\dagger d_\sigma, c_{\mathbf{k}'\uparrow j'}]$$

$$= -\epsilon_{\mathbf{k}'}c_{\mathbf{k}'\uparrow j'} + \Delta c_{-\mathbf{k}'\downarrow j'}^\dagger - t_{j'}^* d_\uparrow$$

$$[\hat{H}, c_{-\mathbf{k}'\downarrow j'}^\dagger] = \sum_{\mathbf{k}\sigma j}\epsilon_{\mathbf{k}}[c_{\mathbf{k}\sigma j}^\dagger c_{\mathbf{k}\sigma j}, c_{-\mathbf{k}'\downarrow j'}^\dagger] - \Delta\sum_{\mathbf{k}j}[c_{-\mathbf{k}\downarrow j}c_{\mathbf{k}\uparrow j}, c_{-\mathbf{k}'\downarrow j'}^\dagger] + \sum_{\mathbf{k}\sigma j}t_j[d_\sigma^\dagger c_{\mathbf{k}\sigma j}, c_{-\mathbf{k}'\downarrow j'}^\dagger]$$

$$= \epsilon_{\mathbf{k}'}c_{-\mathbf{k}'\downarrow j'}^\dagger + \Delta c_{\mathbf{k}'\uparrow j'} + t_{j'}d_\downarrow^\dagger$$

which we use the Nambu matrices to express as

$$[\hat{H}, \psi_{kj}] = -H_S\psi_{kj} - H_{T_j}^\dagger\psi_d$$

and insert in (3.3) to get

$$-\partial_\tau G_{kd}(\tau) = H_S\left\langle T_\tau\left[\psi_{kj}(\tau)\psi_d^\dagger(0)\right]\right\rangle + H_{T_j}^\dagger\left\langle T_\tau\left[\psi_d(\tau)\psi_d^\dagger(0)\right]\right\rangle = H_S G_{kd}(\tau) + H_{T_j}^\dagger G_{dd}(\tau)$$

$$G_{kd}(\tau) = (-\partial_\tau - H_S)^{-1}H_{T_j}^\dagger G_{dd}(\tau). \tag{3.4}$$

After Fourier transformation, which simply results in the substitutions $\tau \to i\omega_n$ and $\partial_\tau \to -i\omega_n$, (3.4) is inserted in (3.2) to obtain the expression for the quantum dot's Green's function

$$G_{dd}(i\omega_n) = \left(i\omega_n\mathbb{1} - H_d - \sum_{\mathbf{k}j}H_{T_j}(i\omega_n\mathbb{1} - H_S)^{-1}H_{T_j}^\dagger\right)^{-1} = \left(g_d^{-1} - \sum_{\mathbf{k}j}H_{T_j}g_{jk}H_{T_j}^\dagger\right)^{-1} \tag{3.5}$$

where we have defined the bare dot and bare lead Green's functions, i.e. in the case of $t = 0$, as the lowercase g_d and g_{jk}.

In order to obtain a solution in a single matrix, we proceed by assuming a wide, flat conduction band by which is meant that it has a constant density of states ρ_0, allowing for converting the $\mathbf{k}$-sum into an energy integral as $\sum_{\mathbf{k}} \to \rho_0\int d\epsilon$. With the width taken to infinity, the bare Green's function for the j'th lead becomes

$$g_j = \sum_{\mathbf{k}}g_{jk} = \sum_{\mathbf{k}}(i\omega_n\mathbb{1} - H_S)^{-1} = \sum_{\mathbf{k}}\frac{-1}{\epsilon_{\mathbf{k}}^2 + \Delta^2 - (i\omega_n)^2}\begin{pmatrix} i\omega_n + \epsilon_{\mathbf{k}} & -\Delta \\ -\Delta & i\omega_n - \epsilon_{\mathbf{k}} \end{pmatrix}$$

$$\to \rho_0\int_{-\infty}^{\infty}d\epsilon\,\frac{1}{\epsilon^2 + \Delta^2 - (i\omega_n)^2}\begin{pmatrix} -i\omega_n - \epsilon & \Delta \\ \Delta & -i\omega_n + \epsilon \end{pmatrix} = \frac{\pi\rho_0}{\sqrt{\Delta^2 - (i\omega_n)^2}}\begin{pmatrix} -i\omega_n & \Delta \\ \Delta & -i\omega_n \end{pmatrix} \tag{3.6}$$

by noting that the integral with ϵ in the numerator cancels because the integrand is odd. Note that the bare lead Green's function is independent on j regardless of the approximation. Using

(3.6), we can readily write down the solution for the QD's Green's function in the infinite, flat band approximation

$$G_{dd}(i\omega_n) \approx \frac{1}{\text{Det}(G_{dd}^{-1}(i\omega_n))} \begin{pmatrix} i\omega_n(1+nf(i\omega_n)) + \epsilon_d & -\Delta f(i\omega_n) \sum_j e^{i\phi_j} \\ -\Delta f(i\omega_n) \sum_j e^{-i\phi_j} & i\omega_n(1+nf(i\omega_n)) - \epsilon_d \end{pmatrix}$$

$$\text{Det}(G_{dd}^{-1}(i\omega_n)) = (i\omega_n)^2(1+nf(i\omega_n))^2 - \epsilon_d^2 - \Delta^2 f^2(i\omega_n) \sum_{ij} \cos(\phi_i - \phi_j), \quad f(i\omega_n) = \frac{\Gamma}{\sqrt{\Delta^2 - (i\omega_n)^2}}$$

where we recall that the hybridization is $\Gamma = \pi\rho_0|t|^2$. Taking the limit of large gap $\Delta \to \infty$, the Green's function becomes

$$g_j \to \lim_{\Delta \to \infty} \frac{\pi\rho_0}{\sqrt{\Delta^2 - (i\omega_n)^2}} \begin{pmatrix} -i\omega_n & \Delta \\ \Delta & -i\omega_n \end{pmatrix} = \pi\rho_0\sigma_x,$$

which makes it independent on frequency. We use this to define the *effective low-energy Hamiltonian*

$$H_{\text{eff}} = i\omega_n \mathbb{1} - G_{dd}^{-1}(i\omega_n) = \epsilon_d\sigma_z - \Gamma \begin{pmatrix} 0 & \sum_j e^{i\phi_j} \\ \sum_j e^{-i\phi_j} & 0 \end{pmatrix} = \epsilon_d\sigma_z - \Gamma \sum_j \left(\cos\phi_j \sigma_x - \sin\phi_j \sigma_y \right) = \mathbf{d}\cdot\boldsymbol{\sigma}$$

(3.7)

with $\mathbf{d}^T = \begin{pmatrix} -\Gamma\sum_j \cos\phi_j & \Gamma\sum_j \sin\phi_j & \epsilon_d \end{pmatrix}$ that may be interpreted as an effective magnetic field in Nambu space. This conveniently allows us to treat the system as non-interacting since the proximity effect has been absorbed into H_d such that $G_{dd}^{-1}(i\omega_n) = i\omega_n \mathbb{1} - H_{\text{eff}}$ has the form of an uncoupled QD's Green's function g_d. Since it contains exactly the same physics as the original interacting system, we call this an *effective* Hamiltonian. It is valid for low energies since we took the limit $\Delta \to \infty$ which means that the frequencies of the system are much smaller than the gap. This results in the QD only coupling to the Cooper pairs of the superconductors since the quasiparticle excitations are far in energy. The coupling between the QD and superconductor is determined by ρ_0, $|t|$ through the hybridization Γ and the phases ϕ_j.

Transforming back from Nambu space gives the result

$$\hat{H}_{\text{eff}} = \psi_d^\dagger H_{\text{eff}} \psi_d = \epsilon_d \sum_\sigma d_\sigma^\dagger d_\sigma - \Gamma \sum_j \left(e^{i\phi_j} d_\uparrow^\dagger d_\downarrow^\dagger + e^{-i\phi_j} d_\downarrow d_\uparrow \right). \tag{3.8}$$

We have hereby gone from a description of two coupled systems to a local description of our system of interest, namely the QD. Here we see how the QD's Hamiltonian is modified due to the proximity effect. A zero-momentum Cooper-pair excitation term is added to the original diagonal term, which induces the correlations in the dot that are characteristic for superconductors. With this description, the effect of the superconductor has been moved to a local property at the QD such that its Hamiltonian (3.8) has the mean-field BCS form itself with $|\Gamma\sum_j e^{i\phi_j}|^2$ as the minimal excitation energy. Exactly like in a superconductor, there is now a gap in the density of states of the QD.

3.2 Energy Spectrum

We have already seen that the physics of the QD is highly modified due to the proximity of the superconductors. In this section we will see how the energy spectrum changes. From the effective Hamiltonian $H_{\text{eff}} = \mathbf{d} \cdot \boldsymbol{\sigma}$ the eigenenergies are found readily as $\pm \varepsilon = \pm |\mathbf{d}|$, which gives

$$\pm \varepsilon = \pm \sqrt{\epsilon_d^2 + \Gamma^2 \sum_{ij} \cos(\phi_i - \phi_j)}. \tag{3.9}$$

The important feature is that in the low-energy regime, this pair of eigenenergies lie inside the gap Δ in the density of states, symmetrically distributed around zero energy, and are thus the energies of the two Andreev Bound States (ABS) that have emerged; a signature of the proximity effect.

The result can be compared to the excitation energy of the BCS Hamiltonian $E_{\mathbf{k}} = \sqrt{\epsilon_{\mathbf{k}}^2 + |\Delta|^2}$ Here, Δ acts as the lowest energy of the excitation continuum while in our case the energies are discrete because we are living on a system of a single energy level.

A difference is that in the case of the QD, the size of the gap is variable through the phases. The sum of cosines can take any value between 0 and n^2. The latter is achieved for $\phi_j = 0 \; \forall j$ while the former happens when all phases are evenly distributed around the unit circle, for example $0, \pi/2, \pi$ and $3\pi/2$ in the case of a four-terminal junction.

It is curious that the supercurrents across the junction can screen the effect from the superconductors from the QD, such that they are decoupled for this special phase configuration. The argument for the sum of cosines cancelling in this case is as follows. If the phases are evenly distributed, the spacing between each is $2\pi/n$. If the phases are adjusted such that one of the phases is zero, it is easy to see that in the case of even n, the values of the phases are symmetric with respect to inversion around the vertical axis, because of which the cosines to all phase differences cancel except for $i = j$ and for $\phi_i - \phi_j = \pi$. To conclude, for n even, $\sum_{ij} \cos(\phi_i - \phi_j) = n + n \cos(\pi) = 0$.

In general, the sum can be rewritten as

$$\sum_{ij} \cos(\phi_i - \phi_j) = n \sum_{i=0}^{n} \cos(\phi_i) = n \sum_{i=0}^{n-1} \text{Re}\{z^i\},$$

where the complex number $z = e^{2\pi i/n}$ was introduced. The sum can be rewritten using the sum of a finite geometric series

$$\sum_{i=0}^{n-1} z^i = \frac{1 - z^n}{1 - z}.$$

Noting that $z^n = 1$, the sum is zero and the proof is complete. Hence the ABS energies lie in the range $\varepsilon \in [\epsilon_d; \sqrt{\epsilon_d^2 + n^2 \Gamma^2}]$ for any n.

The energy spectrum is shown in Figure 3.1. When the contributions from the superconductors cancel, the energy spectrum reduces to that of a normal metal, $E = \{0, \epsilon_d, 2\epsilon_d\}$ for the 0-, 1- and 2-particle eigenstates, respectively, shown as dotted lines in the figure.
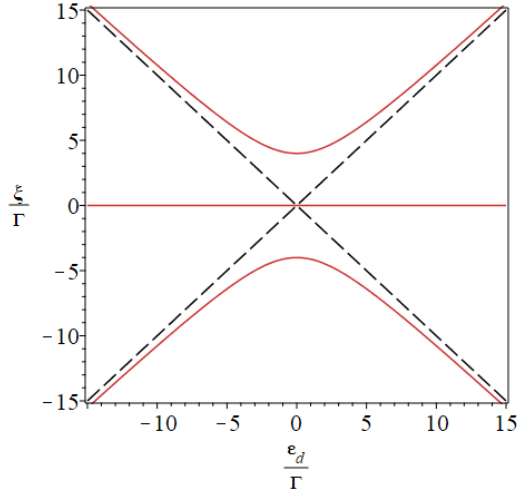
Figure 3.1: The three energy levels (orange) of the effective Hamiltonian of the quantum dot for maximal energy gap $\varepsilon = \sqrt{\epsilon_d^2 + n^2\Gamma^2}$ with $n = 4$. $\xi = E - \epsilon_d$. Normal metal energies are sketched with dashed lines. The gap has size $E = 2\Gamma\sqrt{\sum_{ij}\cos(\phi_i - \phi_j)}$. For $0 < \sum_{ij}\cos(\phi_i - \phi_j) < n^2$, the curve is in the area between the dashed lines and orange curves.

The corresponding (unnormalized) eigenstates are found to be

$$|\pm\rangle = \begin{pmatrix} -\Gamma\sum_j e^{i\phi_j} \\ \pm\varepsilon - \epsilon_d \end{pmatrix}.$$

Meanwhile, from (3.8) we see that $\hat{H}_{\text{eff}}$ has spin-degenerate eigenstates $|\uparrow\rangle$ and $|\downarrow\rangle$ with eigenenergy ϵ_d. To see how these two pictures fit, it is illuminating to write $\hat{H}_{\text{eff}}$ in the basis of all states where we find

$$\hat{H}_{\text{eff}} = \begin{pmatrix} |\uparrow\downarrow\rangle & |0\rangle & |\uparrow\rangle & |\downarrow\rangle \end{pmatrix} \begin{pmatrix} \epsilon_d & -\Gamma\sum_j e^{i\phi_j} & 0 & 0 \\ -\Gamma\sum_j e^{-i\phi_j} & -\epsilon_d & 0 & 0 \\ 0 & 0 & 0 & 0 \\ 0 & 0 & 0 & 0 \end{pmatrix} \begin{pmatrix} \langle\uparrow\downarrow| \\ \langle 0| \\ \langle\uparrow| \\ \langle\downarrow| \end{pmatrix},$$

which contains all four solutions:

$$\text{Energy } \epsilon_d \pm \varepsilon: \qquad |\pm\rangle = (\pm\varepsilon - \epsilon_d)|0\rangle - \Gamma\sum_j e^{i\phi_j}|\uparrow\downarrow\rangle \tag{3.10}$$

$$\text{Energy } \epsilon_d: \qquad |\uparrow\rangle, |\downarrow\rangle.$$

This reveals the underlying implications of transforming to Nambu space. The formalism exploits the parity-conserving property of a BCS Hamiltonian by leaving out the odd parity part (single fermionic occupation), thereby reducing it to a single-particle problem with $|\uparrow\downarrow\rangle$ and $|0\rangle$ as the only possible states. From the many-body Hamiltonian we can combine two fermions of same spin with positive and negative energy relative to ϵ_d, resulting in the $|\uparrow\rangle$ and $|\downarrow\rangle$ solutions.

The ground state $|-\rangle$ is equivalent to the BCS singlet ground state $\prod_{\mathbf{k}}(u_{\mathbf{k}} - |v_{\mathbf{k}}|e^{i\phi}c_{\mathbf{k}\uparrow}^\dagger c_{-\mathbf{k}\downarrow}^\dagger)|\phi_0\rangle$. This becomes clear if we turn to a description of the energy spectrum in terms of quasiparticle

excitations. The ground state is a complicated state; a superposition of many-body states with different numbers of fermions, but it is the vacuum of the quasiparticle operators. These are defined as the pair of operators which diagonalize the Hamiltonian by a rotation in particle-hole space

$$\begin{pmatrix} \gamma_\uparrow \\ \gamma_\downarrow^\dagger \end{pmatrix} = \begin{pmatrix} u^* & v \\ -v^* & u \end{pmatrix} \begin{pmatrix} d_\uparrow \\ d_\downarrow^\dagger \end{pmatrix},$$

such that

$$\hat{H}_{\text{eff}} = \begin{pmatrix} d_\uparrow^\dagger & d_\downarrow \end{pmatrix} \begin{pmatrix} \epsilon_d & -\Gamma \sum_j e^{i\phi_j} \\ -\Gamma \sum_j e^{-i\phi_j} & -\epsilon_d \end{pmatrix} \begin{pmatrix} d_\uparrow \\ d_\downarrow^\dagger \end{pmatrix} = \begin{pmatrix} \gamma_\uparrow^\dagger & \gamma_\downarrow \end{pmatrix} \begin{pmatrix} \varepsilon & 0 \\ 0 & -\varepsilon \end{pmatrix} \begin{pmatrix} \gamma_\uparrow \\ \gamma_\downarrow^\dagger \end{pmatrix}.$$

From this equality, by inserting the transformation and using the normalization condition from $\{\gamma_\sigma, \gamma_{\sigma'}^\dagger\} = \delta_{\sigma\sigma'}$ that $|u|^2 + |v|^2 = 1$ we can derive the expressions for u and v, yielding

$$|u|^2 = \frac{1}{2}\left(1 + \frac{\epsilon_d}{\varepsilon}\right) \qquad |v|^2 = \frac{1}{2}\left(1 - \frac{\epsilon_d}{\varepsilon}\right).$$

$\hat{H}_{\text{eff}}$ has the pair of eigenstates

$$|+\rangle = v^* |0\rangle + u |\uparrow\downarrow\rangle = \gamma_\uparrow^\dagger \gamma_\downarrow^\dagger |-\rangle$$

$$|-\rangle = u^* |0\rangle - v |\uparrow\downarrow\rangle$$

where we can see the clear equivalence to the BCS ground state.

The γ_σ operators are fermionic quasiparticle operators such that the ground state $|-\rangle$ of the system can be defined as the state with no quasiparticle excitations $\gamma_\uparrow |-\rangle = \gamma_\downarrow |-\rangle = 0$ which can be verified by the equations above.

The quasiparticle operators are the ladder operators of the quantum dot. The ground state $|-\rangle$ is their vacuum, the single-particle eigenstates are $\gamma_\uparrow^\dagger |-\rangle = |\uparrow\rangle$ and $\gamma_\downarrow^\dagger |-\rangle = |\downarrow\rangle$, while the excited state is accessed by $\gamma_\uparrow^\dagger \gamma_\downarrow^\dagger |-\rangle = |+\rangle$.

Finally, to see how this is the same as the eigenstates found in (3.10), we identify $u = u^* = (\pm\varepsilon - \epsilon_d)$, $v = \Gamma \sum_j e^{i\phi_j}$ and realize that

$$\frac{(\epsilon_d \pm \varepsilon)(\epsilon_d \mp \varepsilon)}{-|\Gamma|^2} = 1 \quad \Longleftrightarrow \quad \frac{\epsilon_d \pm \varepsilon}{\Gamma \sum_j e^{i\phi_j}} = \frac{-\Gamma \sum_j e^{-i\phi_j}}{\epsilon_d \mp \varepsilon}$$

The eigenstates $|\pm\rangle$ are superpositions of particles and holes, just like expected for ABS. Starting out from a single energy level on the QD, the superconductors have been coupled in a way such that a two-level system has emerged on the quantum dot.

The energy spectrum is no different from what we could achieve already with a standard $n = 2$ Josephson junction. Thus, a natural question so far is why we would bother to include a larger number of superconductors. The new phenomena will show up during the rest of the thesis, as we start generalizing concepts like the Josephson current and conductance properties as anticipated in the introduction. Throughout the thesis, we assume $T = 0$ and the multiterminal Josephson junction being in its ground state $-\varepsilon$.

Finally, we should remember that we simplified the problem by making all the parameters of the superconductors and the tunneling equal. This will of course not be possible to do perfectly in practice, and everything will look more complicated if these vary.

3.3 Josephson Current

Even at zero voltage, a current can flow between two slightly separated superconductors. This was predicted by Josephson to depend on the phase difference $\Delta\phi$ of the superconductors via the relation $I = I_c \sin(\Delta\phi)$, which was introduced in Section 2.1. In this section, the Josephson current of the n-terminal Josephson junction of this chapter will be derived and analyzed with a focus on three terminals.

In terms of the free energy, the Josephson current is defined as $I = \frac{2e}{\hbar}\frac{\partial F}{\partial\phi}$ which at $T = 0$ can be expressed in terms of the ground state energy $-\varepsilon$

$$\langle 0|\left(\frac{\partial\hat{H}}{\partial\phi}\right)|0\rangle = \langle 0|\frac{\partial}{\partial\phi}\left(\hat{H}|0\rangle\right) - \langle 0|\hat{H}\frac{\partial}{\partial\phi}|0\rangle$$

$$= \langle 0|\frac{\partial}{\partial\phi}\left(-\varepsilon|0\rangle\right) + \varepsilon\langle 0|\frac{\partial}{\partial\phi}|0\rangle = -\frac{\partial\varepsilon}{\partial\phi}.$$

The Josephson current of the j'th lead is then

$$I_j = -\frac{2e}{\hbar}\frac{\partial\varepsilon}{\partial\phi_j} = -\frac{2e}{\hbar}\frac{\partial}{\partial\phi_j}\sqrt{\epsilon_d^2 + \Gamma^2\sum_{nm}\cos(\phi_n - \phi_m)} = \frac{-e\Gamma^2}{\varepsilon\hbar}\frac{\partial}{\partial\phi_j}\sum_{nm}\cos(\phi_n - \phi_m)$$

$$= \frac{2e\Gamma^2}{\varepsilon\hbar}\sum_{i\neq j}\sin(\phi_j - \phi_i).$$

Generally, ε depends on the phase variables through the equation (3.9). Only in the limit of $\epsilon_d/\Gamma \gg 1$, we recover the familiar sinusoidal dependence of the Josephson current. The extension to n leads makes sense since any superconductor coupling to the junction of phase different from ϕ_j contributes to generating the j'th Josephson current.

At a first glance the critical current, i.e. the maximal current that each lead is able to support, is $I_c = 2e(n-1)\Gamma^2/\varepsilon\hbar$, reached in the case where all phases but the j'th are equal while ϕ_j differs by $\pi/2 + n\pi$. However, all the currents can clearly not obey this condition at once, since the currents in all terminals are dependent due to the mutual phases together with current conservation $\sum_j I_j = 0$. For an n-terminal Josephson junction, the critical current can no longer be described by a scalar, but rather by a geometrical object, a critical current contour (CCC) in an $(n-1)$-dimensional space. Inside the CCC, all terminals are at a zero voltage, and supercurrent can flow between the leads. The supercurrent in each terminal depends on the $n-1$ independent phase differences in the junction.

When fixing the gauge to $\phi_n = 0$ for the n'th terminal and hence measuring all other phases relative to ϕ_n, current conservation is satisfied automatically.
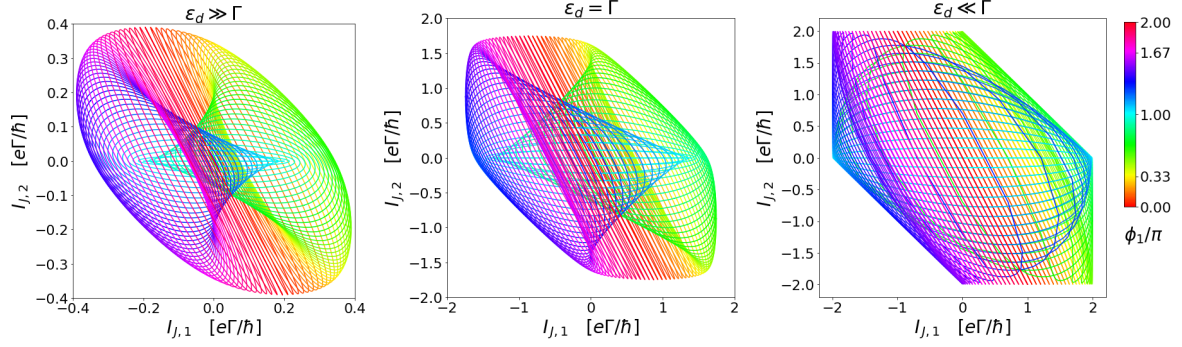
Figure 3.2: The CCC (the boundary of the coloured area) as a function of detuning, shown for $\epsilon_d/\Gamma = 10$, $\epsilon_d/\Gamma = 1$ and $\epsilon_d/\Gamma = 0.1$ from left to right. Note the smaller scale of the leftmost plot; the area of the zero-voltage state is highly suppressed for large detuning.

For a three-terminal Josephson junction with $\phi_3 = 0$, we have

$$I_{J,1} = I_{c,0}(\phi_1, \phi_2)\big(\sin(\phi_1 - \phi_2) + \sin(\phi_1)\big)$$
$$I_{J,2} = I_{c,0}(\phi_1, \phi_2)\big(-\sin(\phi_1 - \phi_2) + \sin(\phi_2)\big)$$

with
$$I_{c,0}(\phi_1, \phi_2) = \frac{2e\Gamma}{\hbar\,\sqrt{(\epsilon_d/\Gamma)^2 + 3 + 2(\cos(\phi_1 - \phi_2) + \cos(\phi_1) + \cos(\phi_2))}} \qquad (3.11)$$

The subscript J was added to the Josephson currents to specify their meaning and distinguish them from the bias currents of later sections.

This function is plotted in $(I_{J,1}, I_{J,2})$-space in Figure 3.2 for three different regimes of detuning ϵ_d/Γ. This plot maps ϕ_1 to a cyclic color map, as shown in the figure. Sweeping ϕ_2 for a constant ϕ_1-value forms an ellipse in $(I_{J,1}, I_{J,2})$-space. This is done to visualize how the phase values relate to a position inside the CCC. For example, if $\phi_1 = 0$, the Josephson currents are linearly related along the red line, and if $\phi_1 = \pi$, the supercurrents are well embedded inside the CCC with only $I_{J,1}$ varying as a function of ϕ_2.

First of all, the figure shows the area and shape of the CCC as a function of detuning, which for $n = 3$ can conveniently be visualized in the plane. For $\epsilon_d/\Gamma \gg 1$ the CCC is elliptical. Despite the superconductors being separated, only coupled through the single energy level on the dot, the supercurrents are highly dependent; the slightest variation in the current over one terminal affects the allowed values in the others. In this limit, the supercurrent amplitude is reduced significantly with respect to the resonant case, and it can roughly be approximated by a constant. For an increasingly large detuning, the QD is eventually decoupled from the superconductors, and the supercurrrent vanish. In the limit of $\epsilon_d/\Gamma \to 0$, the QD's energy level approaches resonance with the Cooper pairs' energy in the superconductors, and the current is stronger. The CCC is hexagonal in this limit. The maximal possible current over Terminal 2 is not affected by $I_{J,1}$ varying between 0 and its maximal possible value of $2\,e\Gamma\hbar^{-1}$. As opposed to the detuned case, the current over one terminal can vary in the entire range from -2 to $2\,e\Gamma\hbar^{-1}$ when no current

runs through the other terminal, resulting in vertices in the CCC at these extrema.

Another huge difference is the behaviour for phase values around π. The star shape appearing in the figure for $\epsilon_d/\Gamma \gg 1$ consists of the Josephson currents at $\epsilon_d \gg \Gamma$ with phase values restricted to $\phi_1 \in [\pi/2; \pi]$ and $\phi_2 \in [\pi; 3\pi/2]$ together with $\phi_2 \in [\pi/2; \pi]$ and $\phi_1 \in [\pi; 3\pi/2]$, which is the same object mirrored around the $I_1 = I_2$ axis. For these phase ranges in the detuned case, the supercurrents are confined to low values, creating the mesmerizing star shape, while this region is characterized by wildly varying currents when approaching resonance.

Just like in the 1D case of the RCSJ model, the Josephson currents equals the bias currents inside the CCC after the convergence time, after which the fictitious particle has settled in the new potential minimum. The 2D case will be introduced properly in Section 5.1. One can view Figure 3.2 as maps of how fast the potential minimum changes position in (ϕ_1, ϕ_2) as a function of bias currents, since this is proportional to the density of the coloured lines. For large detuning, the potential changes fastest for small bias currents. On the contrary, for $\epsilon_d/\Gamma \ll 1$, the line density is higher at the right and left edges, so the potential minimum changes fastest right before exiting the supercurrent regime. The figure is also a representation of the distribution of the current values when both phases are winding and the Josephson currents are alternating, forming exactly the same figures as in Figure 3.2 after completing a full cycle. At large detuning, the currents over the Josephson junctions are thus seen to spend most time at low values, at resonance the currents spend more time at maximal amplitudes while at ϵ_d/Γ the distribution is approximately flat.

As noted earlier in relation to the ABS energies of Figure 3.1, the phase factor $\sum_{ij} \cos(\phi_i - \phi_j)$ of the denominator in the case of three terminals can vary from a minimum of 0 at $(\phi_1, \phi_2) = (2\pi/3, 4\pi/3)$ or vice versa, to maximum of 9 when all three phases are equal at $(\phi_1, \phi_2) = (0, 0)$. At exact resonance $\epsilon_d = 0$, the Josephson current is therefore divergent. For this reason, the minimal detuning used throughout the thesis is $\epsilon_d/\Gamma = 0.1$.

4 Foundations of a Superconducting Qubit with a three-terminal Josephson Junction

Now that the fundamental properties of an n-terminal Josephson junction have been extracted in Chapter 3, we propose a way to integrate it in a superconducting circuit. As we have seen in Section 2.3, two-terminal Josephson junctions are essential elements in superconducting qubits, so it is a relevant question to explore the addition of terminals to the junction.

This section will be concentrated on a three-terminal Josephson junction. Keeping it in its ground state, it contributes with energy

$$-\varepsilon_{n=3} = -\Gamma\sqrt{(\epsilon_d/\Gamma)^2 + 3 + 2\big(\cos(\phi) + \cos(\theta) + \cos(\phi - \theta)\big)}$$

to the circuit potential energy, as stated in (3.9).

Inspired from the flux qubit and its successors, we connect two of the three wires of a three-terminal Josephson junction and add a two-terminal Josephson junction to the resulting loop, which accommodates a flux. The single terminal not connected to the loop is grounded, and its phase is set to zero. The two other terminals are capacitively shunted to ground. This superconducting circuit is shown in Figure 4.1.
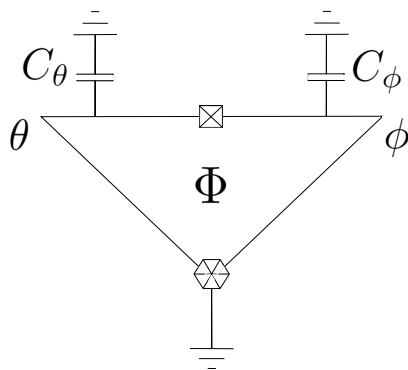

Figure 4.1: A three-terminal Josephson junction (hexagon) with two of the terminals connected over a two-terminal Josephson junction (square), forming a loop.

The potential as a function of the two independent phases is

$$U(\phi, \theta) = -E_{J,2}\cos(\phi - \theta + \phi_{ext}) - \Gamma\sqrt{(\epsilon_d/\Gamma)^2 + 3 + 2\big(\cos(\phi) + \cos(\theta) + \cos(\phi - \theta)\big)},$$

where $E_{J,2}$ denotes the Josephson energy of the two-terminal junction, and $\phi_{ext} = 2\pi\Phi/\Phi_0$.

The periodic potential $U(\phi, \theta)$ has one large minimum at $(\phi, \theta) = (0, 0)$ when no flux is present. At exactly $\Phi = \Phi_0/2$, there are two symmetric minima at $(\phi, \theta) = (\pi/3, 5\pi/3)$ and $(\phi, \theta) = (5\pi/3, \pi/3)$, respectively, as seen in Figure 4.2. Here it is also illustrated that tuning Φ away from exactly half a flux quantum shifts the relative depth of the wells. The two wells only exist
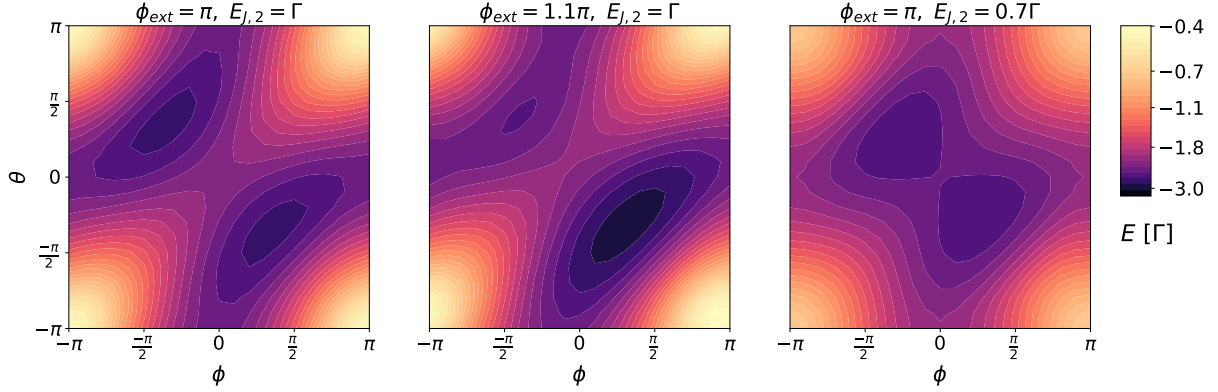
Figure 4.2: The potential $U(\phi, \theta)$ for $\epsilon_d/\Gamma = 1$ shown for three different settings of the tunable parameters.

in a range of approximately 10% from that value, showing that the potential is highly sensitive to flux.

Shifting the ratio between the energy scales of the two- and three-terminal junctions away from balance, $E_{J,2}/\Gamma = 1$, lowers the barrier height between the wells in one direction and raises it in the other direction.

Regardless of $E_{J,2}/\Gamma$, there is a reflection symmetry over the $\theta = \phi$ axis of the potential. Hence, the optimal potential parameters from considering the shape of the potential only, are found to be $\Gamma = E_{J,2}$ and $\Phi = \Phi_0/2$.

To make sure the choices of energy parameters in the following are experimentally realistic, we consider the value $E_J = 10\,h\,\text{GHz} \approx 41\,\mu\text{eV}$ from Ref. [31]. Setting $E_{J,2}$ at this value, we compare it to Γ, which according to the derivation in Chapter 3 must be well below the superconducting energy gap $\Gamma \ll \Delta$. For aluminium, we have approximately $\Delta = 200\,\mu\text{eV}$. Setting $E_{J,2} = \Gamma$ therefore results in $\Gamma/\Delta \approx 0.02$, which is reasonable within the approximation.

4.1 Finding the Optimal Qubit States

Now that we have the desired double-well potential settled, we proceed to the full Hamiltonian for the circuit, which is

$$\hat{H} = 4E_{C,\phi}(\hat{n}_\phi - n_{g,\phi})^2 + 4E_{C,\theta}(\hat{n}_\theta - n_{g,\theta})^2 + U(\phi, \theta).$$

Here, $E_{C,\phi} = e^2/2C_\phi$ is the charging energy associated with phase ϕ and $n_{g,\phi}$ the offset charge on the C_ϕ capacitor.

The capacitors contribute with the kinetic terms of the Hamiltonian with capacitance C acting as mass and charge $2e\hat{n}$ acting as the momentum operator. From the commutation relation between the phase and charge operators, we have that $\hat{n}_\phi = -i\partial_\phi$ in the phase representation.

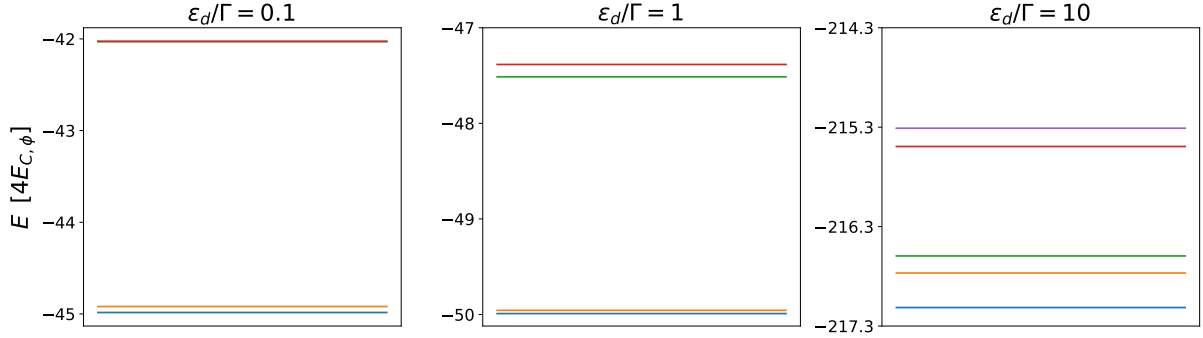To solve this numerically, the discrete and dimensionless two-dimensional Schrödinger equation

Figure 4.3: The energy spectrum for the first four or five eigenstates as a function of detuning. The system shows nearly degenerate ground- and first excited states with a very large anharmonicity for low detuning $\epsilon_d/\Gamma \lesssim 1$.
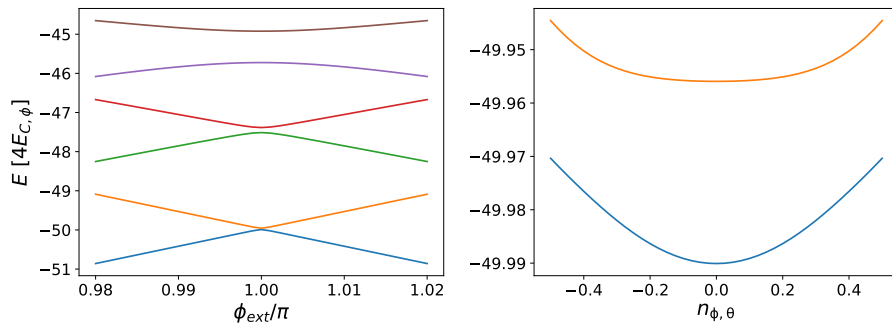

Figure 4.4: Dispersion of the lowest lying energy eigenstates as a function of flux (left) and offset charge (right). The detuning $\epsilon_d/\Gamma = 1$.

for this Hamiltonian is set up. Here, the differential quotient is associated with the matrix that performs the following operation on all n values of the ψ-vector,

$$\partial_\phi \psi_n \to \frac{\psi_{n+1} - \psi_{n-1}}{2\Delta\phi},$$

where $\Delta\phi$ is the distance between two ϕ-values. The choice of taking the difference between ψ_{n+1} and ψ_{n-1} when computing the derivative of ψ_n ensures symmetric matrices and a hermitian Hamiltonian.

The Schrödinger equation is then solved by diagonalizing the Hamiltonian matrix to find the resulting eigenvalues and eigenstates.

The capacitors are supposed to be large enough to ensure the system is in its heavy regime, such that we get a qubit protected from relaxation. We set $E_{J,2}/E_{C,\phi} = 80$ and $E_{C,\phi} = E_{C,\theta}$.

For low detuning, the energy spectrum for the first few eigenstates consists of pairs of quasi-degenerate states, as seen in Figure 4.3. In the low detuning regime, the anharmonicity is high such that the transition frequency between the first and second excited state is much larger than between the lowest two states, $\omega_{1\to2} \gg \omega_{0\to1}$. These features are desirable for a qubit, since we can use the two lowest eigenstates and protect the qubit from dephasing and avoid interactions
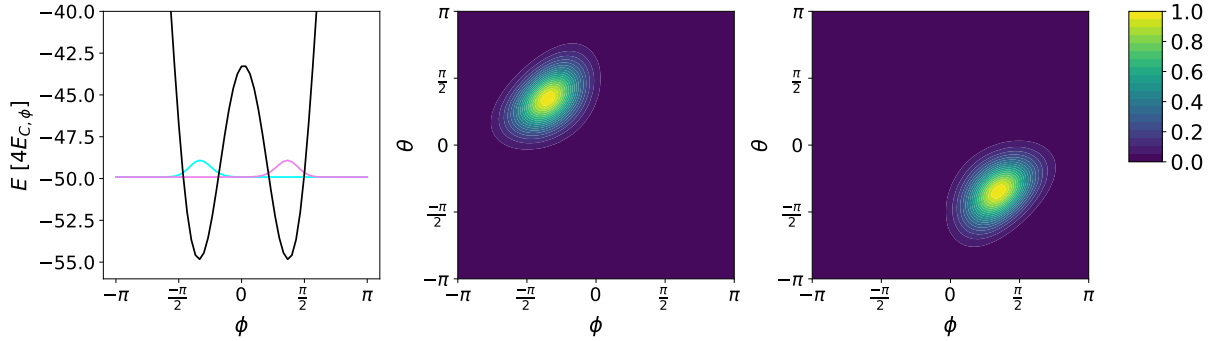
Figure 4.5: The two superposition states $\langle L|L\rangle$ (middle) and $\langle R|R\rangle$ (right) at $\phi_{ext} = \pi$, $E_{J,2} = \Gamma$ and $\epsilon_d/\Gamma = 1$. Left: Potential (black) and qubit states $\langle L|L\rangle$ (cyan), $\langle R|R\rangle$ (violet) for the cross section $\theta = -\phi$ for $\phi \in [-\pi, \pi]$. The normalized wavefunctions have in this plot been rescaled to a height of 1 and set at the energy $(E_0 + E_1)/2$.

with higher-lying states. The energy scale of the three plots is the same to show how the states are squeezed into the potential wells as a function of detuning. Based on this, we set the detuning to $\epsilon_d/\Gamma = 1$.

Now we consider the dispersion of the energy eigenstates. The dispersion of the lowest six (two) eigenstates as a function of flux (offset charge) is shown in Figure 4.4. As a function of flux, we see again that the energies are paired with the splitting between each pair increasing dramatically away from $\Phi = \Phi_0/2$. The transition energy between the ground- and first excited states increases by an order of magnitude when the flux changes from $\phi_{ext} = 1.000\,\pi$ to $\phi_{ext} = 0.996\,\pi$. The transition energy E_{01} has a *sweet spot* at $\phi_{ext} = \pi$, meaning $\partial E_{01}/\partial\phi_{ext} = 0$ at this flux bias. The same applies to the offset charges n_ϕ and n_θ, with a sweet spot at $n_{\phi,\theta} = 0$. However, in comparison, the dispersion with respect to these parameters is flat, noting the energy scales. On this basis, we set the parameters at $n_{g_\phi} = n_{g_\theta} = 0$ and $\phi_{ext} = \pi$.

Now recall the potential, which we also showed to be very sensitive to flux, see Figure 4.2. When setting exactly $\phi_{ext} = \pi$, the symmetry of the potential landscape means that the two lowest-lying eigenstates of the system $|0\rangle$ and $|1\rangle$ (in blue and orange in figures 4.3 and 4.4) are symmetric and anti-symmetric solutions over the two minima. We construct our qubit states from the superpositions of these two eigenstates, which, thanks to the large capacitors, are localized in the left and right minimum, respectively:

$$|L\rangle = (|0\rangle + |1\rangle)/\sqrt{2}$$

$$|R\rangle = (|0\rangle - |1\rangle)/\sqrt{2}$$

These states are degenerate with energy $\langle E\rangle = (E_0 + E_1)/2$, where E_0 and E_1 are the eigenenergies of the $|0\rangle$ and $|1\rangle$ states, respectively. The superposition states are shown in Figure 4.5. It is clear that they are confined to their respective potential wells. A diagonal cross section is shown in the figure with the potential background, showing an undoubtedly vanishing overlap between the states. This points towards that there is space to relax the ratio E_J/E_C.

With the considerations done in this subsection, we have arrived at a protected qubit. It is anharmonic and the qubit states are degenerate and disjoint.

4.2   Perspective: Variable Protection Approach for Gates

In this subsection, we will show the similarity of the qubit of the previous subsection to the Double Shunted Flux Qubit (DSFQ) of Reference [31] and sketch a sensible way of continuing the analysis of the prospects of this qubit.

We will briefly examine the potential in the limit of large detuning. Performing a Taylor expansion around the limit $\Gamma \ll \epsilon_d$ to second order yields

$$\varepsilon \approx \epsilon_d + \frac{\Gamma^2}{2\epsilon_d} \sum_{ij} \cos(\phi_i - \phi_j).$$

In the weakly coupled limit, the potential of the qubit with a 3-terminal junction is

$$U_{\text{weak}}(\phi, \theta) = -E_{J2} \cos(\phi - \theta + \phi_{ext}) - \frac{\Gamma^2}{\epsilon_d}\big(3/2 + \cos(\phi - \theta) + \cos(\phi) + \cos(\theta)\big).$$

In this limit, the potential can be decomposed into separate two-terminal junctions with sinusoidal phase dependence. When the flux is biased at $\phi_{ext} = \pi$, we have to zeroth order

$$U_{\text{weak},\phi_{ext}=\pi}(\phi, \theta) = -E_{J,3}\big(\cos(\phi) + \cos(\theta)\big) + \big(E_{J,2} - E_{J,3}\big)\cos(\phi - \theta).$$

For $E_{J,2} = (1 + \alpha)E_{J,3}$, this is equal to the DSFQ which has the potential

$$U_{DSFQ} = -E_J\big(\cos(\phi) + \cos(\theta)\big) - \alpha E_J \cos(\phi - \theta + \phi_{ext}).$$

The effect of two Josephson junctions of a flux-type qubit can be realized locally at a three-terminal Josephson junction when the flux bias is set exactly at the flux quantum and when $\epsilon_d/\Gamma \gg 1$. This also suggests that the approach of the DSFQ to gates, presented in Section 2.3.3, is applicable to the qubit discussed in Section 4.1.
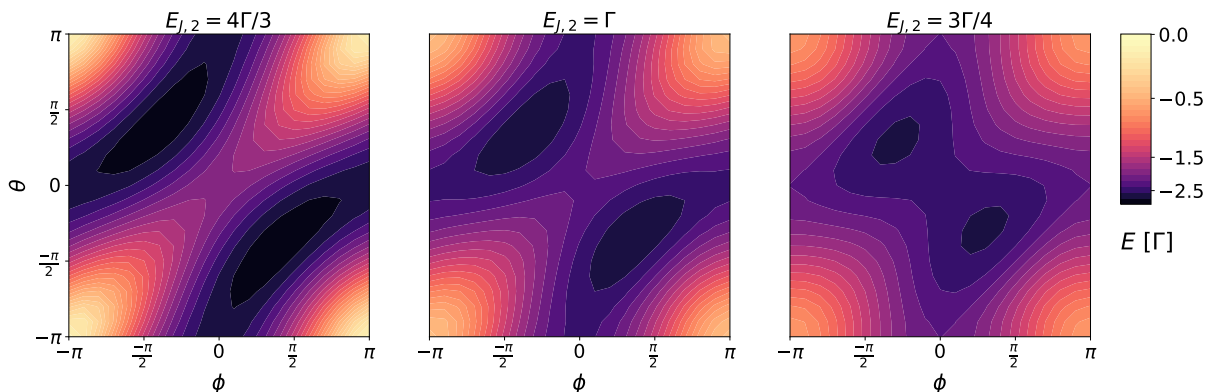

Figure 4.6: The potential for $\epsilon_d/\Gamma = 1$ and $\phi_{ext} = \pi$ at three different values of $E_{J,2}/\Gamma$, demonstrating a tunable barrier height.
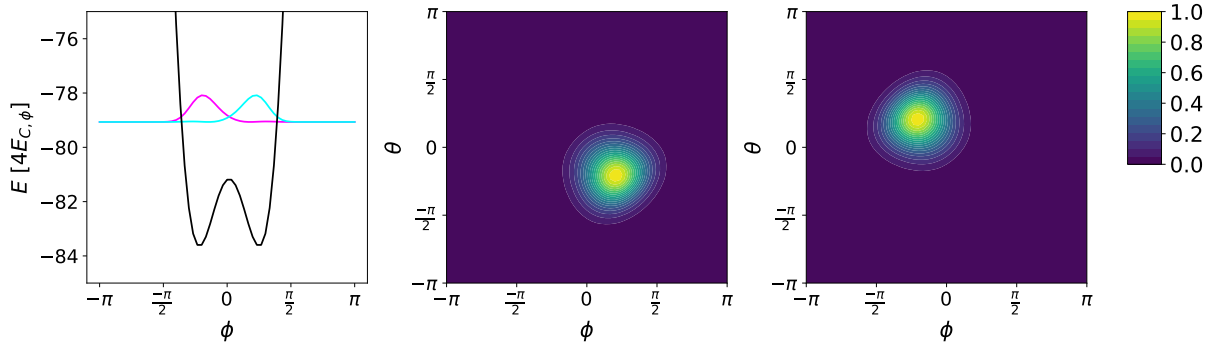
Figure 4.7: The two superposition states $\langle L|L \rangle$ (middle) and $\langle R|R \rangle$ (right) at $\phi_{ext} = \pi$ and $E_{J,2} = 0.625\,\Gamma$. See figure text of Figure 4.5 for comments on leftmost plot.
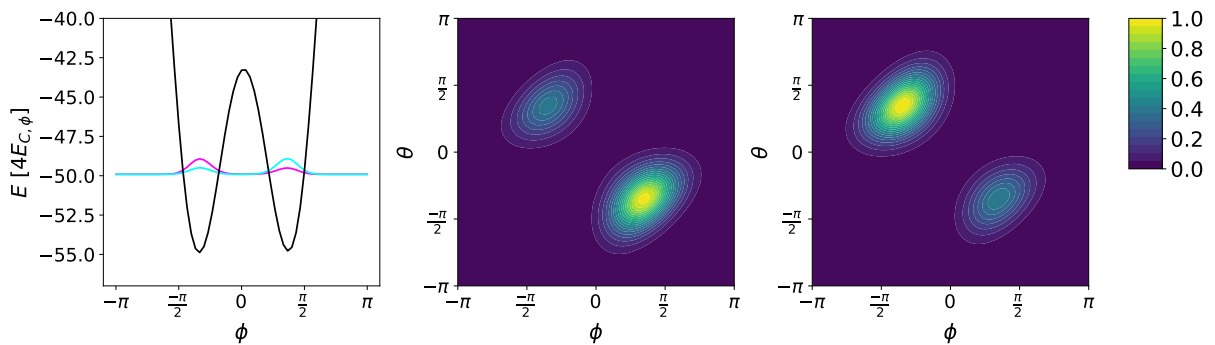

Figure 4.8: The two superposition states $\langle L|L \rangle$ (middle) and $\langle R|R \rangle$ (right) at $\phi_{ext} = 1.001\pi$ and $E_{J,2} = \Gamma$. See figure text of Figure 4.5 for comments on leftmost plot.

We now continue with the two protected qubit states $|L\rangle$ and $|R\rangle$ found in Section 4.1, centered around $(\phi, \theta) = (\pi/3, 5\pi/3)$ and $(5\pi/3, \pi/3)$, respectively, both with energy E. In order to be able to utilize the qubit, it is essential to have an efficient way to perform gates between the qubit states.

Two common gate methods were briefly discussed in Section 2.3. For this qubit, it would be relevant to investigate the method of a tunable barrier as proposed in Reference [31], since we have seen that the qubits are closely related, and that the barrier between the potential wells can be lowered by varying the $E_{J,2}/\Gamma$ ratio as shown for three values in Figure 4.6. When lowering the ratio, the barrier at $\phi = \theta = 0$ is lowered, merging two neighboring wells. When the ratio is increased, the two barriers at $(\phi, \theta) = (0, \pi)$ and vice versa are lowered simultaneously, merging the well with the neighboring wells of two other unit cells. In Figure 4.7 it is evident how the overlap increases between the two states when tuning $E_{J,2}/\Gamma$ away from 1, correspondingly to tuning α of the DSFQ away from 1.

In Figure 4.8, it is shown how the $|L\rangle$ and $|R\rangle$ states vary when tuning the flux just 1‰ away from $\Phi_0/2$. Then the $|L\rangle$ state has a small amplitude in the R well and vice versa. This could be an alternative way of tuning the parameters to a short-term mixing of the states. An advantage of tuning the flux to break the qubit protection is that the flux generally is easier to control

experimentally. However, if such a precise control is necessary, the advantage might cancel out.

Qualitatively, the DSFQ potential reacts equally to variations in α, regardless of ϵ_d/Γ. However, details of the discrepancies between the two qubits are unclear and it would require an independent examination. This section has shown that the variable protection method could be a good candidate for realizing gates for this qubit.

5 Critical Current Contours and Differential Resistance

Until this point, we have only studied multiterminal Josephson junctions under zero voltage. In this regime, DC Josephson currents can flow over the junction as a function of phase differences. However, the junction can only support currents of limited strength, corresponding to the critical current of two-terminal junction. If sufficiently large bias currents are applied, dissipation builds into the system, the phase starts winding, the Josephson current alternates and finite voltages arise between the leads. This regime can for two-terminal Josephson junctions be modelled with the RCSJ model in which the junction is shunted by a resistor and a capacitor, as described in detail in Section 2.1.

In Section 5.1, the RCSJ model is generalized to the three terminals, the details of the numerical solution are given and the resulting dynamics are compared to those of the 1D case. The rest of the chapter will be concerned with the conductance properties of the three-terminal Josephson junction as a function of bias currents, applied magnetic flux, the Q factor and detuning of the QD.

5.1 RCSJ Model for the Three-terminal Josephson Junction

The extension of the RCSJ model to a three-terminal Josephson junction is done by forming a circuit loop of three Josephson junctions as seen in Figure 5.1. The three Josephson junctions have equal critical currents $I_{c,0}$ and are shunted by equal resistances R_0 and capacitances C_0. The third terminal is grounded.
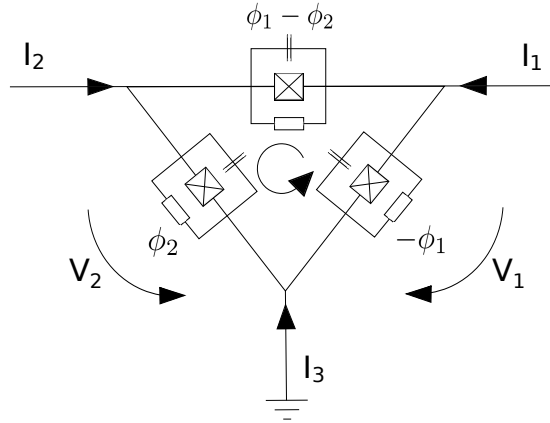

Figure 5.1: Three-terminal RCSJ model. All resistors have resistance R_0 and all capacitors have capacitance C_0. The arrows point in the direction of positive current. Note that V_1 and V_2 denote the voltage drops over the right and left paths to ground, respectively, and should not be confused with the location of I_1 and I_2.

The phases are given relative to ϕ_3, corresponding to a constant $\phi_3 = 0$, and the current I_3 can be found from current conservation. This allows us to reduce the problem to two dimensions in

both the phases and the bias currents.

First, we restate the Josephson currents from equations (3.11) for convenience,

$$I_{J,1} = I_{c,0}(\phi_1, \phi_2)\big(\sin(\phi_1 - \phi_2) + \sin(\phi_1)\big)$$

$$I_{J,2} = I_{c,0}(\phi_1, \phi_2)\big(-\sin(\phi_1 - \phi_2) + \sin(\phi_2)\big)$$

$$\text{with} \qquad I_{c,0}(\phi_1, \phi_2) = \frac{2e\Gamma}{\hbar\,\sqrt{(\epsilon_d/\Gamma)^2 + 3 + 2(\cos(\phi_1 - \phi_2) + \cos(\phi_1) + \cos(\phi_2))}}.$$

Applying Kirchoff's First Law to the circuit of Figure 5.1 and using the Josephson relation $V_i = \hbar\dot{\phi}_i/2e$ yields the two coupled second-order differential equations

$$I_1 = I_{c,0}\sin(\phi_1 - \phi_2) + I_{c,0}\sin(\phi_1) + \frac{\hbar}{2eR_0}\big(2\dot{\phi}_1 - \dot{\phi}_2\big) + \frac{\hbar C_0}{2e}\big(2\ddot{\phi}_1 - \ddot{\phi}_2\big)$$

$$I_2 = I_{c,0}\sin(\phi_2 - \phi_1) + I_{c,0}\sin(\phi_2) + \frac{\hbar}{2eR_0}\big(2\dot{\phi}_2 - \dot{\phi}_1\big) + \frac{\hbar C_0}{2e}\big(2\ddot{\phi}_2 - \ddot{\phi}_1\big).$$

By introducing the characteristic time $t_0 = \frac{\hbar}{e\Gamma}\frac{3\hbar}{2eR_0}$ and switching to dimensionless time $\tilde{t} = t/t_0$ and dimensionless current $\tilde{I} = \frac{\hbar}{e\Gamma}I$, we obtain the equation in dimensionless form

$$\begin{pmatrix} \dot{\phi}_1(\tilde{t}) \\ \dot{\phi}_2(\tilde{t}) \end{pmatrix} + \frac{R_0 C_0}{t_0}\begin{pmatrix} \ddot{\phi}_1(\tilde{t}) \\ \ddot{\phi}_2(\tilde{t}) \end{pmatrix} = \begin{pmatrix} 2 & 1 \\ 1 & 2 \end{pmatrix}\begin{pmatrix} \tilde{I}_1 - \tilde{I}_{J1}(\phi_1(\tilde{t}), \phi_2(\tilde{t})) \\ \tilde{I}_2 - \tilde{I}_{J2}(\phi_1(\tilde{t}), \phi_2(\tilde{t})) \end{pmatrix}. \tag{5.1}$$

The parameter $R_0 C_0/t_0$ scales like $R_0^2 C_0$ i.e. like Q^2. Note that the notion of Q cannot exactly be copied from the 1D case, where we defined $Q = R\sqrt{2eI_cC/\hbar}$, since the critical current now is not a constant. The important feature is that $Q \propto R_0^2 C_0$, so Q in this section will refer to $Q = \sqrt{R_0 C_0/t_0} = R_0\sqrt{\frac{2eC_0}{\hbar}\frac{e\Gamma}{3\hbar}}$, but we note that the value of this constant may shift relative to the value of Q for a problem with a constant $I_{c,0}$.

The dimensionless tilted washboard potential in units of $\Gamma/2$ is

$$\tilde{U}(\phi_1, \phi_2) = -2\sqrt{(\epsilon_d/\Gamma)^2 + 3 + 2\big(\cos(\phi_1) + \cos(\phi_2) + \cos(\phi_1 - \phi_2)\big)} - \tilde{I}_1\phi_1 - \tilde{I}_2\phi_2$$

such that the equation of motion is

$$\frac{R_0 C_0}{t_0}\begin{pmatrix} \ddot{\phi}_1(\tilde{t}) \\ \ddot{\phi}_2(\tilde{t}) \end{pmatrix} = \begin{pmatrix} 2 & 1 \\ 1 & 2 \end{pmatrix}\begin{pmatrix} -\partial\tilde{U}/\partial\phi_1 \\ -\partial\tilde{U}/\partial\phi_2 \end{pmatrix} - \begin{pmatrix} \dot{\phi}_1(\tilde{t}) \\ \dot{\phi}_2(\tilde{t}) \end{pmatrix},$$

analogously to the 1D washboard. A unit cell of the potential under three different biases is shown in Figure 5.2.

The equations are solved numerically using the fourth-order Runge-Kutta method built in Python's *scipy.integrate.solve_ivp* function. This function solves first-order differential equations, so in order to use it, the set of two second-order differential equations is converted to a set of four first-order differential equations by introducing the vector

$$S(\tilde{t}) = \begin{pmatrix} \phi_1(\tilde{t}) \\ \phi_2(\tilde{t}) \\ \frac{R_0 C_0}{t_0}\dot{\phi}_1(\tilde{t}) \\ \frac{R_0 C_0}{t_0}\dot{\phi}_2(\tilde{t}) \end{pmatrix}$$
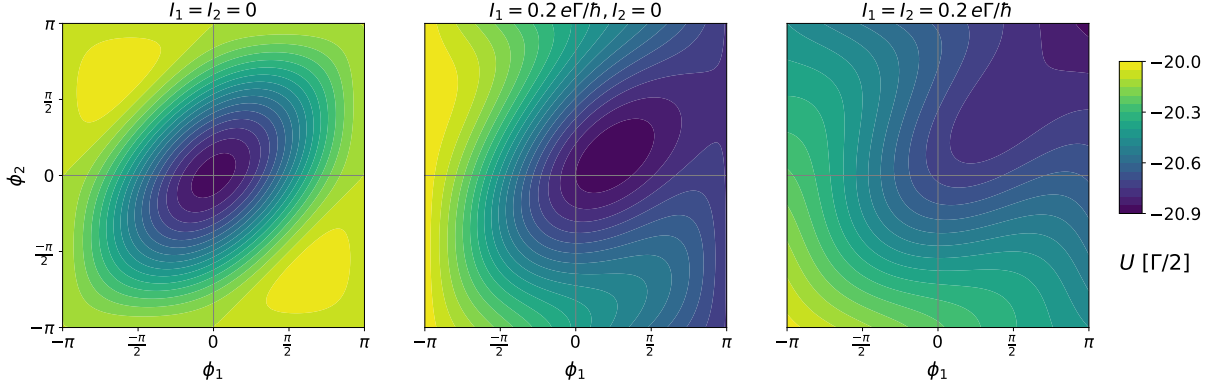
38

Figure 5.2: One unit cell of the 2D tilted washboard potential $U(\phi_1, \phi_2)$ for $\epsilon_d/\Gamma = 10$. When there are no bias currents, the minimum is located at $(\phi_1, \phi_2) = (0, 0)$. The minimum shifts in phase space as a function of bias currents. In the middle plot, I_1 in seen to tilt the washboard in both directions due to the coupled differential equations. The right subplot shows the potential at a point on the CCC.

such that (5.1) is a first-order equation for S

$$\frac{d}{d\tilde{t}}S(\tilde{t}) = \frac{t_0}{R_0 C_0} \begin{pmatrix} 0 & 0 & 1 & 0 \\ 0 & 0 & 0 & 1 \\ 0 & 0 & -1 & 0 \\ 0 & 0 & 0 & -1 \end{pmatrix} S(\tilde{t}) + \begin{pmatrix} 0 & 0 & 0 & 0 \\ 0 & 0 & 0 & 0 \\ 2 & 1 & 0 & 0 \\ 1 & 2 & 0 & 0 \end{pmatrix} \begin{pmatrix} \tilde{I}_1 - \tilde{I}_{J1}(\phi_1(\tilde{t}), \phi_2(\tilde{t})) \\ \tilde{I}_2 - \tilde{I}_{J2}(\phi_1(\tilde{t}), \phi_2(\tilde{t})) \\ 0 \\ 0 \end{pmatrix}.$$

The integration time step is set to $dt = 0.02\, t_0$ for the integral to reach the continuous limit. When calculating the voltage, the integration range is $t \in [0; 2000]\, t_0$ and the voltage is found by averaging over $\phi(t)$ from $t = 70\, t_0$ to $t = 2000\, t_0$. These values are chosen to account for the convergence time of the voltage and the long period of the $\dot{\phi}$ oscillations for some parameter values, while limiting the integration time.

The run time is around 1-2 seconds for one value of (I_1, I_2). Depending on the pixel size (the resolution of I_1 and I_2), it takes around 3 hours on a laptop to generate a plot of the voltages like the one shown in Figure 5.5. This is a major obstacle when looking for the dependence of the voltages or differential resistance on varying parameters. Therefore, in some situations the integration will be more coarse grained, which will be written explicitly in the figure text.

Inside the CCC, the initial conditions for the integration are set to be at rest in the minimum of the potential found using *scipy.optimize.fmin*. Outside CCC, the initial condition is simply set to $\{\phi_1, \phi_2, \dot{\phi}_1, \dot{\phi}_2\} = \{0,0,0,0\}$. For $Q < 1$, the only effect of varying the initial conditions outside CCC is the distribution of convergence time over the parameter space while for $Q \geq 1$ the result is sensitive to the initial conditions close to the CCC. This effect of Q on the dynamics is carried over from the discussion in Section 2.1.

Where nothing else is mentioned, the resistance and capacitance are set to $R_0 = 100\,\Omega$ and $C_0 = 60\,\text{fF}$ such that $Q = 0.78$, because the integration time is limited by setting $R_0 C_0 \approx t_0$ and

the convergence time is lower for $Q < 1$. The currents are measured in units of $e\Gamma/\hbar$ which is set to $1\,\mu A$, meaning Γ has the value $\Gamma = 4.1$ meV. This choice is arbitrary, only affecting the run time of the simulations, and does not affect the results other than setting the scale of the current axes, which should rather be read as depending on the more general $e\Gamma/\hbar$.

The generalization to two dimensions is non-trivial, since the two equations are coupled and cannot be described by a set of 1D washboards. In the limit of large detuning $\epsilon_d \gg \Gamma$, the multiterminal Josephson junction can be described by three individual Josephson junctions, but each 1D potential depends on both bias currents. If we for example start from zero bias currents and tilt the washboard along the ϕ_2-axis, the junctions remain under zero voltage after passing the value of $I_{c,0}$ since the current can distribute itself over three separate terminals. The generalized critical current is a contour in the 2D-plane as three examples showed in Section 3.3.

Note that this also means that the two-terminal Josephson junctions of the RCSJ model described in this section have a non-local dependence on all phase differences through the amplitude $I_{c,0}$. Hence, the model is only an approximation for the three-terminal Josephson junction, serving to include the resistive behaviour. Approaching the limit $\epsilon_d/\Gamma \gg 1$ where $I_{c,0}$ becomes phase-independent, the RCSJ model can be physically realized.
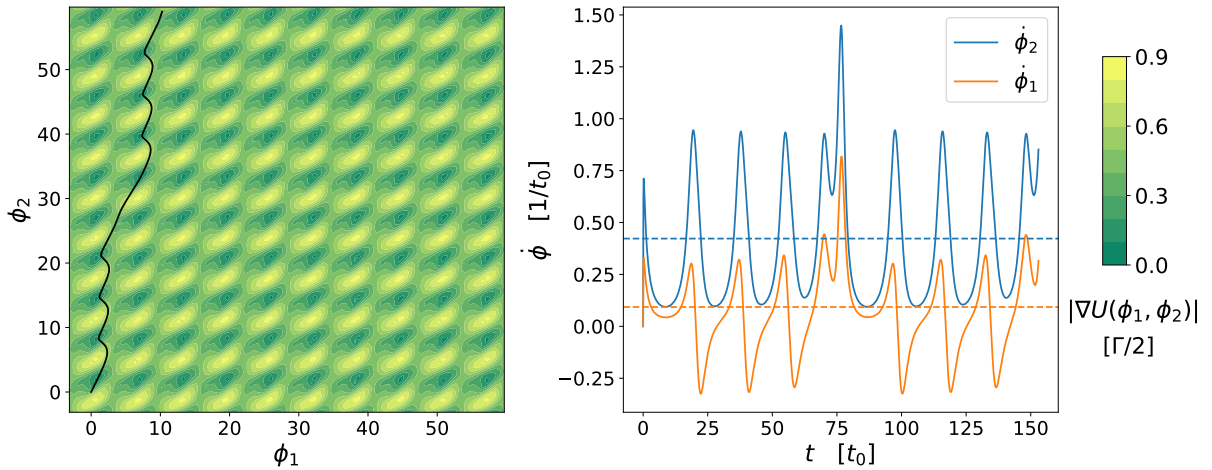

Figure 5.3: Particle trajectory plotted on the background showing the gradient magnitude of the potential $|\nabla U(\phi_1, \phi_2)|$. Dotted lines show $\langle \dot\phi \rangle$ for the function of same color after the convergence time. At low $Q = 0.25$ and a I_1 slightly outside the critical current, we observe phase slips in ϕ_1 and sharp voltage peaks in V_1. Here $I_2 = 0.4\,e\Gamma\hbar^{-1}$ and $I_1 = -0.019\,e\Gamma\hbar^{-1}$. $V_1 = 0.031$ and $V_2 = 0.141\,R_0 e\Gamma\hbar^{-1}$.

The solution of (5.1) is shown for two different sets of bias and Q values in figures 5.3 and 5.4. In figures 5.3 and 5.4 it is evident that the characteristics of the 1D washboard model dynamics, as was seen in figures 2.2 and 2.3, are preserved. For low Q and I_1 slightly exceeding $I_{c,0}$, the particle periodically slips to the next unit cell in ϕ_1, and the voltage is characterized by a series of pulses. It is remarkable how the voltage actually becomes higher at the peaks than in the high Q case, even though the particle spends more time in the flatter regions and the voltage
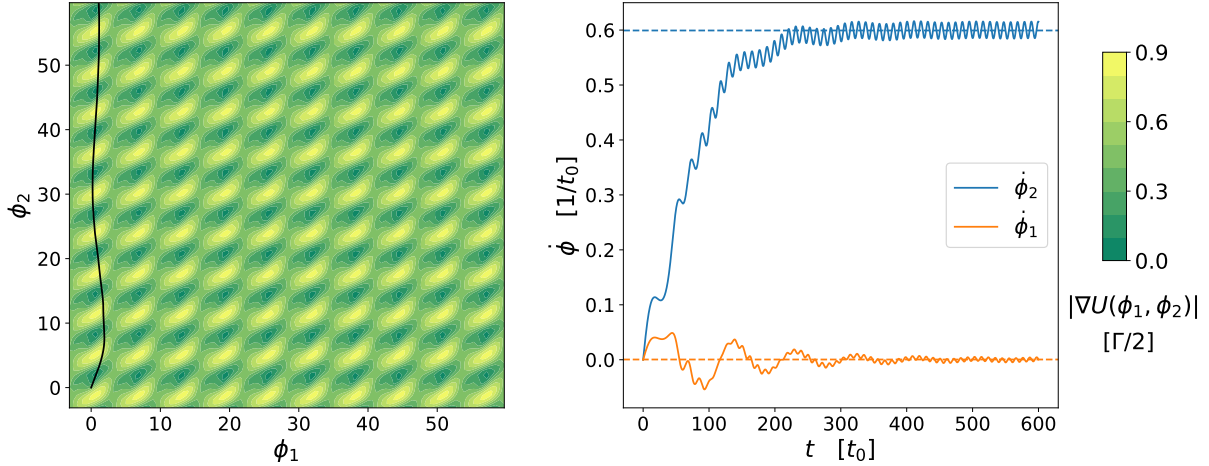
40

Figure 5.4: Particle trajectory plotted on the background showing the gradient magnitude of the potential $|\nabla U(\phi_1, \phi_2)|$. Dotted lines show $\langle \dot{\phi} \rangle$ for the function of same color after the convergence time. At high $Q = 7.8$ and a set of bias current inside the $I_1 = I_3$ branch, we see the large convergence time due to the large inertia. Here $I_2 = 0.4\,e\Gamma\hbar^{-1}$ and $I_1 = -0.025\,e\Gamma\hbar^{-1}$. $V_1 = 0$ and $V_2 = 0.200\,R_0 e\Gamma\hbar^{-1}$.

averages to a lower value.

For high Q, the convergence time is long as the particle on the underdamped washboard gains speed slowly, after which the voltages settle at nearly constant values. The resulting voltage is higher in the high Q case, as one would expect the heavier particle to have a higher terminal velocity.

We have now derived a proper model for the resistive regime of a three-terminal Josephson junction and have set up the numerical solution.

5.2 Differential Resistance in Zero Magnetic Field

In this section, the differential resistance of a current biased three-terminal Josephson junction will be examined in detail. As mentioned in Section 5.1 in the description of of the numerical solution, the current is measured in units of $e\Gamma/\hbar = 1\,\mu A$. We have chosen to express all currents in Sections 5.2-5.5 using this specific value for Γ, but it should be kept in mind that this is just to simplify the notation and that the scale is more general, depending on the value of Γ.

One can visualize the dissipation effect in the three-terminal RCSJ model by plotting the differential resistance in a two-dimensional space spanned by two of the bias currents. This has been done in several papers (see e.g. [9], [10], [11], [20]). The differential resistance is determined by first calculating V_1 and V_2 as described in Section 5.1 for a set of (I_1, I_2)-values, and then finding the difference quotients with respect to the bias currents, which results in the four matrices

$$\frac{dV_n}{dI_1} = \frac{V_n(I_1 + dI, I_2) - V_n(I_1, I_2)}{dI_1} \qquad \frac{dV_n}{dI_2} = \frac{V_n(I_1, I_2 + dI) - V_n(I_1, I_2)}{dI_2} \qquad \text{for} \quad n = 1, 2.$$

41

The pixels of the plot are always quadratic, so we have $dI_1 = dI_2 = dI$. The result for $\epsilon_d/\Gamma = 10$ is plotted in the (I_1, I_2)-plane in Figure 5.5. In the case of three terminals, this contains all information since $I_3 = -(I_1 + I_2)$. Replacing I_1 or I_2 by I_3 will result in the same plot mirrored around one of the axes.
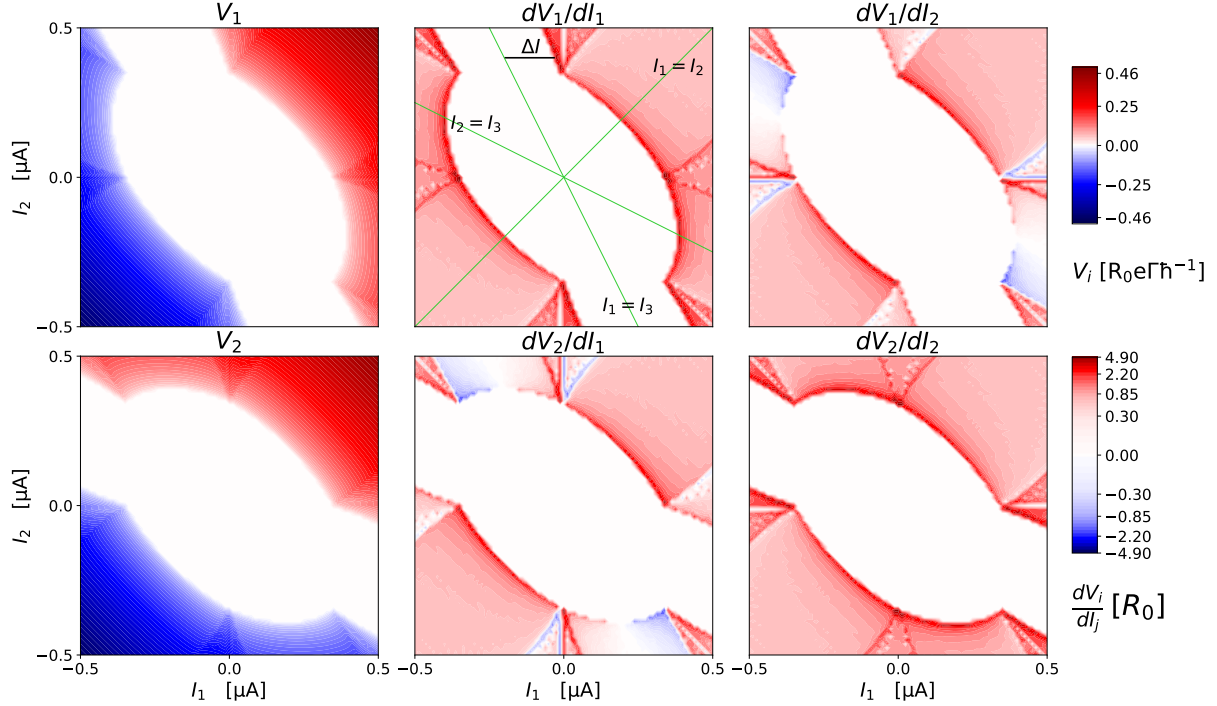

Figure 5.5: Differential resistance map. Leftmost column shows V_1 and V_2 calculated for 80×80 pairs of (I_1, I_2) values. Middle and right column shows the corresponding differential resistance over the left and right paths of the RCSJ circuit. The green lines mark the centers of the branches, and the black horizontal line indicates the branch width ΔI. The parameters used for this plot are $R = 40\,\Omega, C = 40\,\text{fF}, dI = 0.00125\,\mu A$ and $\epsilon_d/\Gamma = 10$. $1\,\mu A = e\Gamma\hbar^{-1}$.

The 2D map over the differential resistance over one junction as a function of bias currents has a characteristic shape with the critical current contour (CCC) enclosing a region of low bias currents that leaves the total system in its superconducting state with all internal currents being dissipationless. The CCC for three different values of ϵ_d/Γ were shown in Figure 3.2 by plotting the Josephson currents from equations (3.11) as a function of (ϕ_1, ϕ_2)-values distributed over the entire phase space. Now, with the inclusion of dissipation via the RCSJ model, we see the resistance building in abruptly around this region. At every boundary between resistance levels, there is a resistance wall.

Another characteristic feature of these plots is the three branches of reduced differential resistance around the three central branch lines $I_2 = I_1$, $I_2 = -2I_1 \, (I_1 = I_3)$ and $I_2 = -I_1/2 \, (I_2 = I_3)$, shown in green in Figure 5.5. The reduced differential resistance results from the fact that along any of these lines supercurrent flows between one pair of terminals, hence supercurrents and dissipative currents coexist inside the branches. The bias currents are distributed over only
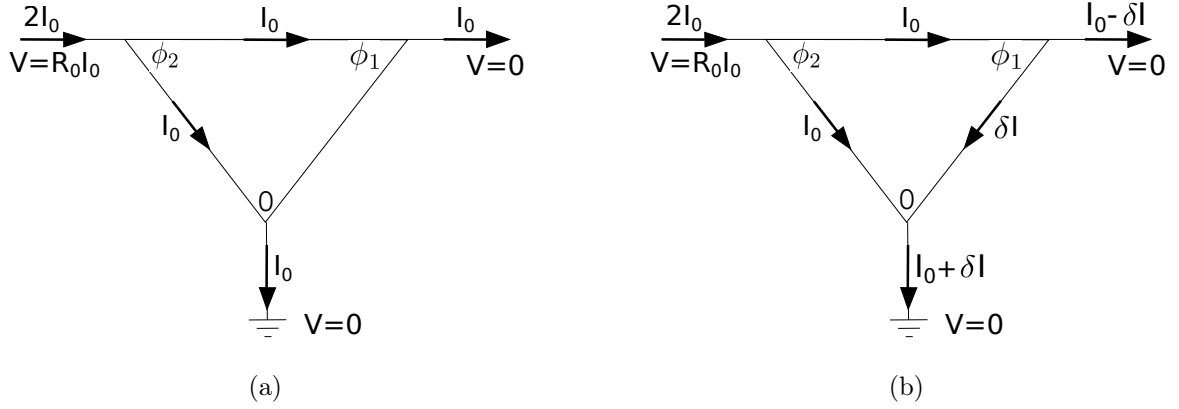
(a)   (b)

Figure 5.6: Current distribution in the three-terminal RCSJ circuit inside the $I_1 = I_3$ branch for $\delta I \ll I_0$. The circuit elements are omitted in the figure for the sake of clarity. (a): At the center $I_1 = I_3$, so no current runs through the ϕ_1 junction, hence $V_1 = 0$. (b): Moving to the right along the horizontal line in the dV_1/dI_1-plot. I_1 differs from I_0 by δI and all of the surplus current δI runs through the ϕ_1 junction.
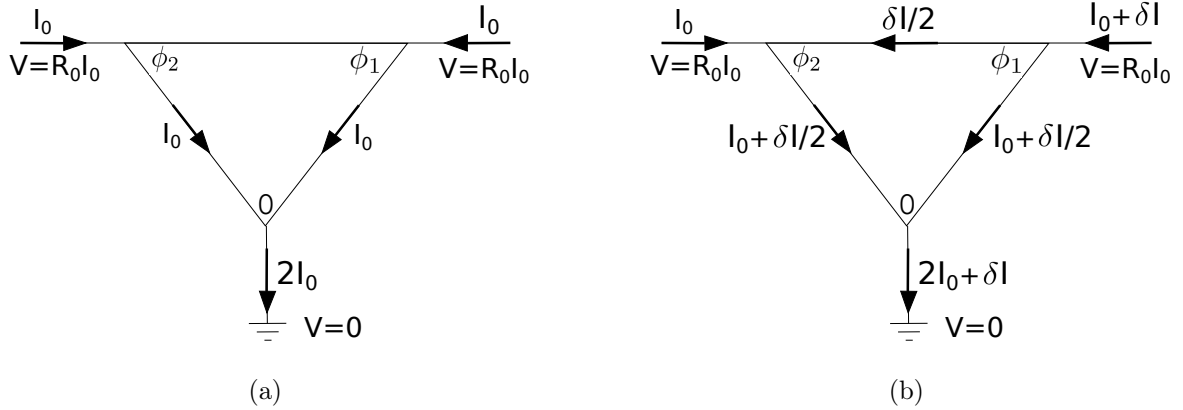

(a)   (b)

Figure 5.7: Current distribution in the three-terminal RCSJ circuit inside the $I_1 = I_2$ branch for $\delta I \ll I_0$. The circuit elements are omitted in the figure for the sake of clarity. (a): At the center $I_1 = I_2$, so no current runs through the $\phi_1 - \phi_2$ junction. (b): Increasing I_1 by δI, half of the surplus current runs clockwise, the other half anti-clockwise since $V_1 = V_2$. Hence this branch has double width in the (I_1, I_2)-plane compared to the others.

two of the junctions, thus one junction is at a zero voltage, as one can confirm by looking at the RCSJ model in figures 5.6a and 5.7a showing the current distributions along the $I_1 = I_3$ and $I_1 = I_2$ lines, respectively. The example shown in the first figure, Figure 5.6a, represents the parameter configuration inside the $I_1 = I_3$ branch where the ϕ_1-junction to the right is subjected to a small bias current $\delta I \ll I_0$, such that $\langle \dot{\phi}_1 \rangle = 0$ and hence $V_1 = 0$.

The physical origin of the branches tells us that, in principle, the branches continue out to infinity. If we follow a horizontal or vertical path from the central branch lines, like the black path shown in Figure 5.5, one can be convinced that the distance ΔI from the central branch line to the resistance wall is related to the critical current of the $V = 0$ junction, by looking at the RCSJ model under these conditions shown in figures 5.6b and 5.7b. This distance ΔI will be referred to as the branch width.

The configurations of the circuit model in figures 5.6 and 5.7 explain why the $I_1 = I_2$ branch is twice as wide as the two others. In the $I_1 = I_3$ case, the voltage conditions mean that the current over the top and the left paths must be equal, which means that all the excess current δI must simply flow over the right path. The situation is the same for $I_2 = I_3$, with reversion of "right" and "left", while in the $I_1 = I_2$ case the voltage drop over right and left is the same, so the excess current δI is equally split between the clockwise and anti-clockwise paths.

The third feature of Figure 5.5 is the thin lines of zero resistance appearing outside the CCC that are visible for $I_2 = -I_1$ and $I_1 = 0$ on the dV_1/dI_1-plot and for $I_2 = -I_1$ and $I_2 = 0$ in the dV_1/dI_1-plot. These are the most stable multiplet resonances, originating from the voltage conditions $V_2 = -V_1, V_2 = 2V_1$ and $V_1 = 2V_2$.

In the first subsection, the physical origin of the branches will be unfolded in the limit of large detuning and large bias currents. The width of the branches turns out to depend on the detuning, the magnitudes of the bias currents and the Q-factor, which will be discussed in the following subsection. In the third subsection, the multiplet resonances will be discussed.

We focus on the $I_1 = I_3$ branch in the following, but the results of course apply to any branch.

5.2.1   Branch Width in the Limit of $I_2 \gg I_{c,0}$ and $\epsilon_d \gg \Gamma$

In this subsection we focus on determining ΔI in the limit far from the CCC and far from resonance between the quantum dot and the superconductors. This is the limit where the approximation is valid for the potential

$$\lim_{\epsilon_d/\Gamma \to \infty} \tilde{U}(\phi_1, \phi_2) = -\frac{2\Gamma}{\epsilon_d}\big(3/2 + \cos(\phi_1 - \phi_2) + \cos(\phi_1) + \cos(\phi_2)\big) - \tilde{I}_1\phi_1 - \tilde{I}_2\phi_2 \qquad \text{with } \tilde{I}_{c,0} = \frac{2\Gamma}{\epsilon_d}.$$

Together with the condition of large bias currents, this means that the washboard can be regarded as flat and that $I_{c,0}$ as constant. For large bias currents, it is possible to determine the branch width ΔI analytically. It has already been discussed why the differential resistance is reduced on and within small deviations from the central branch lines. The voltage conditions inside the

branch and the maximal deviation ΔI can be shown more precisely with an analytical solution from the RCSJ equation (5.1) directly in this limit. We consider the case $I_1 = I_3 \Leftrightarrow I_1 = -I_2/2$ and assume a constant mean terminal velocity, i.e. $\langle \ddot{\phi}_1 \rangle = \langle \ddot{\phi}_2 \rangle = 0$ for $t \to \infty$, in which case the RCSJ equation reduces to

$$\begin{pmatrix} \langle \dot{\phi}_1 \rangle \\ \langle \dot{\phi}_2 \rangle \end{pmatrix} = \begin{pmatrix} 0 \\ \frac{3}{2} I_2 \end{pmatrix} - \begin{pmatrix} 2\langle I_{J,1} \rangle + \langle I_{J,2} \rangle \\ \langle I_{J,1} \rangle + 2\langle I_{J,2} \rangle \end{pmatrix}.$$

If the bias currents are inside the CCC, they equal the Josephson currents such that $\langle I_{J,1} \rangle = -\langle I_{J,2} \rangle/2$, yielding $\langle \dot{\phi}_1 \rangle = \langle \dot{\phi}_2 \rangle = 0$, which we can consider a sanity check. Outside the CCC along the $I_1 = I_3$ line, we know that both Josephson currents average to zero, so we have that $\langle \dot{\phi}_1 \rangle = 0$ and $\langle \dot{\phi}_2 \rangle = \frac{3}{2} I_2$. This harmonizes with the result expected from the circuit arguments that $V_1 = 0$.

Now we introduce a deviation $I_1 = -I_2/2 + \delta I$, i.e. we shift I_1 and thereby I_3 along the black line in Figure 5.5. As an ansatz we use $\langle \dot{\phi}_2 \rangle = \frac{3}{2} I_2$ and assume that ϕ_2 varies fast with respect to ϕ_1 such that $\dot{\phi}_2 \gg \dot{\phi}_1$ and the average Josephson currents reduce to $\langle I_{J,2} \rangle = 0$ and $\langle I_{J,1} \rangle = \langle I_{c,0} \sin(\phi_1) \rangle$. The RCSJ equation becomes

$$\begin{pmatrix} \langle \dot{\phi}_1 \rangle \\ 0 \end{pmatrix} = \left(\delta I - \langle I_{c,0} \sin(\phi_1) \rangle \right) \begin{pmatrix} 2 \\ 1 \end{pmatrix}$$

from which we see that $\delta I = \langle I_{c,0} \sin(\phi_1) \rangle$ and $\langle \dot{\phi}_1 \rangle = 2\delta I - 2\langle I_{c,0} \sin(\phi_1) \rangle = 0$. Evidently, the maximal deviation within the $V_1 = 0$ condition, provided that $\langle \phi_1 \rangle = \pi/2$ at this point, is $\Delta I = I_{c,0}$.

We can now compare this to our numerical results. Inside the branch, the particle is confined to a single unit cell of ϕ_1 as it was seen in Figure 5.4 for low bias currents. From this plot we can confirm the results $\langle \dot{\phi}_1 \rangle = 0$ and $\langle \dot{\phi}_2 \rangle = \frac{3}{2} I_2$. The mean value of ϕ_1 after the convergence time switches from $\langle \phi_1 \rangle = 0$ at $\delta I = 0$ to $\langle \phi_1 \rangle = \pi/2$ at $\delta I = \Delta I$. From the analytical result above, this means that δI does reach exactly the maximally possible value $\Delta I = I_{c,0}$. The result is symmetric so when $\delta I = -\Delta I, \langle \phi_1 \rangle = -\pi/2$. Hence, in this limit along this line, we observe the fictitious washboard particle moving in an effective 1D potential of the well-known form $U(\phi_1) \propto \cos(\phi_1) - \frac{\delta I}{I_{c,0}} \phi_1$. This makes sense since the 2D washboard potential in this limit can be decomposed into a sum of three 1D potentials with $E_J = \Gamma^2/\epsilon_d$. In the next subsection we will look at the effect of moving away from this simplifying limit.

5.2.2 Branch Width Dependence on Detuning, Bias Currents and Q Factor

As long as the bias currents are much larger than the critical current, the effect of varying the detuning is negligible since the potential is dominated by the tilted plane $-(I_1 \phi_1 + I_2 \phi_2)$. We therefore start out by discussing the dependence of ΔI on decreasing the bias current magnitudes while keeping the detuning large such that we can still treat $I_{c,0}$ as a constant.

We consider the case where $I_2 = 2I_{c,0} + 2\epsilon$ and $I_1 = -I_2/2 + \delta I$ like in Figure 5.6, with $\epsilon \ll I_{c,0}$. Then the currents over the top and left paths are $I_{c,0} + \epsilon$.

If we look at the instantaneous current over the two resistors, it varies between $I_R \in [\epsilon; 2I_{c,0} + \epsilon]$. Intuitively, this is an unstable situation since the dissipation, and hence also the instantaneous voltage drops over the two paths, varies wildly. The results are therefore sensitive to the time scales of variations in the parameters. When $\delta I = 0$, the currents over the top and left paths vary with both the same frequency and phase, since when $\phi_1 = 0$ their respective Josephson currents are equal. As $\delta I \to \Delta I$, the currents over the top and left paths get out of phase. In case ϕ_1 reaches $\pi/2$ while V_1 is still zero, the current over the resistor of the left path will be ϵ, so essentially dissipationless, while the current over the resistor of the top path will be $I_{c,0} + \epsilon$. One can reason that since the dissipation over the two other paths approaches zero periodically, the currents will redistribute at these instants such that more current than δI is forced over the right path, which causes a reduced branch width ΔI. Intuitively, ΔI would converge to its ideal value $I_{c,0}$ when $I_2/2 \gg I_{c,0}$, so that the currents over the resistors can be approximated as constant.

The value of $\langle \phi_1 \rangle$ in the limit of $\delta I \to \Delta I$ is observed numerically to decrease for low bias currents to a minimum of $\langle \phi_1 \rangle = 0.466\,\pi$ at the CCC where $I_2 = 0.40\,\mu A$. Since the value of $\langle \phi_1 \rangle$ at $\delta I = \Delta I$ is shifted away from $\langle \phi_1 \rangle = \pi/2$, the branch width is slightly reduced. Besides of this, the dynamics can be shown to depend on the initial value of ϕ_2 if one sets $Q \gg 1$. Hence, outside the limit of $I_2 \gg I_{c,0}$, the potential inside the branch along the horizontal line from the center to the edge of the branch can no longer be described by the usual one-dimensional washboard potential.

Starting from the CCC at large detuning, the branch width is observed to initially increase fast with I_2 and approach the mean value of the Josephson current over the right (ϕ_1) junction, $\langle I_{J,R} \rangle$, asymptotically, i.e.

$$\Delta I = \langle I_{J,R} \rangle = \frac{1}{T} \int_{t_{conv}}^{\infty} I_{c,0}(\phi_1, \phi_2) \sin(\phi_1) \mathrm{dt},$$

as it was shown analytically in the last subsection. The dependence of ΔI on bias magnitude is shown in Figure 5.8a. The values of ΔI are found by decreasing I_1 from the central branch line $I_1 = I_3$ until the point where any net displacement in the ϕ_1 direction is observed. The difference in I_1 from this point to the $I_1 = I_3$ line is ΔI.

If the detuning is also decreased, the problem is intractable, since $I_{c,0}$ is an additional oscillating quantity. In the washboard analogy, the particle is no longer sliding down a plane, but rolling down the rungs of a tilted washboard in the ϕ_1 direction, so the slope along the ϕ_2 direction is varying. This is clearly a regime of additional complexity, where ΔI cannot be predicted analytically.

The measured ΔI as a fraction of $\langle I_{J,R} \rangle$ is shown in Figure 5.8b for $I_2 \gg I_{c,0}$. The branch widths are found by the method described for Figure 5.8a, while the mean value of the Josephson current is found by using the numerical results for $\phi_1(\tilde{t})$ and $\phi_2(\tilde{t})$ at the point where $\delta I \to \Delta I$.
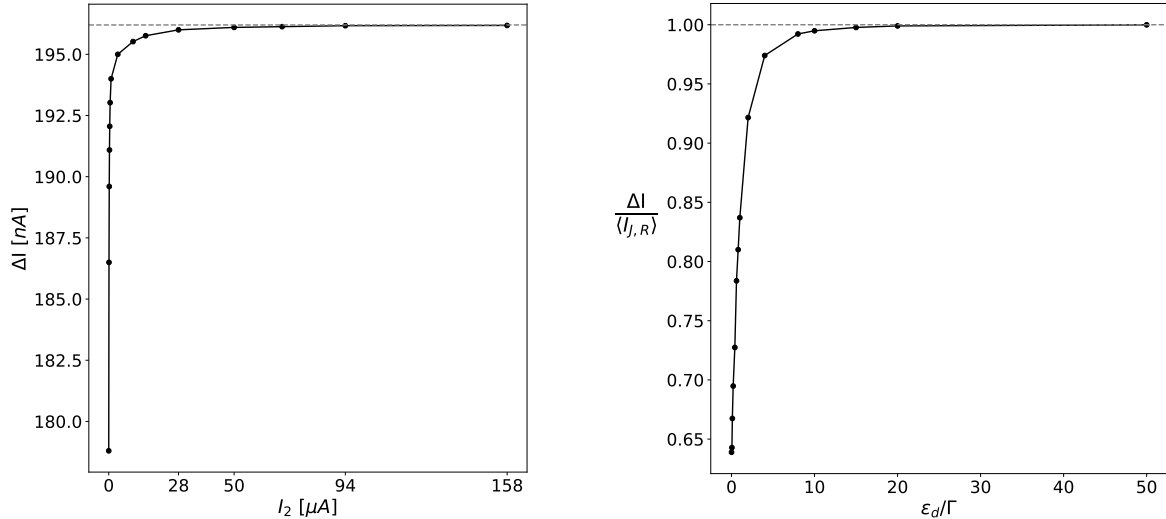
(a) $I_1 = I_3$ branch width dependence on current bias magnitude for $\epsilon_d/\Gamma = 10$. The horizontal line indicates the maximal value $\Delta I = 0.19619\,\mu A$. The last seven points are exact, otherwise the widths are given at a resolution of 0.1 nA.
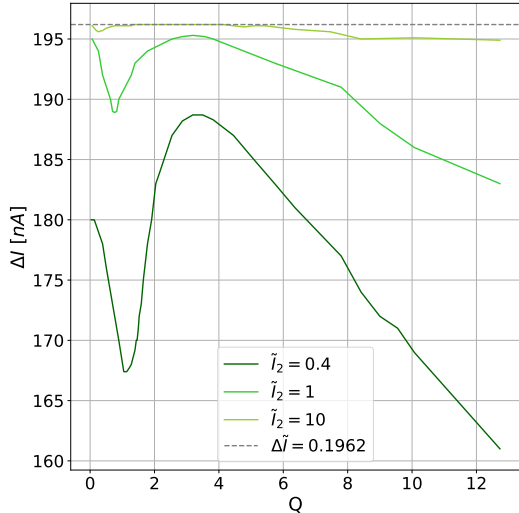
(b) $I_1 = I_3$ branch width dependence on detuning. In this plot $I_2/\langle I_{c,0}\rangle \gg 1$, i.e. for $\epsilon_d/\Gamma = 10$, ΔI is the horizontal line in Figure 5.8a.

Figure 5.8: Outside the limit $I_2 \gg I_{c,0}$ and $\epsilon_d/\Gamma \gg 1$, the width of the branches of the differential resistance plot (Fig. 5.5) decreases, as shown as a function of each parameter. Here $Q = 0.25$.

The two figures have not yet been fully understood. It has been argued quite loosely why a decreased width is expected for small bias currents, and in particular for $I_2 < 4I_{c,0}$ where the current over the shunt resistor is not always larger than the current over the junction. The small shift in maximal $\langle \phi \rangle$ is certainly not sufficiently large to account for the abrupt decrease in width for low bias currents. Regarding the dependence on detuning, the decrease in width is suspected to be related to the decomposition of the three-terminal Josephson junction into the three two-terminal Josephson junctions of the RCSJ model, which is an increasingly poor approximation as resonance is approached.

In order to gain more insight to the functions, it was considered fitting the two functions to power laws, but this would require a higher resolution and additional data points which would be a relatively big project for a laptop considering the long run time for high values of current and detuning. In particular for Figure 5.8b, the measurements are affected by the propagated uncertainties in ΔI and $\langle I_{J,R}\rangle$. Figure 5.8 should therefore not be overinterpreted but simply be taken as an illustration of the stability in the limit of large detuning and bias currents together with an abrupt shrink in branch width in the region close to the CCC.

Additionally to detuning and bias magnitude, the branch width depends on Q close to the CCC. The width as a function of Q is shown for three different I_2 values along the $I_1 = I_3$ branch in Figure 5.9a. In the regime where inertia dominates drag, starting already from $Q \geq 3$, the width decreases linearly. This can be explained by the oscillations in ϕ_1 of the trajectory becoming

47

(a) $I_1 = I_3$ branch width dependence on Q. $\epsilon_d/\Gamma = 10$. The local minimum of the $\tilde{I}_2 = 0.4$ curve is centered around $Q = 1.09$. The resolution is 0.1 nA for the $\tilde{I}_2 = 10$ curve, and 1 nA for the two other curves.
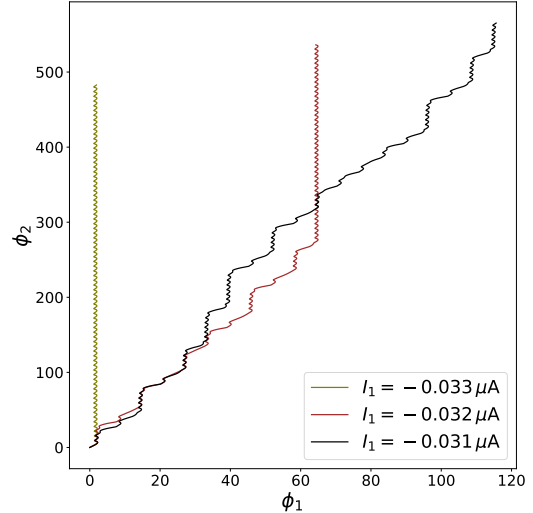
(b) Particle trajectories for Q = 1.21 just at the boundary of the $I_2 = -2I_1$ branch for $\tilde{I}_2 = 0.4$. $\Delta\tilde{I} = -0.032 = -0.2 + 0.169$. The integration time is $1100\,t_0$ for all three trajectories.

Figure 5.9: (a): Dependence of the branch width ΔI on Q close to the CCC. (b): Chaotic dynamics at the local minimum in (a), $Q \approx 1$.

increasingly large when increasing Q, which means it requires a larger tilt in the ϕ_1 direction to prevent the particle from overcoming the barrier to the neighboring unit cell in the ϕ_1 direction and hence obtaining a nonzero $\langle\dot{\phi}_1\rangle$.

For lower Q, the dependence is quadratic around $Q = 1$. The minimum around $Q = 1$ happens because the dynamics is chaotic around this point where all the energy scales have the same order of magnitude, i.e. drag $\approx$ inertia. If one sets a constant $I_{c,0} = 2\Gamma/\epsilon_d$ and define Q conventionally by this value, the minimum is exactly at $Q = 1.00$. A demonstration of chaotic behaviour for $Q = 1.21$ is seen in Figure 5.9b. The three trajectories have equal integration times of $1100\,t_0$ and are equal for the first 2.5 unit cells, after which the evolution of the two trajectories outside the branch continues in a non-periodic, unpredictable manner. Remarkably, the trajectory stops evolving in the ϕ_1 direction after $500\,t_0$. It randomly flips back to the $V_1 = 0$ state, which would cause severe errors in the voltages determined with the current method, if the code was operated at this Q. Again, this show unstable conditions which causes a local minimum in ΔI.

To pick up on the 1D result from Section 2.1 that for $Q \ll 1$ the $I - V$ relation is described by $V = R\sqrt{I^2 - I_c^2}$, we will as a last thing in this subsection find the $I - V$ relation for the three-terminal Josephson junction. For $Q = 0.25$, V_2 along the $I_1 = I_3$ branch line is shown in red in Figure 5.10 together with the Ohmic case $V_2 = R_0 I_2/2$ in solid black and $V_2 = R_0\sqrt{I_2^2 - I_{c,0}^2}/2$ in dotted black, showing a good agreement with the $Q \ll 1$ approximation for the $I - V$ relation. Note that this Q is relatively high, but since the $\ddot{\phi}$ term in the 2D RCSJ equation is proportional
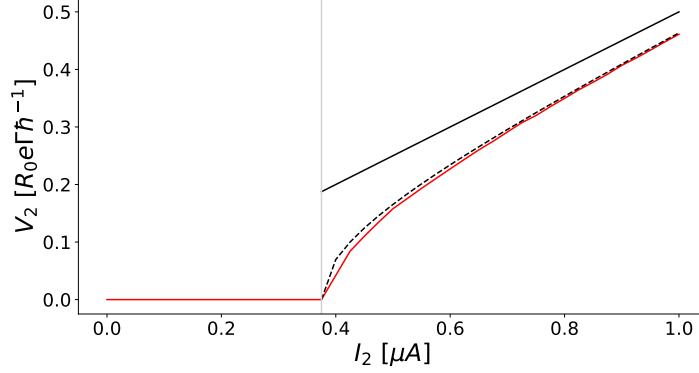
Figure 5.10: $I - V$ relation along the $I_1 = I_3$ branch at $Q = 0.25$ (red), Ohmic relation (solid black) and $V_2 = \frac{R_0}{2}\sqrt{I_2^2 - I_{c,0}^2}$ (dotted black). $R_0 = 40\,\Omega$.

to Q^2 (see (5.1)), the approximation is expected to generalize to $Q^2 \ll 1$.

5.2.3 Multiplet Resonances

Until now, two types of conditions under which the differential resistance is zero or reduced with respect to the resistance for a random pair of large bias currents, has been discussed. One is the zero-voltage state inside the critical current contour (CCC) where the condition is $V_1 = V_2 = 0$ and hence $\langle \dot{\phi}_1 \rangle = \langle \dot{\phi}_2 \rangle = 0$ so the junction carries supercurrents only. The other set of conditions is fulfilled for the branches, inside which either $V_1 = 0, V_2 = 0$ or $V_1 - V_2 = 0$ such that either $\langle \phi_1 \rangle, \langle \phi_2 \rangle$ or $\langle \phi_1 - \phi_2 \rangle$ is stationary with respect to the phase of the grounded terminal, and there is a mixture of supercurrents and dissipative currents in the junction.

This subsection is devoted to a third set of conditions which reduces the differential resistance significantly, of which a few examples can be seen in Figure 5.5. The concept of multiplets was introduced in Section 2.4.2. If the relation $pV_1 = qV_2$ is fulfilled for any set of integers (p, q), $\langle p\phi_1 - q\phi_2 \rangle$ is stationary. For example if $V_1 = -V_2$, we have $\langle \dot{\phi}_1 + \dot{\phi}_2 \rangle = 0 \rightarrow \langle \phi_1 + \phi_2 \rangle = \text{const.}$ The visible of the lines in Figure 5.5 fulfil the conditions $I_2 = -I_1$, in which case $V_2 = -V_1$ and $dV_1/dI_1 = dV_2/dI_2 = 0$, or $I_i = 0$, which means $V_j = 2V_i$ and $dV_i/dI_i = 0$ for $(i, j) = (1, 2)$ and $(i, j) = (2, 1)$. In order to focus on the multiplet resonances, a small region of the differential resistance dV_1/dI_1 in (I_1, I_2)-space is plotted in Figure 5.11 at full integration resolution as described in Section 5.1 and with a pixel size of $1/600\,\mu A$. To maximize the widths of the multiplet resonances, $R = 160\,\Omega$ and $C = 30$ fF so that $Q = 0.88$ in this plot. This is based on the dependence on C described in Ref. [10]. The coloured lines on top of the simulation have the ideal slopes found from the circuit model shown in Figure 5.13, which show two examples of the current distribution for fixed voltage conditions. The black dotted line shows the cross section of the plot for which the ratio of V_2 to V_1 has been plotted on the right side. This plot clearly encapsulates seven of the resonances as plateaus in V_2/V_1 at rational numbers, in agreement with the condition for multiplet resonances.
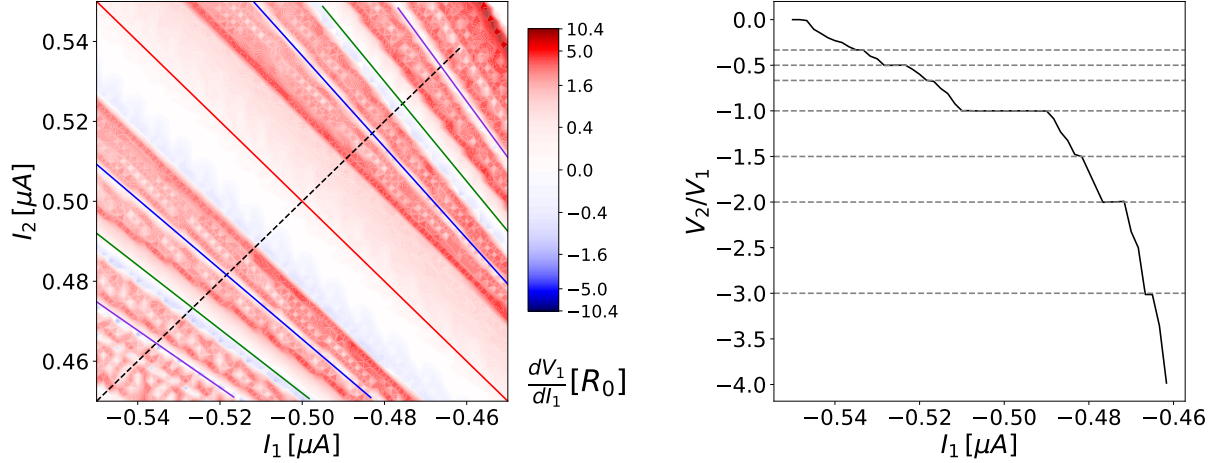
Figure 5.11: Left: dV_1/dI_1 at $Q = 0.88$ and $\epsilon_d/\Gamma = 10$. This plot is 60×60 pixels. The coloured lines show the ideal slopes of the curves; -5/7 and -7/5 (violet), -4/5 and -5/4 (green), -7/8 and -8/7 (blue) and -1 (red) found from the voltage conditions (see Figure 5.13 for examples). The dotted black line shows the cross section for which the ratio V_2/V_1 is calculated. Right: Ratio of V_2/V_1 along the dotted black line on the left plot. The seven horizontal dotted lines show the values at the plateaus which correspond to each of the coloured lines in the left plot.

The ideal slopes of arbitrary multiplets can also be derived from (5.1). As an example for the sextet $\langle \dot{\phi}_1 + 2\dot{\phi}_2 \rangle = 0$, this can be shown by changing variables to $\epsilon = (\phi_1 + 2\phi_2)/2$, $\eta = (2\phi_2 - \phi_1)/2$ and expressing (5.1) in terms of (η, ϵ). This gives the equation for ϵ

$$\ddot{\epsilon} + \frac{1}{RC}\dot{\epsilon} + \frac{2e}{\hbar}\frac{I_{c,0}}{3C}\left(\frac{5}{2}\sin\left(\frac{\epsilon+\eta}{2}\right) + \frac{1}{2}\sin\left(\frac{3}{2}\eta - \frac{1}{2}\epsilon\right) + 2\sin(\epsilon - \eta)\right) = \frac{2e}{3C\hbar}\left(\frac{5}{2}I_2 + 2I_1\right).$$

Averaging the equation over long times or over one period of η, we have that the left side of the equation must be equal to zero, which gives the result that $I_2 = -4I_1/5$ as stated previously.

The ideal slopes are seen to not fit the numerical result of Figure 5.11 perfectly. The lines are bent in towards the quartet resonance in this region, just like the edges of the branches curve towards the central branch lines.

The lines in Figure 5.11 are not fitted, but simply have the ideal slopes, which are then shifted up (for $-V_2/V_1 < 1$) or down (for $-V_2/V_1 > 1$) by an offset of magnitude increasing with distance

to the quartet resonance. The formulas for the seven lines are given below:

$$V_2 = -\frac{1}{3}V_1: \qquad I_2 = -\frac{5}{7}I_1 + 0.082\,\mu A$$

$$V_2 = -\frac{1}{2}V_1: \qquad I_2 = -\frac{4}{5}I_1 + 0.052\,\mu A$$

$$V_2 = -\frac{2}{3}V_1: \qquad I_2 = -\frac{7}{8}I_1 + 0.028\,\mu A$$

$$V_2 = -V_1: \qquad I_2 = -I_1$$

$$V_1 = -\frac{2}{3}V_2: \qquad I_2 = -\frac{8}{7}I_1 - 0.035\,\mu A$$

$$V_1 = -\frac{1}{2}V_2: \qquad I_2 = -\frac{5}{4}I_1 - 0.070\,\mu A$$

$$V_1 = -\frac{1}{3}V_2: \qquad I_2 = -\frac{7}{5}I_1 - 0.119\,\mu A$$

The offsets arising from the multiplets curving inwards can be explained by the bias currents being very close to the CCC. This region was chosen to capture several multiplets with high resolution and affordable integration time. In order to illustrate the convergence of the multiplet curves, similar plots have been made for increasingly large bias values, following the sextet with $V_2 = -2V_1$. By the same method of keeping the slope constant, the results are

$$I_1 = -0.55\,\mu A: \qquad I_2 = -\frac{5}{4}I_1 - 0.070\,\mu A$$

$$I_1 = -1.00\,\mu A: \qquad I_2 = -\frac{5}{4}I_1 - 0.038\,\mu A$$

$$I_1 = -1.25\,\mu A: \qquad I_2 = -\frac{5}{4}I_1 - 0.029\,\mu A$$

$$I_1 = -1.50\,\mu A: \qquad I_2 = -\frac{5}{4}I_1 - 0.021\,\mu A$$

$$I_1 = -3.05\,\mu A: \qquad I_2 = -\frac{5}{4}I_1 - 0.005\,\mu A \qquad (5.2)$$

From this it should be safe to assume that all multiplets converge towards their ideal slopes for $I_2 \gg I_{c,0}$. This is an additional example of the increased complexity of the dynamics in the region close to the CCC.

Multiplets from the RCSJ model

With the results found in this section, it has been demonstrated that multiplet resonances arise from simulations of the three-terminal RCSJ model, in agreement with Ref. [10]. Now the question is still open how multiplets appear from the RCSJ model. In Ref. [10], the stability of the quartet resonance was found to be analogous to the stability of the inverted position of the pendulum in Kapitza's pendulum problem. The following is a resumé of the analytical argument for the presence of the quartet resonance in this paper. By changing variables to $\eta = (\phi_2 - \phi_1)/2$ and $\epsilon = (\phi_2 + \phi_1)/2$ and using the approximation $\eta = e\hbar^{-1}(V_2 - V_1)\,t$, the differential equation for the phases in the three-terminal RCSJ model (see (5.1)) is rewritten to

$$\ddot{\epsilon} + \frac{\omega_0}{Q}\dot{\epsilon} + \omega_0^2\cos(\eta)\sin(\eta) = I_1 + I_2,$$

with $Q = \omega_0 RC$. The approximation for η is claimed to be valid for sufficiently high bias and Q factor. The thresholds are not made clear, but it is shown that for $R = 160\,\Omega, C = 30$ fF and $I_2 - I_1 = 6\,\mu A$, the approximation that η is linear in time is valid. This equation for ϵ is identical to the equation for the angle of Kapitza's inverted pendulum in the absence of gravity. The fast oscillations of $\cos(\eta)$ correspond to the vibration of the pivot point of Kapitza's pendulum. Exactly at the quartet resonance, $\epsilon = 0$ and $I_2 = -I_1$ and the equation is solved. The time derivative $\langle \dot{\epsilon} \rangle = 0$ by definition of the quartets, so that the differential resistance in this frame, $d\langle \dot{\epsilon} \rangle / d(I_1 + I_2) = 0$ which necessarily results in $dV_1/dI_1 = dV_2/dI_2 = 0$. This explains why the quartet condition is evident as a branch of reduced differential resistance.

The equilibrium of ϵ at 0 or π is shown to be stable for small deviations around $I_1 + I_2 = 0$, which explains the finite width of the quartet resonance at $I_2 = -I_1$. The width can be seen as a measure of the stability of the conditions at the center of a branch in the differential resistance map. In the undamped ($Q > 1$) case, this is made more precise by deriving

$$|I_1 + I_2| < \frac{\hbar I_C^2}{4eC(V_2 - V_1)^2}. \tag{5.3}$$

This relation is then backed up by simulations, concluding that the width of the multiplet resonances of the three-terminal Josephson junction for $Q > 1$ depend on the (equal) capacitances as $1/C$. It cannot explain, however, the observed peak in width versus C at $Q = 1$ (quartets) or lower (other multiplets). Keeping the resistances constant at $R = 160\,\Omega$, the width of the multiplet resonance at $I_2 = -I_1$ is shown to peak around $C = 40$ fF with a width of around 220 nA after which it decreases as $1/C$ so that the width has decreased by a factor of 2 around $C = 125$ fF. Other multiplet resonances are shown to have the same dependence on C, though peaking at lower C values and vanishing faster.

Multiplet stability dependence on Q

The description of the dynamics in terms of Q in previous chapters of this thesis led to testing of the theory that the width of the multiplet's dependence on resistance and capacitance can also be collected in a quality factor term. This seems plausible from (5.3) of Ref. [10], since $V \propto R_0$ such that the equation for the quartet width stated is proportional to $1/Q$. An example of the result of letting $R \to \gamma R$ versus letting $C \to \gamma^2 C$ in the multiplet simulation is shown in Figure 5.12 for $Q = 2.65$. Small numerical variations are evident, but the plots indisputably have the same features of a clearly visible quartet branch and slightly visible sextet branches ($V_1 = -2V_2$ and $V_2 = -2V_1$). From this figure it is probable that the variation in multiplet widths as a function of R and C can be described adequately via the Q factor. Additionally, from the plot we see that the quartet branch is as stable as in the $Q = 0.88$ case for the lowest bias values, but is seen to weaken faster for larger bias. The higher-order multiplets are seen to be very sensitive to the Q factor.

As mentioned, in Ref. [10] it is pointed out that it requires $Q > 1$ and relatively high bias currents around $I_2 - I_1 = 6\,\mu A$ to make the approximations necessary to solve for the multiplet
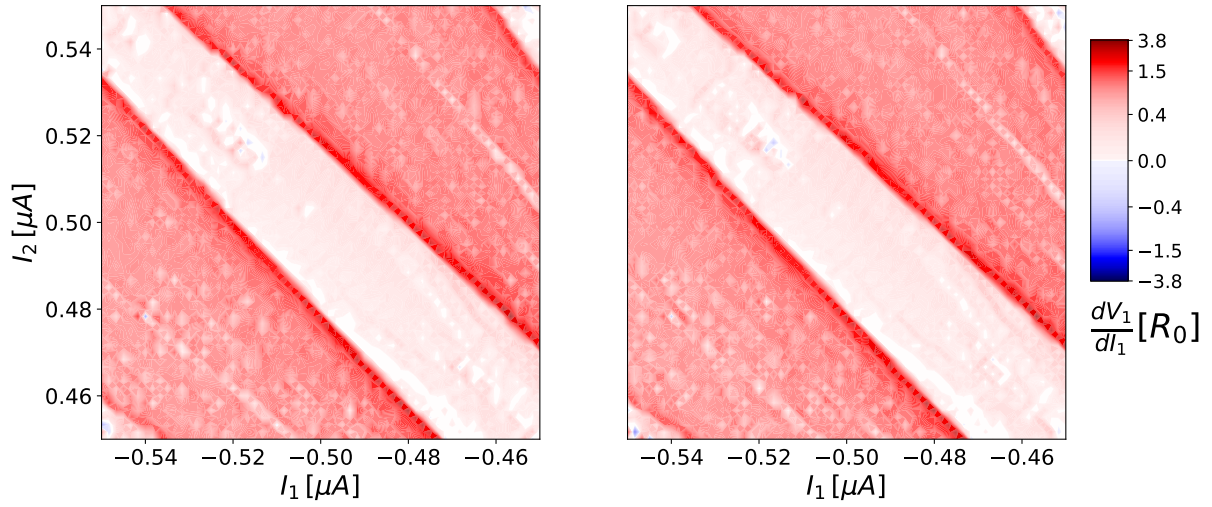
Figure 5.12: dV_1/dI_1 at Q = 2.65. The resolution of the plots is 60×60 pixels. Left: $R = 480\,\Omega, C = 30$ fF. Right: $R = 160\Omega, C = 270$ fF. From this, the multiplet widths are seen to depend on R and C through the Q factor.
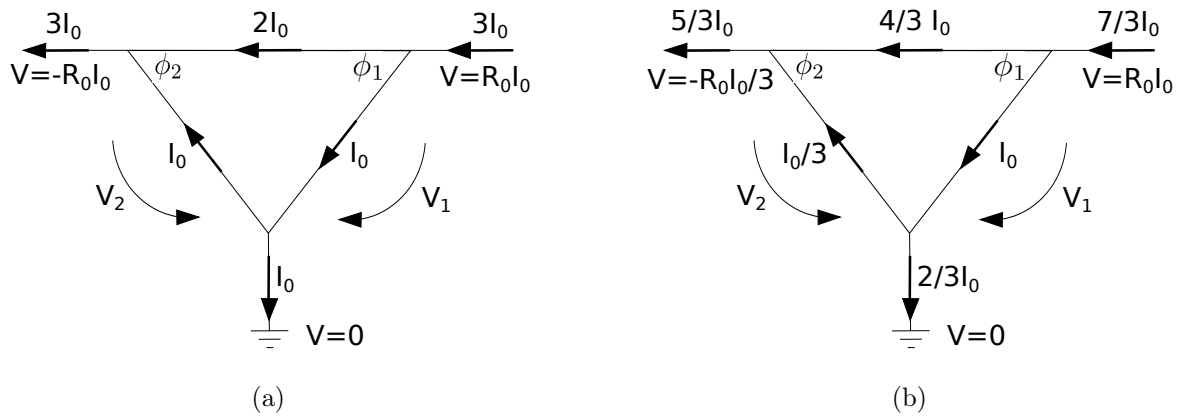

Figure 5.13: Current distributions in two cases that meet the multiplet condition (a): $V_2 = -V_1$ which results in $I_2 = -I_1$ and (b): $V_2 = -1/3V_1$ which results in $I_2 = -5/7I_1$. Lines with these ideal slopes in (I_1, I_2) space are plotted on top of the lines of corresponding voltage conditions in Figure 5.11

conditions analytically and derive the Kapitza's pendulum equation.

Regarding the condition on Q, it is somewhat surprising that a higher Q simplifies the multiplet derivations in this case, based on the role of Q in the dynamics discussed earlier.

Regarding the condition on the current magnitudes, it is reasonable to assume that this limit corresponds to the limit of ideal multiplet slopes. As an approximate method to compare the currents to the results of our model, we reformulate this in units of the CCC width, by which we mean the I_2-coordinate of the CCC along the $I_1 = -I_2/2$ line. In Ref. [10] the CCC width is $I_2 = 1.4\,\mu A$, meaning $I_2 - I_1 = 6\,\mu A$ can be converted to $I_2 = 4\,\mu A = 2.9$ CCC widths.

In Figure 5.11, where the CCC width is $I_2 = 0.35\,\mu A$, the highest bias currents fulfill $I_2 - I_1 = 1.10\,\mu A$ i.e. $I_2 = 2.1$ CCC widths, which is below the threshold. The deviation from $I_2 = -5I_1/4$ for the sextet was found to be vanishing for $I_2 - I_1 = 6.84\,\mu A$ in (5.2), i.e. $I_2 = 13.0$ CCC widths, which should be well within the regime of the approximation. In our model, 2.9 CCC widths corresponds to $I_2 = 1\,\mu A$, so already the second measurement of (5.2) where the multiplet was found at $(\tilde{I}_1, \tilde{I}_2) = (-1.00, 1.25 - 0.038)$ should be within the approximation. This is reasonable, since this I_2 only deviates by $3\,\%$ from its ideal value. Thus the two findings are found to be in agreement.

In this subsection it has been shown that multiplet resonances are visible in the differential resistance map of the three-terminal RCSJ model stated in Section 5.1. The I_2/I_1 relations of the resonances have been found, both analytically directly from the RCSJ differential equation and from Kichhoff's laws in the circuit model, and it has been shown that they bend towards the quartet resonance for low bias currents. A partial derivation of the stability of the quartet resonance from the RCSJ model according to Reference [10] was restated. The results of the paper were supplemented by the statement that the width of the multiplets are Q-dependent, adding to the list of properties of the three-terminal RCSJ equation that depend on Q.

How to distinguish between the two fundamentally different origins of the multiplets, since differential resistance cannot, remains an open question. Regardless of this, it is established that it is possible to generate stable supercurrents under high bias conditions where all phases are winding, which is quite remarkable.

5.3   Differential Resistance in the Presence of a Magnetic Field

In this section the theoretical predictions of how the differential resistance of the three-terminal Josephson junction changes in response to an external flux will be investigated. The model including the flux is set up, after which it is solved numerically and the results are analyzed.

First, we consider a flux Φ through the RCSJ circuit loop of Figure 5.1. Due to the flux quantization condition discussed in Section 2.2, one of the Josephson junctions' phase is shifted by $2\pi\Phi/\Phi_0$. An initial guess could therefore be that the energy of the three-terminal Josephson

junction changes to

$\varepsilon \to -\Gamma\sqrt{(\epsilon_d/\Gamma)^2 + 3 + 2\big(\cos(\phi_1) + \cos(\phi_2 + 2\pi\Phi/\Phi_0) + \cos(\phi_1 - \phi_2)\big)}$. However, if $\epsilon_d/\Gamma < \sqrt{3}$, the energy takes imaginary values for some phase configurations, which writes off this solution as clearly unphysical. This is no surprise since the model treats the junction as zero-dimensional, so this model does not support a flux through the center.
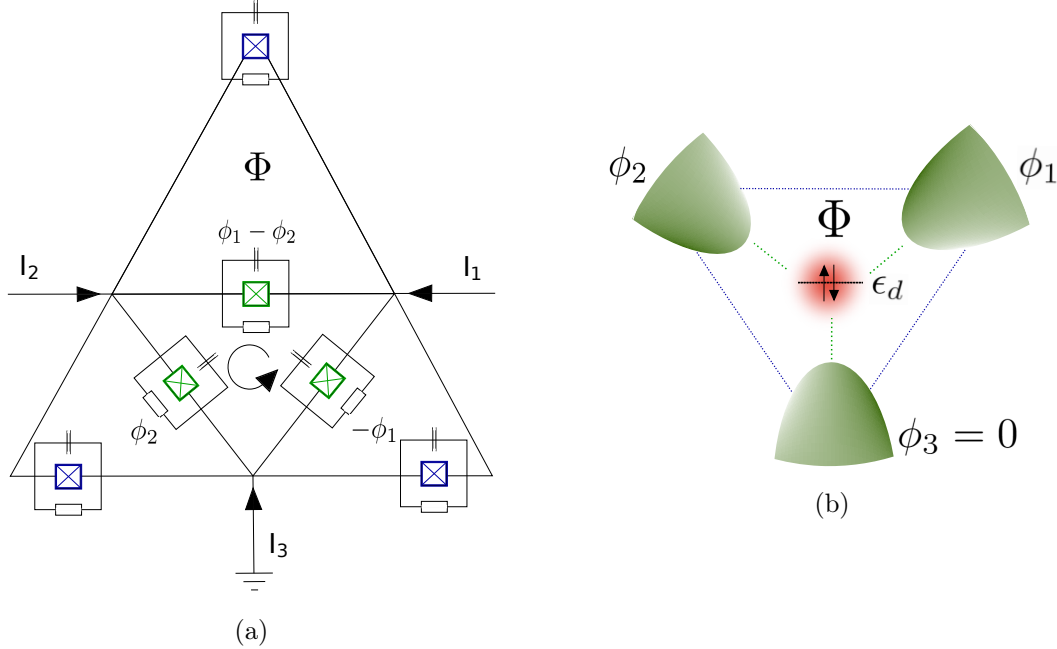

Figure 5.14: Left: RCSJ model of a three-terminal Josephson junction with coupling both through quantum dot and directly to neighbors. The Josephson junctions have critical currents $I_{c,0}$ (green) or $I_{c,2}$ (blue). The arrows point towards positive current direction. All resistors have resistance R_0 and all capacitors have capacitance C_0. Right: Three-terminal Josephson junction which the RCSJ model to the left represents.

In order to accommodate a two-dimensional area between the superconducting leads, we now include direct coupling between the neighboring leads as illustrated in Figure 5.14b. The three coupling energies are assumed to be equal and the three new Josephson junctions of the circuit representation shown in blue in Figure 5.14a are shunted by resistance R_0 and capacitance C_0. This modifies (5.1) by

$$
\begin{aligned}
I_{J,1} &\to I_{J,1} + I_{c,2}\big(\sin(\phi_1 - \phi_2 + 2\pi\Phi/\Phi_0) + \sin(\phi_1)\big) \\
I_{J,2} &\to I_{J,2} + I_{c,2}\big(-\sin(\phi_1 - \phi_2 + 2\pi\Phi/\Phi_0) + \sin(\phi_2)\big) \\
t_0 &\to 2\,t_0
\end{aligned}
\tag{5.4}
$$

where $I_{c,2}$ is the critical current of the directly coupled (two-terminal) junctions. Note that this does not completely reduce to (5.1) for $I_{c,2} = 0$ because of the additional resistors and capacitors, but this has no effect on the critical current contours (CCC).

We already know from previous discussion how dV_1/dI_1 and dV_2/dI_2 relate to current bias and

are now focusing on how the CCC and branches of these maps change under a flux bias, so we plot $(dV_1/dI_1 + dV_2/dI_2)/2$ for a range of flux values and direct coupling energies, which highlights the CCC. The result is shown in the CCC table of Figure 5.15. The detuning used for this figure is $\epsilon_d/\Gamma = 10$, where $I_{c,0} \in [0.1915, 0.2000]$. The resolution of the plots of the CCC table is reduced to $dt = 0.5$, integration range $T = 300\,t_0$ and 40×40 pixels for all subplots. This is done to limit the total integration time while one can still clearly see the evolution of the main features, namely the CCC and the branches of reduced differential resistance.

The rest of Section 5.3 will be a detailed analysis of the effects on these main features backed up by physical arguments from the model of Figure 5.14.

5.3.1 General Response of CCC to Flux and Interterminal Coupling Ratio

In this subsection, the overall properties of the CCC's of Figure 5.15 will be discussed, supplemented by remarks on the change of the branch widths and multiplet resonances.

The most striking feature of the table in Figure 5.15 is the quite dramatic change of the CCC as the flux piercing the loop Φ is increased from zero to half a flux quantum. The area of the CCC decreases, and the shape changes from smooth oval to triangle at $\Phi = 3\Phi_0/8$ to square/rhombus at $\Phi = \Phi_0/2$. At zero flux, the CCC is symmetric with respect to inversion around the origin. This is as expected since the circuit is symmetric with respect to reversal of the direction of the bias currents because the magnitude of the current flowing through each junction, which have a critical current symmetric around zero, is conserved. The shape is an ellipse with semi-minor axis along $I_1 = I_2$ of ideal length $\sqrt{2}(I_{c,0} + I_{c,2})$, and semi-major axis of double length along $I_1 = -I_2$. The axis along $I_1 = -I_2$ is reduced in the simulations, below the range of $I_{c,0}$. When a flux is present, a screening current flows in the circuit, because of which the current magnitude through each junction is no longer conserved under sign reversal of I_1 and I_2. This is reflected as a breaking of the inversion symmetry of the CCC. For flux values of $3\Phi_0/8$ and $\Phi_0/2$, the CCC is no longer convex for $I_{c,2} > I_{c,0}$. At $\Phi = \Phi_0/2$, the CCC recovers its inversion symmetry, since at this point all supercurrent through the top part of the circuit runs over the larger junction only (zero current in the $I_{c,2} = I_{c,0}$ case). The part of the circuit consisting of a loop with a flux will be referred to as the SQUID part of the circuit.

The decrease in area as a function of Φ makes sense since an increasingly large screening current is present in the circuit, even in absence of bias currents. The area of the CCC in the case of $I_{c,2} \approx I_{c,0}$ is measured from Figure 5.15 to decrease by a factor of 3 from $\Phi = 0$ to $\Phi = \Phi_0/2$. The decrease is larger for increasing $I_{c,2}$ so that the area at $I_{c,2} \approx 2I_{c,0}$ decreases with the same factor already at $\Phi = 3\Phi_0/8$.

On the other hand, the area increases as a function of $I_{c,2}$. Obviously, for $I_{c,2} = 0$, no current can go through the blue junctions, the flux has no effect and the problem reduces to the simpler three-terminal RCSJ circuit. Increasing the critical current to $I_{c,2} = I_{c,0}$, the three loops become

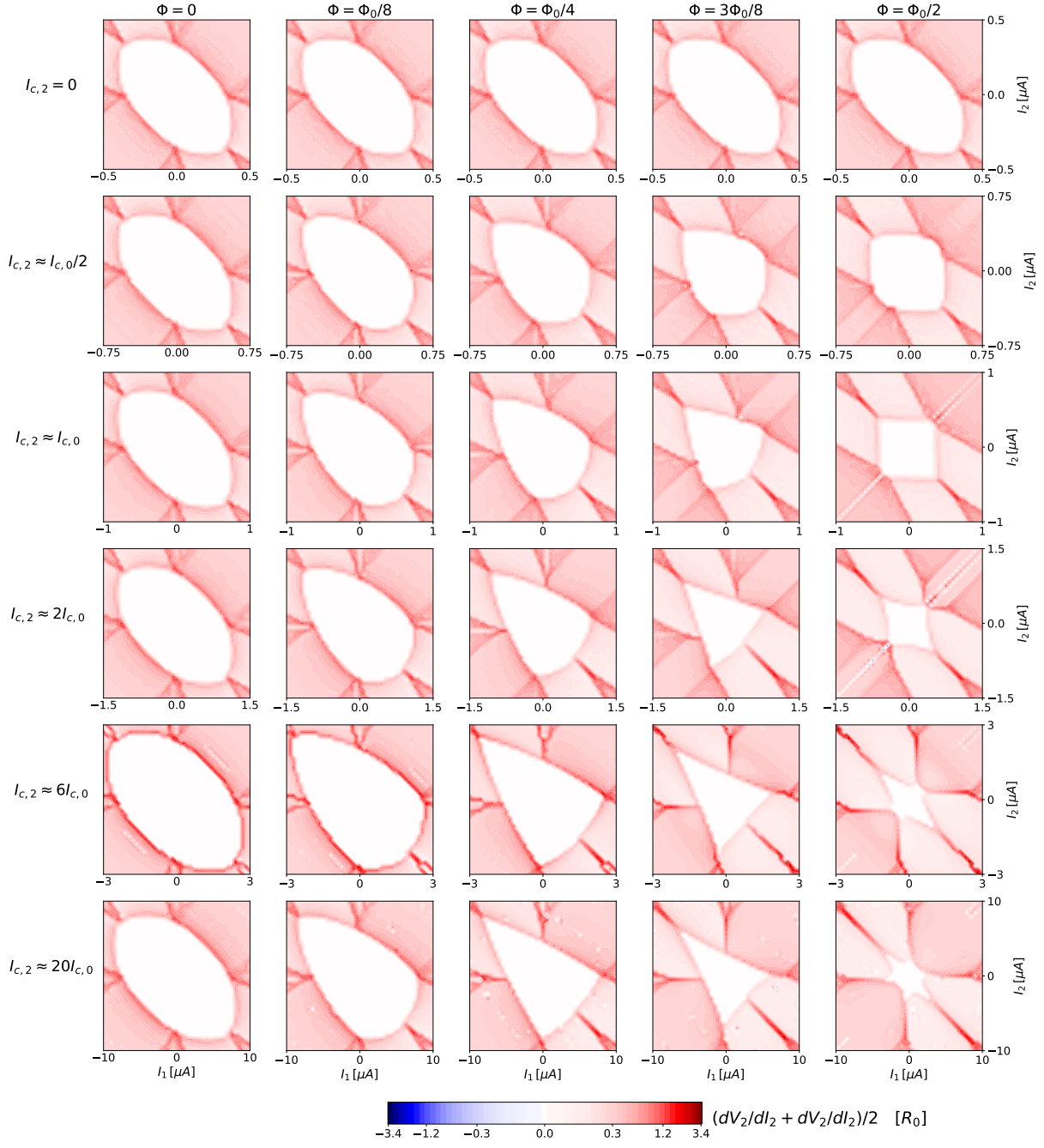Figure 5.15: CCC and branches as a function of different direct coupling energies and flux values. Each subplot in the table is a sum of differential resistance plots $(dV_1/dI_1 + dV_2/dI_2)/2$ for the given parameters at 40×40 pixels. The detuning is $\epsilon_d/\Gamma = 10$, so $I_{c,0} \in [0.1915, 0.2000]\,\mu A$ and the exact values of $I_{c,2}$ are taken as fractions of $0.2\,\mu A$. $R_0 = 100\,\Omega, C_0 = 60$ fF.

symmetric so that the circuit can carry double as much current before building a finite voltage. Without a flux, this is analogous to doubling the critical current and capacitance of the green junctions, halving their resistances and omitting the blue. This logic agrees with the numerical results; the model allows twice as large bias currents inside the CCC, hence the area increases by a factor of 4 relatively to when $I_{c,2} = 0$. The area must continue increasing at the same rate as a function of $I_{c,2}$. We can make this more precise. Looking at the leftmost column, the widths of the figures with zero magnetic field are observed to increase linearly, namely as $\Delta I_1 = 5I_{c,2} + 1\,\mu A$. Hence the area of the CCC increases quadratically as a function of $I_{c,2}$. That makes sense from the stated formula of the area of the elliptical CCC's at $\Phi = 0$, namely $A = 4\pi(I_{c,2} + I_{c,0})^2$.

At $I_{c,2}/I_{c,0} = 20$, the coupling over the QD becomes unimportant and the RCSJ model is approximately equal to a a flux-biased loop of three two-terminal Josephson junctions. From Figure 5.15, we see that in this case the ellipse is deformed to a six-pointed star at $\Phi = \Phi_0/2$, which is reminiscent of the star in the center of the supercurrent plot of Figure 3.2 for $\epsilon_d/\Gamma = 10$. This is the limit where the multiterminal junction is approximately equal to a loop of three two-terminal junctions, but with no flux bias.

The width of the $I_1 = I_2$ branch generally varies as a function of flux when $I_{c,0}$ and $I_{c,2}$ are comparable in size. The width has a minimum around $\Phi = \Phi_0/2$ and $I_{c,2} = I_{c,0}$, which will be discussed in more detail in the next section. The $\Phi = \Phi_0/2$ column reflects that the critical current of an asymmetric SQUID does not go to zero. Rather, it can carry $|I_{c,2} - I_{c,0}|$ at $\Phi = \Phi_0/2$. It agrees with the simulations that the width of the $I_1 = I_2$ branch is $\Delta I = 2I_{c,0}$ for $I_{c,2} \approx I_{c,0}/2$, and $\Delta I = I_{c,0}$ for $I_{c,2} \approx 2I_{c,0}$. Recall how the widths of the $I_1 = I_3$ and $I_2 = I_3$ branches are determined from Figure 5.6. This tells us that the width of those branches are $\Delta I = I_{c,0} + I_{c,2}$. Since the width of the subplots also increase linearly with $I_{c,2}$, these two branches have a constant absolute width in the table.

Finally, we can notice that the width of the multiplet resonances depends on both the flux and the ratio of the coupling energies, since we from the, in this context, very limited resolution of the plots observe that the resonances are most visible at $\Phi_0/8$ and $\Phi_0/4$ and for $I_{c,2} = I_{c,0}$ which ratifies the complexity of the physics of the multiplet resonances.

To conclude on this subsection, we see that the area of the CCC in Figure 5.15 changes as expected just from the circuit model as a function of flux and interterminal coupling ratio $I_{c,2}/I_{c,0}$. Additionally, we observe the overall result that the CCC is inversion symmetric only when $\Phi = 0$ and $\Phi = \Phi_0/2$, and that it changes gradually from convex to concave as Φ is increased from zero to half a flux quantum.

5.3.2 Details of CCC Response for Equal Three- and Two-terminal Coupling

The focus of this subsection is on the detailed effect of flux and bias currents in the $I_{c,2} \approx I_{c,0}$ case, where the flux-pierced loop is approximately a symmetric SQUID.
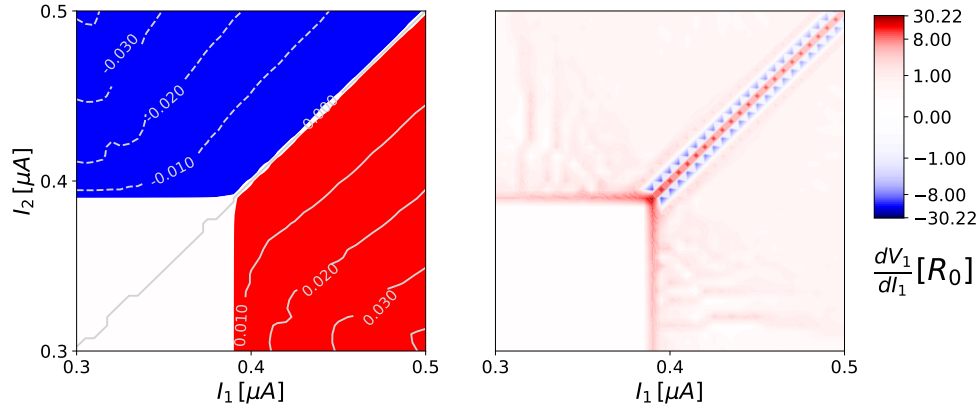

Figure 5.16: $I_{c,2} = 0.2$ and $\Phi = \Phi_0/2$. Left: $V_1 - V_2$ as a function of bias currents. Red and blue indicate the regions of positive and negative voltage regions, respectively. Contour lines for the voltage are shown, in units of $R_0 e \Gamma \hbar^{-1}$. Right: $(dV_1/dI_1 + dV_2/dI_2)/2$. 40×40 pixels (pixel size $0.005 \, \mu A$). Integration time $1000 \, t_0$ and $d\tilde{t} = 0.02$.

In order to explain the effect of the flux in more detail, we consider the case of $I_{c,2} = 0.2 \, \mu A \approx I_{c,0}$. The $I_2 = -I_1$ line corresponds to a SQUID with two junctions of current $I_{c,2} \sin(\phi_1 - \phi_2)$ connected to an extra loop of zero flux with two junctions of critical current $2I_{c,2}$. At zero flux, this is the semi-major axis of the ellipse as discussed previously. Here, the maximal current with zero voltage should be $4I_{c,2} = 0.8 \, \mu A$ in both I_1 and I_2. Half of the current runs through the SQUID part of the circuit and the other half runs through the bottom loop. When we now increase the flux to $\Phi = \Phi_0/2$, the maximal current is seen to reduce to half the value. This agrees with our knowledge about the SQUID from Section 2.2 that no bias current can flow in the symmetric SQUID at zero voltage. The CCC under these conditions is unique, namely a perfect square. We can make sense of this by once again looking at Figure 5.14 and start at $I_2 = 0$ with $I_{c,2} = I_{c,0}$ and $\Phi = \Phi_0/2$. The SQUID part of the circuit can take no bias current within the superconducting regime, so I_1 will be distributed equally over the two remaining arms. This means the CCC is reached at $I_1 = 2I_{c,2}$, which agrees with the plot shown. The path of I_1 to ground does not interfere with the path of I_2 to ground, so the CCC continues along the vertical direction for $I_2 = \pm 2I_{c,2}$. This is why the CCC is a square under these special conditions. This is shown at a high resolution plot in Figure 5.16. The CCC is an exception from the general statement that the critical current of a multiterminal Josephson junction cannot be decomposed into a scalar in the direction of each bias current. In this case, the critical currents in I_1 and I_2 are independent. One could imagine utilizing a junction with this property as an intersection point of superconducting wires where independent currents can cross without affecting each other.

Another unique property of this plot is the $I_1 = I_2$ branch width going to zero. Recall that in the $I_1 = I_2$ case, any deviation δI from this line must be split in two, each half going around the loop in clockwise and anti-clockwise direction, respectively (see Figure 5.7). Hence, in the case where $I_1 = I_2 + \delta I$, the SQUID is biased by a current $\delta I/2$ which, in the case of a symmetric SQUID at half a flux quantum, immediately results in a finite voltage. The pixel size is decreased by a factor of 100 in these plots, and the integration improved as stated in the figure text. Up to this resolution, the $I_1 = I_2$ branch has zero width.

When the bias currents are exactly balanced, the voltage $V_1 - V_2$ over the SQUID is zero, as seen in the left plot of Figure 5.16. Deviating from this point, resistance builds in immediately over the SQUID, so there is a large peak in differential resistance on the $I_1 = I_2$ line as seen in the right plot of Figure 5.16.

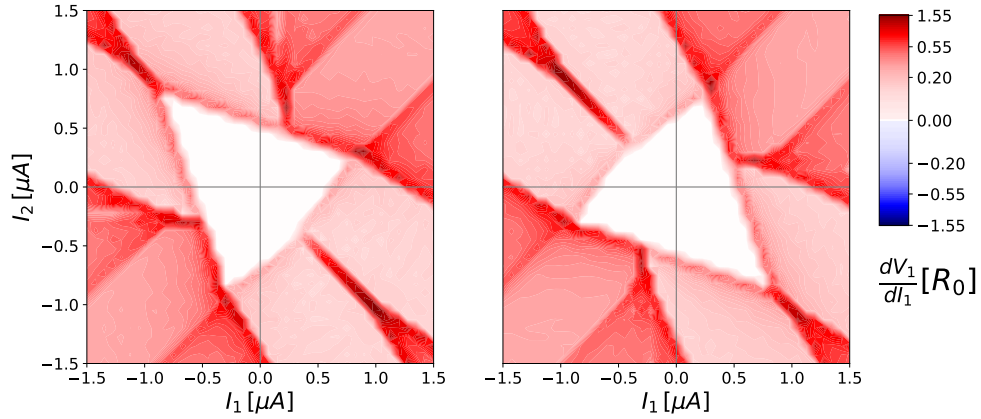### 5.3.3 The Symmetry of Flux Inversion

Figure 5.17: Flipping the sign of Φ and inverting it around the origin leaves the CCC invariant. Left: The figure is identical to the subplot at $I_{c,2} \approx 2I_{c,0}$, $\Phi = 3\Phi_0/8$ in the CCC table (Figure 5.15). Right: Same conditions but with $\Phi = -3\Phi_0/8$.

There is an important symmetry in CCC as a function of flux between the table in Figure 5.15 and the part that has been omitted, namely for flux values between $\Phi \in]-\Phi_0/2; 0[$. The missing half of the table is simple to construct. Flipping the sign of Φ reverses the direction of the screening current as can be confirmed by looking at Figure 2.5b or by simply applying the right-hand rule. Hence by simultaneously reversing the direction of I_1 and I_2, the system is back to its original configuration. As a conclusion, the differential resistance plot for $\Phi \to -\Phi$ can be constructed by inverting the figure around the origin, corresponding to $I_1 \to -I_1$ and $I_2 \to -I_2$. This is another argument to why the contours for $\Phi = 0$ and $\Phi = \Phi_0/2$ must be inversion symmetric. An example of two figures with two flux values of opposite sign is shown in Figure 5.17. The figures are not constructed as explained above, but both generated individually.

5.3.4 Resonant Case

The discussion of Section 5.3 so far has only been concerned with the case of large detuning. In order to get a sense of the effect of the detuning as well, a similar table of CCC has been calculated for the opposite extreme, $\epsilon_d/\Gamma = 0.1$. The result is shown in Figure 5.18. Additionally to the same overall effects of the flux, when the energy level of the quantum dot approaches resonance with the superconductors, the CCC of the three-terminal Josephson junction is hexagonal, as was seen in Figure 3.2. As $I_{c,2}$ increases, the hexagon approaches the elliptical shape of a CCC of a Josephson junction with currents of constant amplitude. For this detuning, the critical current varies wildly, ranging between $0.666\,\mu A$ and $20\,\mu A$ as a function of phase, which makes it hard to compare to $I_{c,2}$ a priori. From the numerical results, the direct coupling seems to dominate completely already at $I_{c,2} = 10\,\mu A$. The CCC's at this value are indistinguishable from the contours for $I_{c,2} = 20I_{c,0}$ at high detuning. This indicates that the effective critical current lies close to the lower limit. Indeed, the Josephson currents are weighted by the sine-terms such that they only vary between -2 and 2 μA as seen in (3.2).

In order to highlight the gradual introduction of nodes in the CCC, three simulations with small steps in flux between each are shown in Figure 5.19. The CCC is seen to change from convex for $\Phi = 0.225\,\Phi_0$ to contain one node for $\Phi = 0.300\,\Phi_0$. The same results can be found for large detuning $\epsilon_d/\Gamma = 10$ when $I_{c,2} \approx 2I_{c,0}$. Here, the CCC at $\Phi_0/2$ is very similar to the CCC for $\epsilon_d/\Gamma = 0.1$ and $I_{c,2} = 1\,\mu A$ for the same flux value. This is another indication that the effective $I_{c,0}$ value in relation to the zero-voltage state lies close to its lower boundary of $0.666\,\mu A$.

In the case of large detuning, the CCC's require a larger increase in flux to reproduce Figure 5.19. The CCC of Figure 5.19 for $\Phi = 3\Phi_0/8$ is reproduced by a flux value of $\Phi = 7\Phi_0/16$ in the large detuning case. Thus for different detunings, the flux-biased three-terminal junction do not respond to flux at the same rate.
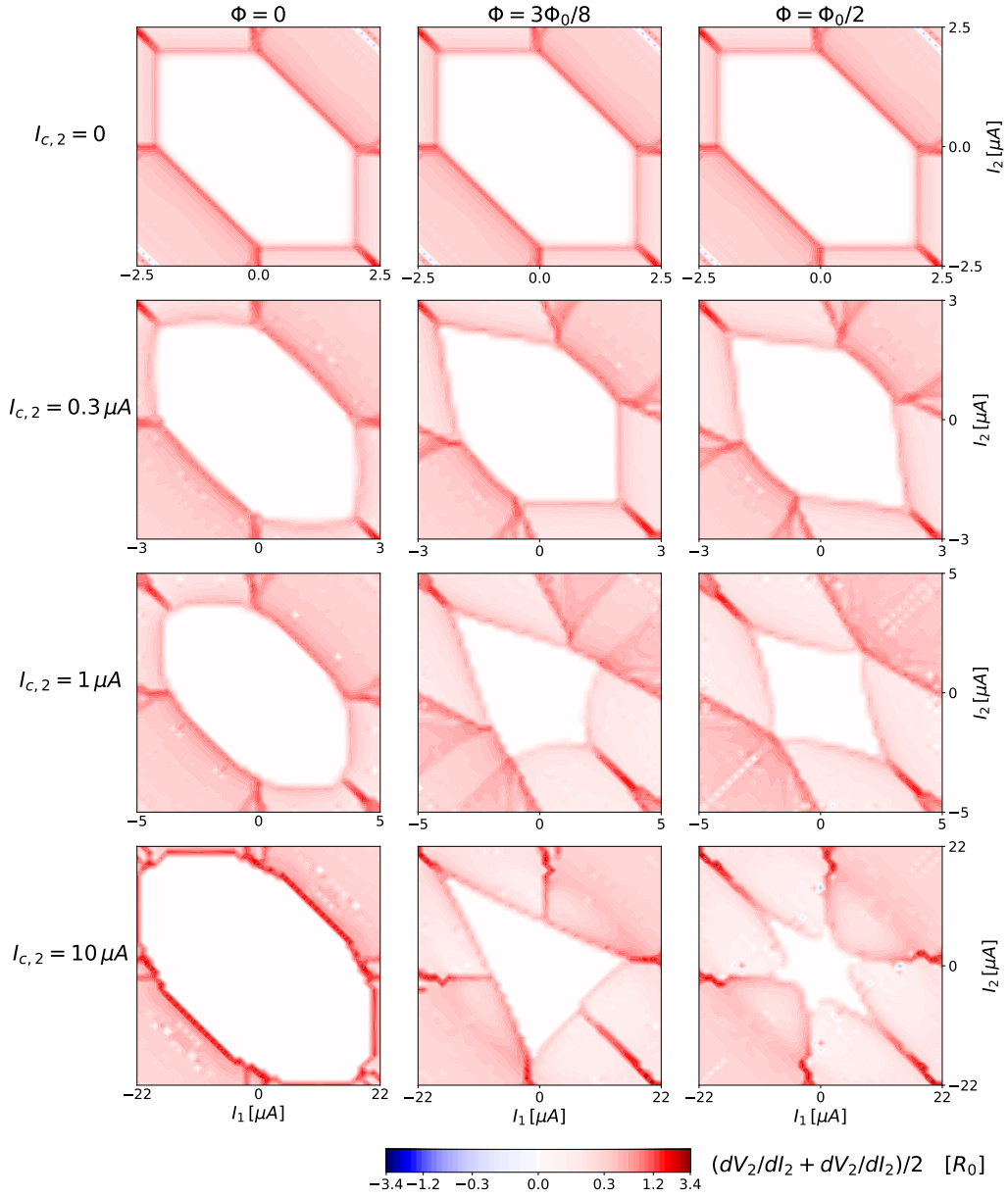
Figure 5.18: CCC and branch response to flux and coupling energies for $\epsilon_d/\Gamma = 0.1$ where $I_{c,0} \in [0.666, 20]\,\mu A$. Each subplot in the table is a sum of differential resistance plots $(dV_1/dI_1 + dV_2/dI_2)/2$ for the given parameters at 40×40 pixels. $R_0 = 100\,\Omega, C_0 = 60$ fF.
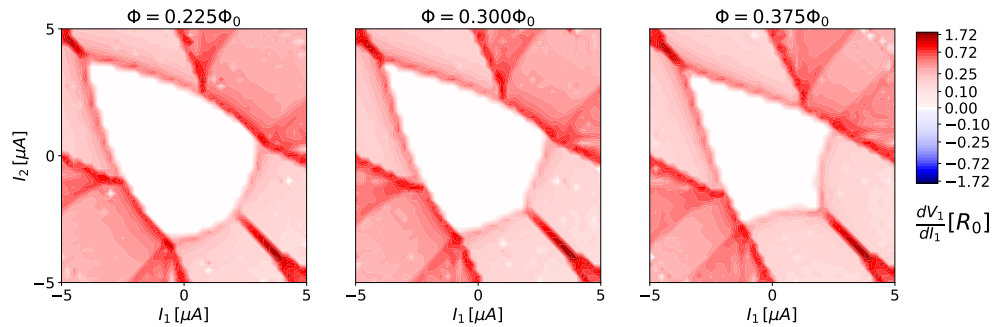

Figure 5.19: $(dV_1/dI_1 + dV_2/dI_2)/2$ for $\epsilon_d/\Gamma = 0.1$ and $I_{c,2} = 1\,\mu A$ at three different flux values. The rightmost plot is equal to the plot in Figure 5.18 for $3\Phi_0/8$.

5.4 Comparison of Numerical Findings to Experimental Results

In this section, the results of the previous section are compared to the experimental results of Reference [20].

In this recent paper, the effect of a magnetic field on the CCC of a multiterminal Josephson junction is found experimentally with two different setups, which are shown in (d) and (e), respectively, in the figure copied from the article, Figure 5.20. The two setups are (d) a four-terminal Josephson junction in a magnetic field and (e) the same four-terminal Josephson junction with two of the leads short-circuited, forming a loop, which is then flux-biased and grounded. The latter can be viewed as a flux-controlled three-terminal junction, so the previously discussed model from Figure 5.14b can be seen as a simplified theoretical model of this setup.
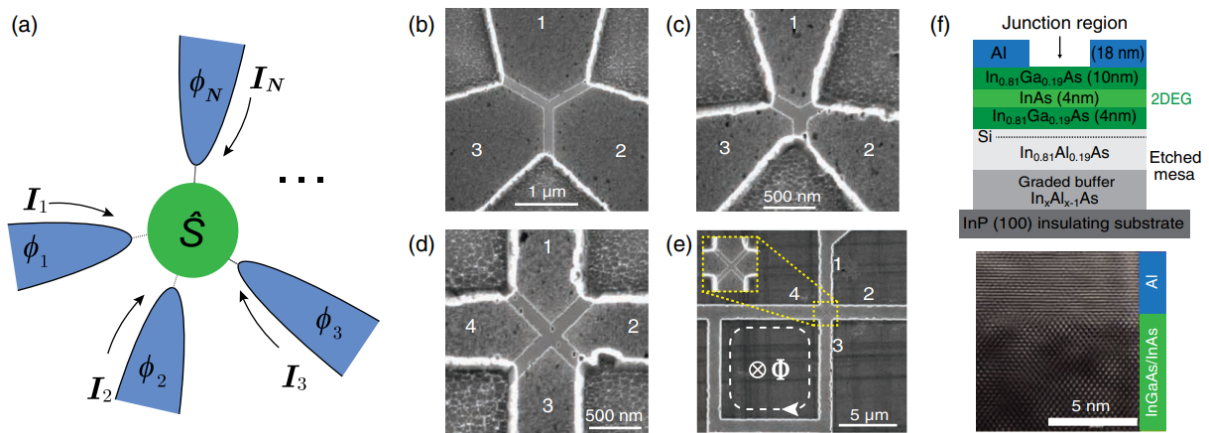
Figure 5.20: Figure from Ref. [20] showing (a) Model for n-terminal junction, (b) Three-terminal symmetric junction, (c) Three-terminal symmetric junction, (d) Four-terminal junction, (e) Flux-biased and short-circuited four-terminal junction and (f) Vertical cross section of the devices in (b)-(e).

Figure 5.21: Figure from Ref. [20] showing the zero-voltage state for experiment (e) of Figure 5.20 at different flux values.

The results of the experiment (e) are shown for $\Phi = 0$, $\Phi = 0.39\,\Phi_0$ and $\Phi = 0.5\,\Phi_0$ in Figure 5.21. There is an indisputable similarity of the results of experiment (e) and the numerical results of Section 5.3 for $I_{c,2} \gg I_{c,0}$.

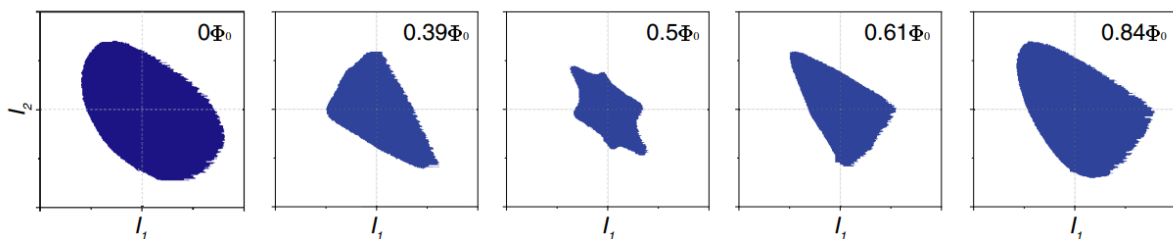We see the same overall transformation of the CCC from ellipse at $\Phi = 0$ over triangle to a six-pointed star at $\Phi = \Phi_0/2$. The inversion symmetry at half-integer multiples of Φ_0 is not perfect, but small enough to be attributed small variations from the ideal system of the model of Section 5.3. We also observe noise in the measurements at the right side of the boundaries of all the plots, which must be attributed to the way the measurements have been performed. Also the inversion symmetry for flipped direction of the flux is evident for the values $\Phi = 0.39\,\Phi_0$ and $\Phi = -0.39\,\Phi_0$.

The comparison of the simulations to this experiment indicates that the coupling energies of the experimental setup is dominated by the two-terminal coupling between neighboring leads.
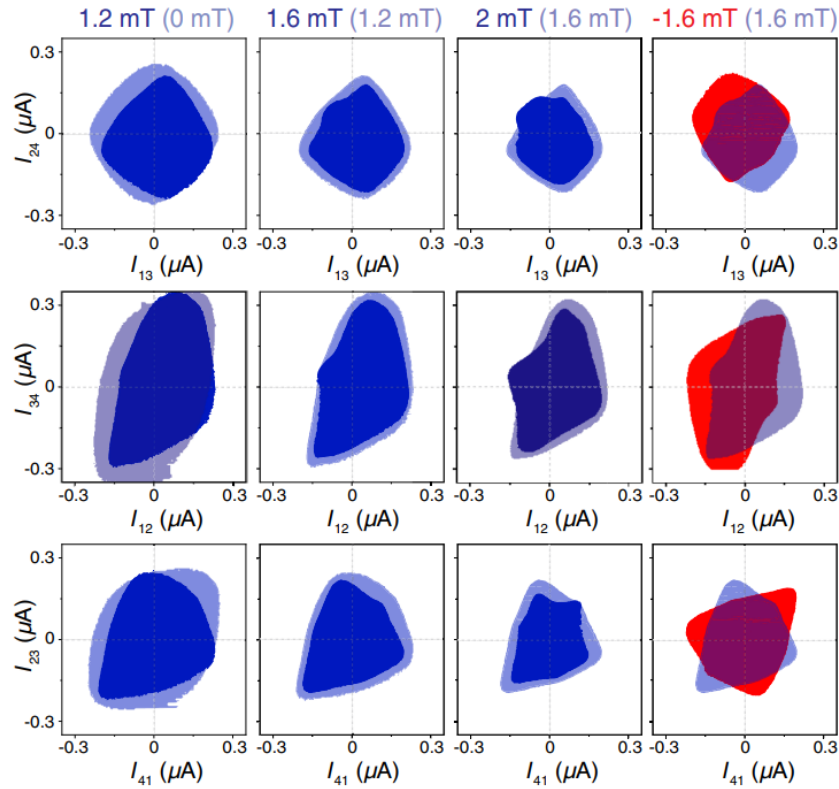

Figure 5.22: Figure from Ref. [20] showing the results of experiment (d) of Figure 5.20 exposed to four different magnetic fields. The quantities in the axes are described in the text.

Experiment (d) is a four-terminal junction exposed to a magnetic field which pierces its center. Since there are four terminals, the CCC is a three-dimensional object in the space of the three independent bias currents. Since one cannot clearly visualize a three-dimensional object in two dimensions, the constraints are added on the bias currents $I_{ij} : I_i = -I_j$ for $i, j \in [0; 4], i \neq j$, and these two-dimensional projections to (I_{ij}, I_{kl}) space are plotted. That is, the four leads are paired in the three possible combinations (I_{12}, I_{34}), (I_{23}, I_{41}) and (I_{13}, I_{24}), respectively, so that three different plots are presented for each field value in Figure 5.22. The three two-dimensional projections respond qualitatively in the same way to a magnetic field of a fixed strength, but the sizes and shapes clearly differ. The combination (I_{13}, I_{24}) must differ from the two others, since

in this case the leads are coupled in a way that forces the supercurrents in the normal region to cross each other. From the fact that the two other combinations do not produce identical plots, it is evident that the experimental setup is not strictly symmetric, so that the sizes, critical currents and relative distances between the leads cannot be seen as constant.

The results of (d) can clearly be distinguished from (e), but the overall features in terms of inversion symmetry and convexity persist. The same applies to all the simulations of Section 5.3. Thus these features are confirmed to be quite general for multiterminal Josephson junctions and less sensitive to the details of the geometry.

Experiment (d) is less straightforward to compare to the simulations since the experimental setup is different and since it is unclear what the exact relation between the field strength and flux is. Simulating this experiment would require an extension of the RCSJ model to four terminals by adding three Josephson junctions of critical current $I_{c,0}$ to the model, simply adding one term to each of the Josephson currents. The flux through the center could be accommodated in the limit of large detuning. Regarding the conversion between magnetic field and flux, the maximal field strength of 2 mT is reported to correspond to approximately $\Phi_0/5$, but the effective value is expected to be larger due to the flux focusing effect, which arises from the fact that for sufficiently thick leads the magnetic field is screened completely, thereby increasing the flux through the normal material. Finally, we possess no information about the details of the experiment which cause the deviations in the supercurrent region between each row of Figure 5.22.

Notwithstanding this series of caveats, it is clear that the simulations of Figure 5.19 are very similar to the bottom row of Figure 5.22, which have been produced in both the resonant and detuned limit.

The maximal flux used in Figure 5.19, $\Phi = 0.375\,\Phi_0 = 3\Phi_0/8$, is 87.5 % larger than $\Phi_0/5$; the expected value of flux at 2 mT in the absence of flux focusing. The ratio between the flux of the three simulations is the same as the ratio between the field strengths of the three plots in the article. Thus it seems plausible to believe that the flux value in this specific setup corresponding to 2 mT is significantly larger than $1/5$ of the flux quantum. The 87.5 % increase is of course not very precise, since the CCC has only been analyzed for a limited amount of flux values, and should be done for an approximately continuous range of flux values to do a more quantitative comparison of the plots. Simulations have been performed for the six values $\Phi \in [0.167, 0.2, 0.25, 0.30, 0.33, 0.375]\,\Phi_0$, the results of which suggest that 2 mT corresponds to $\Phi_0/5$ times a factor of between $3/2$ and 2, assuming that the effective flux increases by the same ratio for all three values in this range (0.12, 0.16 and 0.20 mT). To make this even less precise, if we use the simulation for $\epsilon_d/\Gamma = 10$ the highest flux is $\Phi = 7\Phi_0/16$, a 119% increase from $\Phi_0/5$. At the end of the day, it seems like the flux value in experiment (d) is increased by roughly a factor of 2 with respect to the initially stated value of $\Phi_0/5$, which can probably be explained by the flux focusing effect.

To conclude on this chapter, we have most importantly seen that the most robust of the features, namely the properties regarding convexity, inversion symmetry and the change in area are found to be universal for all simulations and experiments.

Additionally, when going into more detail, the results of the experiment (e) with two of four terminals short-circuited, mimicking a three-terminal Josephson junction, agree very well with the result of the simulations of Section 5.3 at $I_{c,2} \gg I_{c,0}$, backing up the validity of the model used throughout this thesis. This, in turn, provides an estimate of the relation between the energy scales of the experiment. The result suggests that a high direct coupling energy compared to the three-terminal coupling energy is experimentally realistic, but whether any other tuning of $I_{c,0}/I_{c,2}$, corresponding to the rows of the tables of figures 5.15 and 5.18, is experimentally accessible by design, remains unknown.

Regarding the results of the experiment on a four-terminal Josephson junction, we cannot expect the details of the experimentally found CCC's to agree with our simulations, since we use a three-terminal model for the simulations. Despite of this, we find that the simulations of Figure 5.19, requiring a decrease in $I_{c,2}/I_{c,0}$ of an order of magnitude with respect to above, are very similar to the results of the experiment when the current biases are paired as $I_3 = -I_2$ and $I_4 = -I_1$, but we do not have sufficient information to argue why this is the case. As long as we do not have a mapping between the model and the experimental setup for the four-terminal Josephson junction, we cannot conclude convincingly on these results. However, as mentioned, the ratio between the field values is the same as between the flux values, and we can see that the CCC is deformed at the same rate. The fact that in any case it requires an increased flux to reproduce the experiments, as expected due to the flux focusing effect, also backs up the validity of the simulations.

5.5 Time-dependent Flux

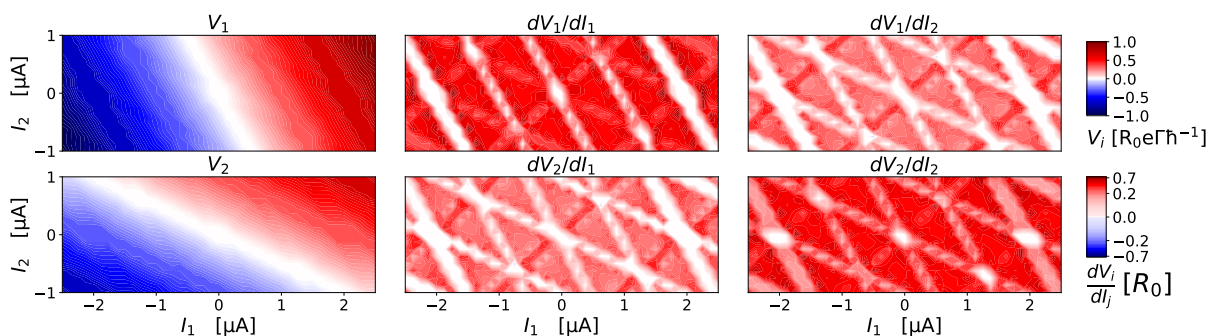Figure 5.23: Differential resistance maps for an oscillating flux $\Phi = \Phi_0 \sin(2\tilde{t})$. The detuning is $\epsilon_d/\Gamma = 10$ and $I_{c,2} = 0.2\,\mu A$. $R_0 = 60\,\Omega$ and $C_0 = 100\,\mathrm{fF}$ such that $Q = 0.60$.

In this section we will generalize the model to accommodate a time-dependent flux through the loop. The motivation for this is that it generates alternating screening currents which are

expected to give rise to fractional Shapiro steps (see Section 2.4). The equation for the RCSJ model of Section 5.3 with a time-dependent flux will be implemented in the numerical solution, and a first signature of fractional Shapiro steps will be demonstrated.

We first consider a general time-dependent flux, which due to its non-zero time-derivatives adds additional terms to the equation of motion. Maintaining the modifications from (5.4), the new equation of motion becomes

$$\begin{pmatrix} \dot{\phi}_1(\tilde{t}) \\ \dot{\phi}_2(\tilde{t}) \end{pmatrix} + \frac{R_0 C_0}{t_0} \begin{pmatrix} \ddot{\phi}_1(\tilde{t}) \\ \ddot{\phi}_2(\tilde{t}) \end{pmatrix} + \left(\pi \dot{\Phi}(\tilde{t})/\Phi_0 + \frac{R_0 C_0}{t_0 \Phi_0} \pi \ddot{\Phi}(\tilde{t}) \right) \begin{pmatrix} 1 \\ -1 \end{pmatrix} = \begin{pmatrix} 2 & 1 \\ 1 & 2 \end{pmatrix} \begin{pmatrix} \tilde{I}_1 - \tilde{I}_{J1}(\phi_1(\tilde{t}), \phi_2(\tilde{t})) \\ \tilde{I}_2 - \tilde{I}_{J2}(\phi_1(\tilde{t}), \phi_2(\tilde{t})) \end{pmatrix}. \tag{5.5}$$

Now considering the specific form $\Phi = \Phi_0 \sin(\omega t)$, the equation for S is

$$\frac{d}{d\tilde{t}} S(\tilde{t}) = \frac{t_0}{R_0 C_0} \begin{pmatrix} 0 & 0 & 1 & 0 \\ 0 & 0 & 0 & 1 \\ 0 & 0 & -1 & 0 \\ 0 & 0 & 0 & -1 \end{pmatrix} S(\tilde{t}) + \begin{pmatrix} 0 & 0 & 0 & 0 \\ 0 & 0 & 0 & 0 \\ 2 & 1 & 1 & 0 \\ 1 & 2 & -1 & 0 \end{pmatrix} \begin{pmatrix} \tilde{I}_1 - \tilde{I}_{J1}(\phi_1(\tilde{t}), \phi_2(\tilde{t})) \\ \tilde{I}_2 - \tilde{I}_{J2}(\phi_1(\tilde{t}), \phi_2(\tilde{t})) \\ \pi \omega t_0 \cos(\omega t) - \frac{R_0 C_0}{t_0} \pi (\omega t_0)^2 \sin(\omega t) \\ 0 \end{pmatrix}.$$

The simulation is performed at $\epsilon_d/\Gamma = 10$ and $I_{c,2} = 0.2\,\mu A$ and shown in Figure 5.23. This differential resistance map has a completely different composition with an almost periodic network of branches of zero- and reduced resistance branches. These lines have the same slopes as the branches in absence of the flux, and we observe a CCC around $(I_1, I_2) = (0, 0)$. Hence, the picture of Figure 5.5 is roughly unchanged, but now we see that in presence of the oscillating flux, the branches are periodically repeated with a period of $1\,\mu A$. With a frequency of $\tilde{\omega} = 2$, corresponding to $\omega = 1.22 \cdot 10^{11}\,\mathrm{s}^{-1}$, the voltages should take values that are fractions of $\hbar\omega/2e = 40\,\mu V$. The values of V_1 as a function of I_1 for $I_2 = 0$ are shown in Figure 5.24. V_1 is given in units of $R_0 e \Gamma \hbar^{-1} = 60\,\mu V$, so the distance between the Shapiro steps is seen to be $20\,\mu V = \hbar\omega/4e$. Hence, the model exhibits distinct half-integer Shapiro steps, the same result as in Ref. [11].
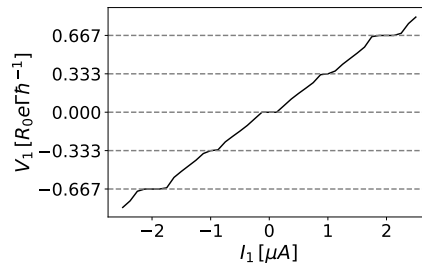
Figure 5.24: Black line: cross section of V_1 of Figure 5.23 at $I_2 = 0$. The dotted lines mark the values of V_1 at the plateaus.

The result of fractional Shapiro steps for multiterminal Josephson junctions has been reproduced, and it has been demonstrated that an oscillating flux bias is an alternative method to obtain the result. This is just an initial test, and one could gain much more insight by building upon this in the future.

6 Conclusion

6.1 Summary

In this thesis, a broad range of properties of Josephson junctions has been covered. Starting from a model describing n equal superconductors symmetrically coupled through a single energy level on a quantum dot in the non-interacting limit, an effective low-energy Hamiltonian was derived for the quantum dot. As a manifestation of the proximity effect, a gap was induced in its density of states and Andreev bound states emerged in its energy spectrum.

The general problem was from here confined to the case of $n = 3$. A qubit design consisting of a flux-biased loop with one two- and one three-terminal Josephson junction was proposed, and it was found that for a specific tuning of the Josephson energies and the flux, its potential equals a loop of three two-terminal Josephson junctions to zeroth order. Inspired from an existing qubit proposal of this form, the DSFQ, it was found that a variable protection approach for realizing gates would be a reasonable method for this qubit.

A three-terminal RCSJ model laid the foundation for the principal part of the thesis. The structure of the differential resistance map as a function of bias currents was examined minutely, dividing the map into conductance levels; a zero-resistance region enclosed by the CCC for low bias current pairs, three branches of reduced resistance, each corresponding to supercurrent between one pair of leads, and multiplet resonances, narrow rays of zero resistance.

The branch width in the limit of large bias currents and large detuning was derived, and it was shown that the width is reduced outside this limit, particularly in the vicinity of the CCC. It was also shown how the width depends on the Q factor for low bias currents.

The slopes of the multiplet resonances were derived, and higher-order multiplets were shown to bend towards the quartet resonance as the bias currents approach the CCC. Again, it was shown that the width of the multiplets is determined by the Q factor.

Throughout the thesis, an emphasis was laid on the dependence on the Q factor, which was shown to be an important catalyst of the dynamics in the treated aspects of the multiterminal Josephson junction, where the dependence on R and C could always be collected in the Q factor.

As an extension of the RCSJ model, direct coupling between neighboring leads was included to accommodate a flux bias. The CCC was displayed as a function of direct coupling strength and flux bias both in both the resonant and detuned case. It was shown that the CCC is inversion symmetric with respect to its flux inverted counterpart and that the critical current contour is convex at $\Phi = 0$, shifting to concave close to $\Phi = \Phi_0/2$, both in agreement with experimental evidence. The model was used for estimating energy scales and the significance of the flux focusing effect in the experimental setup. A unique behaviour was detected at half a flux quantum and equal coupling energies where the CCC was found to be a square, thereby recovering the scalar critical current known from two-terminal junctions, and one of the branches

of the differential resistance map was found to collapse to zero width.

To close the circle, half-integer Shapiro steps were demonstrated with a sinusoidally time-varying flux bias.

6.2 Discussion and Outlook

The thesis comes around numerous aspects of multiterminal Josephson junctions, supporting previous results about general conductance properties, multiplets, Shapiro steps and response to magnetic fields, while adding new details to the existing literature.

It is remarkable that this elementary, analytically solvable model for the multiterminal Josephson effect contains such rich physics, and that the results regarding response of the CCC to a flux, multiplets and Shapiro steps agree with experimental results. The approximations done in the derivation have passed the test and the validity of the model has been backed up by evidence, acting as a motivation to use it for making additional predictions. Furthermore, the overall qualitative results agree with different setups like the four-terminal Josephson junction, so these results are more general than for the specific model used in the thesis. These results have the ability to predict the outcomes of a different experimental architecture which changes the coupling strengths between the leads. The table of CCC response to flux is also a way to estimate the coupling strengths in the system like for example the ones of Ref. [20], where it was found that $I_{c,2} \gg I_{c,0}$. However, not all simulations are necessarily experimentally accessible, and it might for example be difficult to design the experiment such that all pairs of leads couple at least as strongly through the quantum dot as the neighboring leads.

The multiterminal Josephson junction has been shown to be a candidate for a qubit with variable protection, closely related to the DSFQ. Replacing a pair of two-terminal junctions by one three-terminal junction is more compact and could be an advantage in terms of minimizing the spatial extension of the qubit. Also, the models deviate when tuning the flux and Josephson energies away from the specific configuration, and the detuning can be controlled as an additional parameter. Whether it possesses any advantages in terms of qubit performance will require further studies. The next step would be gate implementation and finding out more about the sensitivity to variations in flux bias.

Apart from this, a natural continuation of the work done in this thesis would be to go more in detail with Shapiro steps to get a more complete understanding of the results of Section 5.5, including a high resolution plot of the region closely around the CCC to compare with the $\Phi = 0$ case. This could be followed up by exploring the dependence on amplitude and frequency of the oscillating flux and improving the resolution to see if Shapiro steps of other fractions than $1/2$ could be observed.

Improvement could also be made in studying the decay of the branch width to identify by which function the decay is described. This would first of all require additional data points and more

thought on the required resolution.

The thesis has concentrated on three terminals, which has been an advantage both in clarity in visualization of the results and in comparison to other simulations and experiments which in most cases also work with $n = 3$. However, it would be relevant to extend the model to at least $n = 4$. In this case, the junction can act as an intersection between two superconducting wires. A model of a four-terminal Josephson junction could be used for simulating the corresponding experiment of Ref. [20]. For this, it would also be suitable to allow for some asymmetry in the model in the intrinsic properties of each lead or in the coupling between them.

For further studying the differential resistance maps as a function of a range of parameters, it would be particularly useful to reduce the simulation time. A more gradual change of flux could be studied, and the resolution of figures in the CCC tables could be improved, revealing more detailed features. According to Ref. [10] the speed can be increased by two orders of magnitude by using a graphic card and reformulate the code so that the simulations for different bias current pairs can be computed in parallel.

7 References

[1] M. Tinkham, *Introduction to superconductivity*. Courier Corporation, 2004.

[2] J. Bardeen, L. N. Cooper, and J. R. Schrieffer, "Theory of superconductivity," *Physical review*, vol. 108, no. 5, p. 1175, 1957.

[3] B. D. Josephson, "Possible new effects in superconductive tunnelling," *Physics letters*, vol. 1, no. 7, pp. 251–253, 1962.

[4] F. Arute, K. Arya, Babbush, and R. et al., "Quantum supremacy using a programmable superconducting processor," *Nature Physics*, vol. 574, pp. 505–510, 2019.

[5] P. Krantz, M. Kjaergaard, F. Yan, T. P. Orlando, S. Gustavsson, and W. D. Oliver, "A quantum engineer's guide to superconducting qubits," *Applied physics reviews*, vol. 6, no. 2, p. 021318, 2019.

[6] A. Gyenis, A. Di Paolo, J. Koch, A. Blais, A. A. Houck, and D. I. Schuster, "Moving beyond the transmon: Noise-protected superconducting quantum circuits," *PRX Quantum*, vol. 2, no. 3, p. 030101, 2021.

[7] M. Kjaergaard, M. E. Schwartz, J. Braumüller, P. Krantz, J. I.-J. Wang, S. Gustavsson, and W. D. Oliver, "Superconducting qubits: Current state of play," *Annual Review of Condensed Matter Physics*, vol. 11, pp. 369–395, 2020.

[8] P. Strenski and S. Doniach, "A system of three josephson junctions," *Journal of applied physics*, vol. 57, no. 3, pp. 867–874, 1985.

[9] F. Zhang, A. S. Rashid, M. T. Ahari, W. Zhang, K. M. Ananthanarayanan, R. Xiao, G. J. de Coster, M. J. Gilbert, N. Samarth, and M. Kayyalha, "Andreev processes in mesoscopic multi-terminal graphene josephson junctions," *arXiv preprint arXiv:2210.04408*, 2022.

[10] E. G. Arnault, S. Idris, A. McConnell, L. Zhao, T. F. Larson, K. Watanabe, T. Taniguchi, G. Finkelstein, and F. Amet, "Dynamical stabilization of multiplet supercurrents in multi-terminal josephson junctions," *Nano Letters*, vol. 22, no. 17, pp. 7073–7079, 2022.

[11] E. G. Arnault, T. F. Larson, A. Seredinski, L. Zhao, S. Idris, A. McConnell, K. Watanabe, T. Taniguchi, I. Borzenets, F. Amet, *et al.*, "Multiterminal inverse ac josephson effect," *Nano letters*, vol. 21, no. 22, pp. 9668–9674, 2021.

[12] R.-P. Riwar, M. Houzet, J. S. Meyer, and Y. V. Nazarov, "Multi-terminal josephson junctions as topological matter," *Nature communications*, vol. 7, no. 1, p. 11167, 2016.

[13] R. L. Klees, G. Rastelli, J. C. Cuevas, and W. Belzig, "Microwave spectroscopy reveals the quantum geometric tensor of topological josephson matter," *Physical Review Letters*, vol. 124, no. 19, p. 197002, 2020.

[14] G. V. Graziano, M. Gupta, M. Pendharkar, J. T. Dong, C. P. Dempsey, C. Palmstrøm, and V. S. Pribiag, "Selective control of conductance modes in multi-terminal josephson junctions," *Nature communications*, vol. 13, no. 1, p. 5933, 2022.

[15] M. Amin, A. Omelyanchouk, A. Blais, A. M. van den Brink, G. Rose, T. Duty, and A. Zagoskin, "Multi-terminal superconducting phase qubit," *Physica C: Superconductivity*, vol. 368, no. 1-4, pp. 310–314, 2002.

[16] Z. Qi, H.-Y. Xie, J. Shabani, V. E. Manucharyan, A. Levchenko, and M. G. Vavilov, "Controlled-z gate for transmon qubits coupled by semiconductor junctions," *Physical Review B*, vol. 97, no. 13, p. 134518, 2018.

[17] A. V. Galaktionov and A. D. Zaikin, "Current-biased andreev interferometer," *Physical Review B*, vol. 88, no. 10, p. 104513, 2013.

[18] M. Gupta, G. V. Graziano, M. Pendharkar, J. T. Dong, C. P. Dempsey, C. Palmstrøm, and V. S. Pribiag, "Superconducting diode effect in a three-terminal josephson device," 2022.

[19] A. W. Draelos, M.-T. Wei, A. Seredinski, H. Li, Y. Mehta, K. Watanabe, T. Taniguchi, I. V. Borzenets, F. Amet, and G. Finkelstein, "Supercurrent flow in multiterminal graphene josephson junctions," *Nano letters*, vol. 19, no. 2, pp. 1039–1043, 2019.

[20] N. Pankratova, H. Lee, R. Kuzmin, K. Wickramasinghe, W. Mayer, J. Yuan, M. G. Vavilov, J. Shabani, and V. E. Manucharyan, "Multiterminal josephson effect," *Physical Review X*, vol. 10, no. 3, p. 031051, 2020.

[21] W. McMillan, "Tunneling model of the superconducting proximity effect," *Physical Review*, vol. 175, no. 2, p. 537, 1968.

[22] T. Meng, "Andreev bound states in josephson quantum dot devices," *Master's thesis, Institut Néel, CNRS Grenoble*, 2009.

[23] P. Ioselevich and M. Feigel'man, "Tunneling conductance due to a discrete spectrum of andreev states," *New Journal of Physics*, vol. 15, no. 5, p. 055011, 2013.

[24] J. Pillet, C. Quay, P. Morfin, C. Bena, A. L. Yeyati, and P. Joyez, "Andreev bound states in supercurrent-carrying carbon nanotubes revealed," *Nature Physics*, vol. 6, no. 12, pp. 965–969, 2010.

[25] A. Nurbawono and C. Zhang, "Sensing with superconducting point contacts," *Sensors*, vol. 12, no. 5, pp. 6049–6074, 2012.

[26] M. Houzet and P. Samuelsson, "Multiple andreev reflections in hybrid multiterminal junctions," *Physical Review B*, vol. 82, no. 6, p. 060517, 2010.

[27] M. Octavio, M. Tinkham, G. Blonder, and T. Klapwijk, "Subharmonic energy-gap structure in superconducting constrictions," *Physical Review B*, vol. 27, no. 11, p. 6739, 1983.

[28] V. Bouchiat, D. Vion, P. Joyez, D. Esteve, and M. Devoret, "Quantum coherence with a single cooper pair," *Physica Scripta*, vol. 1998, no. T76, p. 165, 1998.

[29] W. Smith, A. Kou, X. Xiao, U. Vool, and M. Devoret, "Superconducting circuit protected by two-cooper-pair tunneling," *npj Quantum Information*, vol. 6, no. 1, p. 8, 2020.

[30] T. W. Larsen, M. E. Gershenson, L. Casparis, A. Kringhøj, N. J. Pearson, R. P. McNeil, F. Kuemmeth, P. Krogstrup, K. D. Petersson, and C. M. Marcus, "Parity-protected superconductor-semiconductor qubit," *Physical review letters*, vol. 125, no. 5, p. 056801, 2020.

[31] S. Krøjer, A. E. Dahl, K. S. Christensen, M. Kjaergaard, and K. Flensberg, "Fast universal control of a flux qubit via exponentially tunable wave-function overlap," *arXiv preprint arXiv:2303.01102*, 2023.

[32] S. Shapiro, "Josephson currents in superconducting tunneling: The effect of microwaves and other observations," *Physical Review Letters*, vol. 11, no. 2, p. 80, 1963.

[33] O. Deb, K. Sengupta, and D. Sen, "Josephson junctions of multiple superconducting wires," *Physical Review B*, vol. 97, no. 17, p. 174518, 2018.

[34] B. Raes, N. Tubsrinuan, R. Sreedhar, D. Guala, R. Panghotra, H. Dausy, C. C. de Souza Silva, and J. Van de Vondel, "Fractional shapiro steps in resistively shunted josephson junctions as a fingerprint of a skewed current-phase relationship," *Physical Review B*, vol. 102, no. 5, p. 054507, 2020.

[35] Y. M. Shukrinov, S. Y. Medvedeva, A. Botha, M. Kolahchi, and A. Irie, "Devil's staircases and continued fractions in josephson junctions," *Physical Review B*, vol. 88, no. 21, p. 214515, 2013.

[36] T. Klapwijk, G. Blonder, and M. Tinkham, "Explanation of subharmonic energy gap structure in superconducting contacts," *Physica B+ C*, vol. 109, pp. 1657–1664, 1982.

[37] Y. Cohen, Y. Ronen, J.-H. Kang, M. Heiblum, D. Feinberg, R. Mélin, and H. Shtrikman, "Nonlocal supercurrent of quartets in a three-terminal josephson junction," *Proceedings of the National Academy of Sciences*, vol. 115, no. 27, pp. 6991–6994, 2018.

[38] G.-H. Park, K. Watanabe, T. Taniguchi, G.-H. Lee, and H.-J. Lee, "Engineering crossed andreev reflection in double-bilayer graphene," *Nano Letters*, vol. 19, no. 12, pp. 9002–9007, 2019.

[39] H. Bruus and K. Flensberg, *Many-body quantum theory in condensed matter physics: an introduction.* OUP Oxford, 2004.